Characterising and approximating exact density functionals for model electronic systems

Michael Entwistle

Doctor of Philosophy

University of York
Physics

July 2020

Dedicated to my mother, father and grandmother

Characterising and approximating exact density functionals for model electronic systems

M. T. Entwistle

Submitted for the degree of Doctor of Philosophy in Physics

July 2020

Abstract

Accurate descriptions of the electronic properties of molecules, solids and other materials are crucial in the development of many modern technologies, and are therefore the subject of much scientific research. In tandem with experimental research, computational simulations play a huge role. Density functional theory (DFT) is the most popular method for performing ground-state electronic structure calculations due to its accuracy in many situations along with its computational efficiency. Its time-dependent extension (TDDFT) allows the modelling of the dynamics of systems of interacting electrons. (TD)DFT is an exact theory in principle, but requires approximations in practice, specifically to the many-body effects of electron exchange and correlation (xc), which are described by some unknown universal functional. Despite much success, it often proves inadequate in many scenarios of increasing interest. Therefore, we aim to contribute to the development of improved approximate density functionals.

In this thesis, we take the approach of studying small model systems for which we can compute the exact functionals. These systems are designed to exhibit the key features present in realistic quantum systems, such as atoms and molecules, which the exact universal (TD)DFT functional is capable of describing, but are often ill-described by the commonly used approximations. By analysing the nature of these exact functionals, we gain valuable insight into their fundamental properties, together with identifying where the current approximations are lacking, thereby allowing us to suggest how these approximations may be improved.

CONTENTS

LIST OF FIGURES

LIST OF TABLES

ACKNOWLEDGEMENTS

Declaration

I declare that the work presented in this thesis, except where otherwise stated, is based on my own research and has not been submitted for examination at this or any other institution for another award. All sources are acknowledged as References.

Chapter 4 represents collaborative work that has been published:

M. T. Entwistle, M. J. P. Hodgson, J. Wetherell, B. Longstaff, J. D. Ramsden and R. W. Godby, 'Local density approximations from finite systems', *Phys. Rev. B **94**, 205134 (2016)*. I performed all calculations and analysis under the guidance of R. W. Godby. I prepared the first draft of the publication with subsequent drafts written collaboratively with all listed authors.

M. T. Entwistle, M. Casula and R. W. Godby, 'Comparison of local density functionals based on electron gas and finite systems', *Phys. Rev. B **97**, 235143 (2018)*. Except where otherwise stated, all calculations and analysis were performed by me under the guidance of R. W. Godby. Additional calculations were performed by M. Casula. I prepared all drafts of the publication and these were reviewed by R. W. Godby and M. Casula.

Chapter 5 represents work that has been published:

M. T. Entwistle and R. W. Godby, 'Exact nonadiabatic part of the Kohn-Sham potential and its fluidic approximation', *Phys. Rev. Materials **4**, 035002 (2020)*. I performed all calculations and analysis under the guidance of R. W. Godby. I prepared all drafts of the publication and these were reviewed by R. W. Godby.

Chapter 6 represents one piece of work that has been published and one piece of collaborative work that is being prepared for publication:

M. T. Entwistle and R. W. Godby, 'Exact exchange-correlation kernels for optical spectra of model systems', *Phys. Rev. B* **99**, *161102(R) (2019)*. I performed all calculations and analysis under the guidance of R. W. Godby. I prepared all drafts of the publication and these were reviewed by R. W. Godby.

M. T. Entwistle, N. D. Woods and R. W. Godby, 'Insights from exact exchange-correlation kernels'. N. D. Woods and I participated equally in the development of code, execution of calculations and analysis under the guidance of R. W. Godby. N. D. Woods and I are preparing a first draft of the manuscript.

PUBLICATIONS

The following are four publications that contribute to this thesis. Chapters which use wording from these publications have the relevant publication mentioned at the beginning of the chapter.

1. M. T. Entwistle, M. J. P. Hodgson, J. Wetherell, B. Longstaff, J. D. Ramsden and R. W. Godby, 'Local density approximations from finite systems', *Phys. Rev. B* **94**, *205134 (2016)*

2. M. T. Entwistle, M. Casula and R. W. Godby, 'Comparison of local density functionals based on electron gas and finite systems', *Phys. Rev. B* **97**, *235143 (2018)*

3. M. T. Entwistle and R. W. Godby, 'Exact exchange-correlation kernels for optical spectra of model systems', *Phys. Rev. B* **99**, *161102(R) (2019)*

4. M. T. Entwistle and R. W. Godby, 'Exact nonadiabatic part of the Kohn-Sham potential and its fluidic approximation', *Phys. Rev. Materials* **4**, *035002 (2020)*

The following is a study that contributes to Chapter 6 and is being prepared for publication.

5. M. T. Entwistle, N. D. Woods and R. W. Godby, 'Insights from exact exchange-correlation kernels'

INTRODUCTION

A primary contributor to the advancement of many areas of modern technology is the accurate quantum mechanical description of matter. Accordingly, computational simulations have become one of the most important features of scientific research. The majority of electronic structure calculations in condensed matter physics and many areas of materials science are performed using density functional theory (DFT), a method based on a reformulation of quantum mechanics and exact in principle. When extended to the time-dependent regime, time-dependent DFT (TDDFT) is widely used to model the dynamics of systems of interacting electrons. However, the success of (TD)DFT in practical calculations hinges on approximating electron exchange and correlation (xc) — an unknown functional to which various approximations exist. Currently, DFT can be used to accurately model a wide variety of ground-state systems, but there are a number of important situations in which the most commonly used approximate functionals are inappropriate. Furthermore, these ground-state functionals are frequently utilised in many TDDFT calculations, and are often incapable of predictive accuracy in relation to a multitude of applications to diverse fields. In this chapter, we briefly discuss the limitations of (TD)DFT in order to provide the motivations for performing studies shown later in this thesis. We also outline our general strategy for performing these studies and describe the presentation of the results in the context of the overall thesis.

1.1   Motivation

Many-electron quantum mechanics cannot be used in practical calculations due to the computational cost of doing so, and hence methods such as DFT [1, 2] are employed, as discussed above. While being computationally efficient, and hugely successful in many cases, it becomes much less accurate in the presence of strong correlation. Most approximate xc functionals are (semi-) local[1], such as the widely used local density approximation [2] (LDA), which is known to miss out some key features present in the exact xc functional [3–9]. Most applications of TDDFT [10, 11] utilise an adiabatic approach[2], in which the instantaneous electron density is implicitly assumed to be in its ground state, thereby neglecting all memory effects. Here, a ground-state xc functional is used as an approximation to the true xc functional. This proves inadequate in many situations, such as the determination of electronic excitation energies including those of a charge-transfer nature [12], electron dynamics [13] including non-perturbative charge transfer dynamics [14], time-resolved spectroscopy [15] and electron scattering [16].

The approximate density functionals of (TD)DFT that are currently available need to be improved upon to allow more accurate simulations of matter, which are necessary for continual technological advancements where descriptions of electronic properties are crucial.

1.2   Our strategy

Our approach is to study small, prototype systems of a few electrons, where we can solve the many-electron Schrödinger equation exactly, to within machine precision. This gives us access to the exact wavefunctions and electron density, and through optimisation techniques, we can determine the *exact* ground-state and time-dependent exchange-correlation functional. Our aim is to identify features present in the exact xc functional that are missing from the commonly used approximations, in order to inform the development of improved approximate functionals. We can also implement approximations, both established and novel, to test their performance against

---

[1]The true xc potential v_{xc} at each point in space depends on the density at all points in the system in an unknown way. Most approximate functionals are either local, in which v_{xc} at each point is assumed to depend only on its local density value, or semi-local, through, e.g. local density gradients.

[2]The true time-dependent v_{xc} depends on the present and entire history of the density. Adiabatic functionals ignore this memory dependence and use the instantaneous density as the input to the functional.

the exact solutions. Each system we study is designed to illustrate important general phenomena in order to be representative of the behaviour of electrons in more realistic finite systems, e.g. molecules.

To perform our calculations we use the interacting Dynamic Electrons Approach [17] (iDEA) code, developed within our research group. This models small, one-dimensional prototype systems of spinless electrons for which we can compute exact solutions, and is used for all the research presented in this thesis (see Chapter 3 for more details).

1.3 Outline of thesis

Chapter 2 outlines the concepts underpinning many-body quantum mechanics, and through use of the Born-Oppenheimer approximation, many-electron quantum mechanics. We discuss various approaches to performing practical electronic structure calculations, focusing on DFT and TDDFT. We then review the successes and failures of the typical approximations used within these methods, which are the limiting factor in their application, and thus motivate the work presented in this thesis.

In Chapter 3, we outline how we perform our electronic structure calculations using the iDEA code, as mentioned above. We also give details about the workings of iDEA, background theory and development/testing of the code.

The LDA is the simplest and one of the most widely used approximations to the xc functional, and is typically constructed from accurate quantum Monte Carlo (QMC) simulations of the homogeneous electron gas (HEG) – an infinite system approaching the thermodynamic limit. In Chapter 4, we introduce a set of alternative LDAs constructed from one-dimensional finite systems, which resemble the HEG within a finite region. We also construct a HEG-based LDA appropriate for spinless electrons in one dimension. By comparing the finite and HEG LDAs with one another we demonstrate that local approximations constructed from finite systems are a viable alternative, and explore the nature of any differences between them. By identifying their relative strengths and weaknesses, we hope this insight will lead to better accuracy in a variety of applications, and through extension to the time-dependent regime, the development of improved TDDFT functionals from finite systems. This analysis sheds light on whether local density functionals can be tailored for use in ab initio calculations, which has the potential to improve the predictive power of (TD)DFT calculations.

Following on from Chapter 4, which focused on approximating the exact quantities of ground-state DFT, we now move on to exact TDDFT. In practical TDDFT calculations, an adiabatic approximation based on ground-state DFT is often used for the true xc potential, thereby neglecting all memory effects in this part of the Kohn-Sham (KS) potential and severely limiting the application of TDDFT to a multitude of diverse fields. In Chapter 5, we present a new perspective on the KS potential, by considering the purest application of the concept of the adiabatic functional to the *complete* KS potential, and present a simple geometrical "fluidic" approximation to the non-adiabatic part. We find that the fluidic approximation corrects a large part of the error arising from the "exact adiabatic" approach, even when the system is evolving far from adiabatically. We believe this may form a solid foundation for a hierarchy of approximations, and provide an alternative method to conduct TDDFT calculations, particularly in situations where the typical adiabatic xc functionals are insufficient. Through our novel approach, the surprising power of the fluidic approximation helps to address the difficult problem of non-adiabaticity in the evolution of many-electron quantum systems, which the vast majority of approximations completely neglect, and currently prevents the application of TDDFT to a wide variety of experimental situations.

One particularly important class of applications of TDDFT, whose accuracy is severely restricted, is the wide variety of spectroscopies, such as optical absorption spectra of molecules and solids. Here, accurate approximations to the exchange-correlation kernel f_{xc} are required, but the most commonly used approximate kernels are adiabatic and (semi-) local, in much the same way as most approximations to v_{xc} are. There have been a limited number of studies conducted on analysing the character of the exact f_{xc}, all of which focus on particular aspects of it, rather than a mixture. We believe that calculating the full dynamic f_{xc} opens up this possibility. As a step in this direction, in Chapter 6 we calculate the *exact* f_{xc} for prototype systems, including full spatial behaviour and frequency-dependence. By characterising and analysing its properties, we draw conclusions on the applicability of approximate kernels and suggest circumstances where more sophisticated approximations may be needed. We anticipate that the insight our work generates will, through further research, lead to the development of improved approximate kernels for model systems, which we hope can in time be extended to ab initio calculations.

Finally, Chapter 7 summarises the results presented in earlier chapters and brings the work together to decide what broad conclusions we can infer.

ELECTRONIC STRUCTURE THEORY

The fundamental description of nature on the atomic scale is described by the theory of quantum mechanics. This constitutes a many-body problem, stemming from the interactions between particles. Many-body problems rank among the most computationally demanding problems in many areas of science, and are often infeasible. In this chapter, we outline the concepts underpinning many-body quantum mechanics, and through use of the Born-Oppenheimer approximation, many-electron quantum mechanics. The Born-Oppenheimer approximation allows us to consider the motion of the electrons in molecular systems separately from that of the nuclei, i.e. constituting electronic structure calculations. We then discuss approaches to performing these types of calculations with the most prominent being density functional theory (DFT) and its time-dependent counterpart TDDFT. TDDFT, through a reformulation of quantum mechanics, is in principle an exact and efficient theory of the dynamics of systems of interacting electrons, but in practice it requires approximations to be made. We review the successes and failures of these approximations, which are the limiting factor in applications of TDDFT.

2.1 Many-body quantum mechanics

2.1.1 The many-body problem

The behaviour of systems of nuclei and electrons interacting via the Coulomb potential, such as atoms and molecules, is described by the equations of many-body quantum mechanics. These necessitate the formulation of the many-body Hamiltonian[1]:

$$\hat{H} = -\sum_i \frac{\hbar^2}{2m_e} \nabla_i^2 - \sum_I \frac{\hbar^2}{2M_I} \nabla_I^2 - \sum_{i,I} \frac{1}{4\pi\varepsilon_0} \frac{Z_I e^2}{|\vec{r}_i - \vec{R}_I|} + \sum_i \sum_{j>i} \frac{1}{4\pi\varepsilon_0} \frac{e^2}{|\vec{r}_i - \vec{r}_j|}$$
$$+ \sum_I \sum_{J>I} \frac{1}{4\pi\varepsilon_0} \frac{Z_I Z_J e^2}{|\vec{R}_I - \vec{R}_J|}, \tag{2.1}$$

which includes the kinetic energy of the electrons and nuclei, the electron-nucleus interaction, electron-electron interaction and nucleus-nucleus interaction. Here, electrons are denoted by charge e, mass m_e and coordinates $\vec{r}_i$. Nuclei are denoted by atomic number Z_I, charge $Z_I e$, mass M_I and coordinates $\vec{R}_I$.

In theory, one can obtain the many-body wavefunction through solving the many-body Schrödinger equation, from which all properties of the system can be derived. However, the computational cost of solving this equation scales exponentially with the number of particles in the system, due to the interaction terms in Eq. (2.1). This makes practical use near impossible and is known as the many-body problem.

2.1.2 The Born-Oppenheimer approximation

In quantum chemistry, molecular physics and other electronic structure calculations, the Born-Oppenheimer approximation [18] is often used. Its validity stems from the mass of nuclei being much larger than the mass of the electron[2], and as such treats the motion of atomic nuclei and electrons separately[3]. The nuclear kinetic energy (the second term in Eq. (2.1) and $\propto 1/M_I$) is neglected, thereby assuming fixed nuclei. This means the last term, the nucleus-nucleus interaction, is a constant and can therefore be added to the zero of energy. Furthermore, the electron-nucleus interaction (third) term becomes equivalent to the electrons experiencing an external Coulomb potential fixed in space. This leaves a fully electronic Hamiltonian which drastically simplifies

---

[1]Other terms, such as those describing externally applied scalar and vector fields and relativistic effects, can be included. But for now, we have neglected them.

[2]Approximately 1836 times as large for the lightest atomic nucleus, hydrogen.

[3]Mathematically, the wavefunction of a system is separated into an electronic wavefunction and a nuclear wavefunction.

the problem[4].

The Born-Oppenheimer approximation is well justified for many electronic structure calculations, and allows one to focus on the description of electrons. While it has its limitations, its validity remains for our calculations. Therefore, it is used throughout all the work presented in this thesis.

2.1.3 The many-electron Schrödinger equation

As stated above, utilising the Born-Oppenheimer approximation allows us to switch to a fully electron problem where Eq. (2.1) reduces to a many-electron Hamiltonian[5]:

$$\hat{H} = -\frac{1}{2}\sum_i \nabla_i^2 + \sum_i v_{\text{ext}}(\vec{r_i}) + \sum_i \sum_{j>i} \frac{1}{|\vec{r_i} - \vec{r_j}|}, \tag{2.2}$$

where we have rewritten the electron-nucleus interaction as an external potential v_{ext}, felt by all electrons. All observables of the system can be determined, in theory, through solving the Schrödinger equation. Its time-independent form, the time-independent Schrödinger equation (TISE), is given by

$$\hat{H}\Psi_n(\{\vec{r_i}\}) = E_n\Psi_n(\{\vec{r_i}\}), \tag{2.3}$$

whose solutions Ψ_n are the eigenstates (allowed states) of the system. In general, a system will exist in a superposition of these eigenstates $\Psi = \sum_n c_n \Psi_n$, with the expectation value of an observable O, with corresponding Hermitian operator $\hat{O}$, given by

$$\langle O \rangle = \langle \Psi | \hat{O} | \Psi \rangle. \tag{2.4}$$

Ψ is a single-valued, continuous function of $\{\vec{r_i}\}$, which is anti-symmetric with respect to exchange of any two electron coordinates (see Sec. 2.2.3) and normalised ($\langle \Psi | \Psi \rangle = 1$).

A system's eigenstates, and indeed its general many-electron wavefunction, depend on the coordinates of all electrons $\{\vec{r_i}\}$ in an irreducible way, due to the presence of the electron-electron interaction term in Eq. (2.2). For N electrons in three dimensions Ψ is a complex-valued function of $3N$ variables. As such, the many-electron

---

[4]The Born-Oppenheimer approximation still allows the motion of nuclei to be accounted for. E.g., solving the electronic problem for different (stationary) nuclear positions allows the determination of a potential energy surface for the nuclei, which can be used to simulate molecular dynamics.

[5]Hereafter we switch from SI units to Hartree atomic units: $m_{\text{e}} = \hbar = e = 4\pi\varepsilon_0 = 1$.

problem itself is too difficult to solve in any realistic system due to the exponential scaling in computational cost.

The system may also be subject to externally applied potentials, e.g. electric fields, which are included in Eq. (2.2) through v_{ext}. In the case of time-dependent potentials, the system is not static, and the time-evolution of the wavefunction is described by the time-dependent Schrödinger equation (TDSE):

$$\hat{H}\Psi(\{\vec{r}_i\}, t) = i\frac{\partial}{\partial t}\Psi(\{\vec{r}_i\}, t). \tag{2.5}$$

2.2   Density functional theory

Density functional theory (DFT) is an exact reformulation of many-electron quantum mechanics, whose fundamental quantity is the electron density $n(\vec{r})$ rather than the many-electron wavefunction $\Psi(\{\vec{r}_i\})$. This reduces the N-electron problem from a complex-valued function of $3N$ variables to a real-valued function of 3 variables[6]. As such, DFT is a practical, and the most widely used, method for electronic structure calculations.

2.2.1   The Hohenberg-Kohn theorems

The theoretical foundations of DFT were established in 1964 with the theorems developed by Hohenberg and Kohn [1] (HK). The first HK theorem states that the external potential of an N-electron system is a unique functional (up to an additive constant) of the electron density $n(\vec{r})$, where $\int n(\vec{r}) \, d^3r = N$. Hence, the total energy E is also a functional of $n(\vec{r})$, which may be written as [19]

$$
\begin{aligned}
E[n] &= \langle\Psi|\hat{H}|\Psi\rangle \\
&= F[n] + \int n(\vec{r}) \, v_{\text{ext}}(\vec{r}) \, d^3r \\
&= \min_{\Psi \to n}\langle\Psi|\hat{T} + \hat{V}_{\text{ee}}|\Psi\rangle + \int n(\vec{r}) \, v_{\text{ext}}(\vec{r}) \, d^3r,
\end{aligned}
\tag{2.6}
$$

where we have inputted $\hat{H}$ from Eq. (2.2) into Eq. (2.4) and denoted $\hat{T}$ and $\hat{V}_{\text{ee}}$ as the many-electron kinetic energy and electron-electron repulsion operators, respectively. $F[n]$ is some unknown, but universal functional of the density and is known as the HK functional. A corollary of theorem one is that there is a one-to-one mapping between

---

[6]The factor of 3 arises from dimensionality. Later on we restrict ourselves to one dimension (1D) (see Chapter 3), which reduces this factor to 1.

the external potential and ground-state wavefunction, i.e. two different potentials cannot give rise to the same ground-state electron density.

The second HK theorem states that the density that minimises Eq. (2.6) is the true ground-state density n_0:

$$E_0 = E[n_0] = \langle \Psi_0[n_0] | \hat{H} | \Psi_0[n_0] \rangle = F[n_0] + \int n_0(\vec{r}) \, v_{\text{ext}}(\vec{r}) \, d^3r, \qquad (2.7)$$

where Ψ_0 is the ground-state wavefunction.

The power of DFT is that all ground-state properties of a system can, in principle, be expressed as functionals of $n_0(\vec{r})$, without need for $\Psi_0(\{\vec{r}_i\})$.

2.2.2 The Kohn-Sham formalism

A year later in 1965 Kohn and Sham [2] showed that the real system of interacting electrons can be mapped onto an auxiliary system of non-interacting electrons moving in an effective local Kohn-Sham (KS) potential $v_s(\vec{r})$, with both systems yielding the same ground-state electron density. This allows us to rewrite our total energy functional in Eq. (2.6) as

$$\begin{aligned}
E[n] &= F[n] + \int n(\vec{r}) \, v_{\text{ext}}(\vec{r}) \, d^3r \\
&= T[n] + E_{\text{ee}}[n] + \int n(\vec{r}) \, v_{\text{ext}}(\vec{r}) \, d^3r \\
&= T_s[n] + E_{\text{H}}[n] + E_{\text{xc}}[n] + \int n(\vec{r}) \, v_{\text{ext}}(\vec{r}) \, d^3r \\
&= T_s[n] + \int n(\vec{r}) \, v_s(\vec{r}) \, d^3r,
\end{aligned} \qquad (2.8)$$

where T_s are the single-particle kinetic energies, E_{H} is the Hartree energy, and E_{xc} is the exchange-correlation (xc) energy. The first two are known analytically:

$$T_s[n] = T_s[\{\phi_i[n]\}] = -\frac{1}{2} \sum_{i=1}^{N} \int \phi_i^*(\vec{r}) \nabla^2 \phi_i(\vec{r}) \, d^3r, \qquad (2.9\text{a})$$

$$E_{\text{H}}[n] = \frac{1}{2} \int \int \frac{n(\vec{r}) n(\vec{r}')}{|\vec{r} - \vec{r}'|} \, d^3r \, d^3r'. \qquad (2.9\text{b})$$

The non-interacting kinetic energy functional $T_s[n]$ is simply the expectation value of the kinetic energy operator evaluated with the single-particle wavefunction ϕ_i (a KS orbital found from solving the KS equations[7]; see Eq. (2.14)), summed over all oc-

---

[7]While the HK theorems say that, in principle, only the electron density is needed, the KS formalism reintroduces wavefunctions (KS orbitals) as they are needed to evaluate T_s in Eq. (2.9a).

cupied states, while the Hartree energy $E_H[n]$ is the classic Coulomb energy of the electronic charge density. The form of $E_{xc}[n]$ is unknown and its role is to account for the many-electron effects in this non-interacting system by correcting the discrepancies in the many- and single-particle kinetic energies, $T - T_s$, and interaction energies, $E_{ee} - E_H$.

Now, through variation of $E[n]$ with respect to n, we obtain the Euler-Lagrange equation for this functional:

$$\frac{\delta E[n]}{\delta n(\vec{r})} = 0 \implies \frac{\delta F[n]}{\delta n(\vec{r})} + v_{\text{ext}}(\vec{r}) = \frac{\delta T_s[n]}{\delta n(\vec{r})} + v_s(\vec{r}) = \mu, \tag{2.10}$$

where μ is a Lagrange multiplier necessary to constrain the electron number to N. This can only hold if

$$v_s(\vec{r}) = v_{\text{ext}}(\vec{r}) + v_H(\vec{r}) + v_{xc}(\vec{r}), \tag{2.11}$$

where v_H is the Hartree potential:

$$v_H(\vec{r}) = \frac{\delta E_H[n]}{\delta n(\vec{r})} = \int \frac{n(\vec{r}')}{|\vec{r} - \vec{r}'|} d^3 r', \tag{2.12}$$

and v_{xc} is the xc potential:

$$v_{xc}(\vec{r}) = \frac{\delta E_{xc}[n]}{\delta n(\vec{r})}. \tag{2.13}$$

While KS DFT is an exact theory in principle, the functional form of $v_{xc}[n]$, like $E_{xc}[n]$, is unknown and must therefore be approximated in all practical calculations. As the KS electrons are non-interacting, the system is governed by a set of single-particle Schrödinger equations, known as the KS equations:

$$\left(-\frac{\nabla^2}{2} + v_s[n](\vec{r}) \right) \phi_n(\vec{r}) = \varepsilon_n \phi_n(\vec{r}), \tag{2.14}$$

where ε_n is the eigenenergy of the orbital ϕ_n, which is orthonormal to all other orbitals ($\langle \phi_n | \phi_m \rangle = \delta_{nm}$). Summing the squares of the lowest N (occupied) orbitals yields the ground-state density of the non-interacting system:

$$n_0(\vec{r}) = \sum_{i=1}^{N} |\phi_i(\vec{r})|^2, \tag{2.15}$$

which is equal to the ground-state density of the interacting system.

2.2.3 The exchange-correlation functional

The only part of the KS functional that is unknown is the xc term. As such, the accuracy of a practical DFT calculation is determined by the approximation to this term. We now explore it in more detail, along with one of the most common approximations to it.

The exchange-correlation energy $E_{xc}[n]$, by accounting for the many-electron effects, acts to lower the total energy E. It can be split into two components, $E_{xc} = E_x + E_c$. The first of which accounts for the exchange interaction between identical particles. In the case of electrons (fermions), this ensures that the Pauli exclusion principle is obeyed, i.e. two electrons cannot occupy the same quantum state, and acts as a repulsive force between electrons of like spin. Mathematically, this requires the many-electron wavefunction to be antisymmetric with respect to the exchange of two electron coordinates. E.g., for the ground state of a two-electron system:

$$\Psi_0(\{\vec{r_i}\}) = \Psi_0(\vec{r_1}, \vec{r_2}) = -\Psi_0(\vec{r_2}, \vec{r_1}). \tag{2.16}$$

Additionally, the exchange term removes the self-interaction error introduced by the Hartree potential, in which each KS electron spuriously interacts with itself.

The second component accounts for electron correlation, which is the tendency of electrons to "push" electrons out of their vicinity due to their mutual Coulomb repulsion, i.e. their motion is correlated. This manifests in a decrease in the repulsive Hartree potential between each pair of KS electrons, and a difference between the many-electron and single-electron kinetic energies. Like the exchange interaction, electron correlation lowers E.

2.2.3.1 The local density approximation

The local density approximation (LDA) was first proposed by Kohn and Sham in their original 1965 paper [2]. It is the most simple, and one of the most widely used, methods for approximating the xc functional. While the true $E_{xc}[n]$ depends on the electron density in a non-local fashion (e.g. through spatial derivatives of n), the LDA assumes that it depends solely on the local electron density at each point in the system. Specifically:

$$E_{xc}^{LDA}[n] = \int n(\vec{r})\, \varepsilon_{xc}^h(\bar{n})|_{\bar{n}=n(\vec{r})}\, d^3r, \tag{2.17}$$

where $\varepsilon_{xc}^h(\bar{n})$ is the xc energy per electron of a homogeneous electron gas (HEG) of density $\bar{n}$. The HEG is a conceptually important model system containing an infinite number of interacting electrons with a spatially-uniform density $\bar{n} \neq \bar{n}(\vec{r})$. Like the total xc energy E_{xc}, the xc energy per electron of a system can also be split into separate exchange and correlation components, $\varepsilon_{xc} = \varepsilon_x + \varepsilon_c$. The exchange term for the HEG is known analytically:

$$\varepsilon_x^h(\bar{n}) = -\frac{3}{4}\left(\frac{3}{\pi}\right)^{1/3}\bar{n}^{1/3}, \tag{2.18}$$

while no corresponding analytic expression for $\varepsilon_c^h(\bar{n})$ exists. Instead, numerical values for ε_c^h are obtained through quantum Monte Carlo (QMC) calculations, with the original being by Ceperley and Adler [20]. Here, quantum mechanical expectation values (see Eq. (2.4)), which are multi-dimensional integrals, are evaluated using one of several techniques based on the Monte Carlo method. This consists of repeated random sampling to obtain an approximation to the quantity of interest, e.g. ε_c^h. The results are then parameterised to obtain an accurate $\varepsilon_c^h(r_s)$, where r_s is the Wigner-Seitz radius and is related to the density by $4\pi r_s^3/3 = 1/\bar{n}$.

Due to the relative simplicity of $E_{xc}^{LDA}[n]$ in Eq. (2.17), the xc potential in Eq. (2.13) reduces to

$$v_{xc}^{LDA}[n](\vec{r}) = \frac{\delta E_{xc}^{LDA}[n]}{\delta n(\vec{r})} = \varepsilon_{xc}^h(\bar{n})|_{\bar{n}=n(\vec{r})} + n(\vec{r})\frac{d\varepsilon_{xc}^h}{d\bar{n}}\bigg|_{\bar{n}=n(\vec{r})}, \tag{2.19}$$

such that $v_{xc}^{LDA}(\vec{r})$ at each point $\vec{r}$ depends solely on the electron density at that point, $n(\vec{r})$.

The LDA becomes exact in the uniform limit, i.e. $n \neq n(\vec{r})$. No realistic system is perfectly uniform, and so when first proposed, the LDA was expected to perform well in systems where the density was slowly varying. Mathematically, this means $|\nabla n(\vec{r})|/n(\vec{r}) \ll k_F(\vec{r})$, where $k_F(\vec{r})$ is the local Fermi wave vector. The LDA has however performed much better than first predicted, even in situations where the aforementioned conditions are violated. One of the reasons for this is that the LDA is based off a physical system (the HEG) and so it satisfies many of the sum rules of the exact xc functional; e.g. the sum rule to the exchange-correlation hole which ensures that an electron excludes a total charge of one electron from its neighbourhood [21]. There are a number of important cases where the LDA is inadequate and breaks down, and these are discussed at the end of this chapter and in Chapter 4.

2.3 Hartree-Fock theory

The Hartree-Fock method (HF) predates DFT and dominated electronic structure theory calculations for decades, and continues to be widely used today. It originated as an extension of the Hartree equations [22], which were formulated a year after Schrödinger published his own equation, and were the first attempt at replacing the intractable many-body problem with a single-particle approach. While they enjoyed some success, the relative simplicity of the Hartree equations means the resulting approximation to the many-electron wavefunction, a (Hartree) product of the occupied single-electron orbitals, is not exchange-antisymmetric [23, 24].

The HF method [24, 25] corrects this by approximating the many-electron wavefunction for the ground state as a single Slater determinant:

$$\Psi_0(\{\vec{r}_i\}) \approx \Phi^{\mathrm{HF}}(\{\vec{r}_i\}) = \frac{1}{\sqrt{N}} \begin{vmatrix} \phi_1^{\mathrm{HF}}(\vec{r}_1) & \phi_2^{\mathrm{HF}}(\vec{r}_1) & \cdots & \phi_N^{\mathrm{HF}}(\vec{r}_1) \\ \phi_1^{\mathrm{HF}}(\vec{r}_2) & \phi_2^{\mathrm{HF}}(\vec{r}_2) & \cdots & \phi_N^{\mathrm{HF}}(\vec{r}_2) \\ \vdots & \vdots & \ddots & \vdots \\ \phi_1^{\mathrm{HF}}(\vec{r}_N) & \phi_2^{\mathrm{HF}}(\vec{r}_N) & \cdots & \phi_N^{\mathrm{HF}}(\vec{r}_N) \end{vmatrix} \tag{2.20}$$

where $\{\phi_n^{\mathrm{HF}}\}$[8] are the set of solutions to the self-consistent HF equation:

$$\left[-\frac{\nabla^2}{2} + v_{\mathrm{ext}}(\vec{r}) + v_{\mathrm{H}}(\vec{r}) \right] \phi_n^{\mathrm{HF}}(\vec{r}) - \sum_{k=1}^{N} \int d^3r' \, \frac{\phi_k^{\mathrm{HF}*}(\vec{r}')\phi_k^{\mathrm{HF}}(\vec{r})}{|\vec{r}-\vec{r}'|} \, \phi_n^{\mathrm{HF}}(\vec{r}') = \varepsilon_n^{\mathrm{HF}}\phi_n^{\mathrm{HF}}(\vec{r}), \tag{2.21}$$

which is derived through a variational procedure of the expectation value [Eq. (2.4)] of the many-electron Hamiltonian [Eq. (2.2)] with Eq. (2.20).

In contrast to the KS equations of DFT, in which the electrons are moving in an effective *local* potential, the effective potential in Eq. (2.21) is *non-local* due to the last term:

$$v_{\mathrm{x}}^{\mathrm{HF}}(\vec{r},\vec{r}')\phi_n^{\mathrm{HF}}(\vec{r}') = [v_{\mathrm{x}}\,\phi_n^{\mathrm{HF}}](\vec{r}) = -\sum_{k=1}^{N} \int d^3r' \, \frac{\phi_k^{\mathrm{HF}*}(\vec{r}')\phi_k^{\mathrm{HF}}(\vec{r})}{|\vec{r}-\vec{r}'|} \, \phi_n^{\mathrm{HF}}(\vec{r}'), \tag{2.22}$$

where $v_{\mathrm{x}}^{\mathrm{HF}}$ is known as the Fock operator, and Eq. (2.21) reduces to the Hartree approximation if we set $v_{\mathrm{x}}^{\mathrm{HF}} = 0$. This non-locality means that HF is more computationally expensive than DFT, which typically uses simple approximate functionals in practical applications.

---

[8]In general the set $\{\phi_n^{\mathrm{HF}}\}$ are spin orbitals, but here we neglect spin such that they are spatial orbitals.

In HF theory exchange is treated exactly, including complete removal of the spurious electron self-interaction, and so

$$E - E^{\mathrm{HF}} = E - \langle \Phi^{\mathrm{HF}} | \hat{H} | \Phi^{\mathrm{HF}} \rangle = E_{\mathrm{c}}^{\mathrm{HF}}, \qquad (2.23)$$

where the remainder $E_{\mathrm{c}}^{\mathrm{HF}}$ is the correlation energy and is completely neglected. It is worth noting that the exchange energy $E_{\mathrm{x}}^{\mathrm{HF}}$, and $E_{\mathrm{c}}^{\mathrm{HF}}$, are in general not the same as their counterparts in DFT[9]. This arises from Eq. (2.21) being derived from an unconstrained minimisation of E with respect to the single-particle orbitals, which produces the effective *non-local* potential, whereas DFT is restricted to an effective *local* potential.

2.4   Time-dependent density functional theory

Time-dependent DFT (TDDFT) is in principle an exact and efficient theory of the excited-state properties and dynamics of many-electron systems under the influence of time-dependent potentials. An extension to DFT, TDDFT replaces the time-dependent many-electron wavefunction $\Psi(\{\vec{r}_i\}, t)$ with the time-dependent electron density $n(\vec{r}, t)$ as the fundamental quantity.

2.4.1   The Runge-Gross theorem

The time-dependent Schrödinger equation [Eq. (2.5)] defines a unique mapping between a system's time-dependent external potential $v_{\mathrm{ext}}(\vec{r}, t)$ and time-dependent wavefunction $\Psi(\{\vec{r}_i\}, t)$, for a given initial state $\Psi(\{\vec{r}_i\}, t = 0)$ (which is often the ground state, $\Psi_0(\{\vec{r}_i\})$).

The Runge-Gross theorem [10] states that for any fixed initial state $\Psi(\{\vec{r}_i\}, t = 0)$, there is a one-to-one mapping between $n(\vec{r}, t)$ and $v_{\mathrm{ext}}(\vec{r}, t)$, thereby resulting in $v_{\mathrm{ext}}(\vec{r}, t)$ being a unique functional (up to an additive time-dependent constant) of $n(\vec{r}, t)$. Consequently, all observables of a time-dependent system can be be expressed as functionals of $n(\vec{r}, t)$.

---

[9]Certain cases do exist, e.g. the exchange energy of the HEG is defined via the HF method. Here, the omission of correlation leads to errors, such as a broadening of the occupied part of the band structure and a singularity at the Fermi energy – a typical failure of HF in all metals.

2.4.2 Time-dependent Kohn-Sham theory

The KS formalism of ground-state DFT allows us to replace the real interacting system with an auxiliary non-interacting system that has the same ground-state density $n(x)$, thus making DFT a practical theory. We would like to extend this procedure to TDDFT, however the Runge-Gross theorem alone does not guarantee such a procedure is valid.

For this we need the van Leeuwen theorem[10] [11] which proves that for a many-electron system, such as the one described above (with interaction $v_{ee}(\vec{r},\vec{r}') = 1/|\vec{r} - \vec{r}'|$), there exists a different many-electron system with interaction $v'_{ee}(\vec{r},\vec{r}')$ and unique external potential $v'_{ext}(\vec{r},t)$ which yields the same time-dependent density ($n'(\vec{r},t) = n(\vec{r},t)$), provided that the initial state $\Psi'(\{\vec{r}_i\}, t=0)$ is chosen such that $n'(\vec{r}, t=0) = n(\vec{r}, t=0)$ and $\partial_t n'(\vec{r}, t=0) = \partial_t n(\vec{r}, t=0)$. By setting $v'_{ee} = 0$ we have a non-interacting system, which shows that a time-dependent KS scheme is valid. There are certain restrictions, but this is not the case when the initial states of both systems are their respective ground states (many-electron: $\Psi(t=0) = \Psi_0$, Kohn-Sham: $\Phi(t=0) = \Phi_0$), which is the case in all the work presented in this thesis. In these situations, the time-dependent KS (effective) potential $v_s[n, \Psi(t=0), \Phi(t=0)](\vec{r}, t)$ reduces to a density functional $v_s[n](\vec{r}, t)$, which is given by

$$v_s(\vec{r},t) = v_{ext}(\vec{r},t) + v_H(\vec{r},t) + v_{xc}(\vec{r},t). \tag{2.24}$$

Here, $v_H(\vec{r}, t)$ is the time-dependent Hartree potential, whose value at a particular time is obtained through inputting the instantaneous density into Eq. (2.12), and $v_{xc}(\vec{r}, t)$ is the time-dependent xc potential, which like its ground-state counterpart, is unknown. The single-particle orbitals of the KS system evolve according to the time-dependent KS equations:

$$\left(-\frac{\nabla^2}{2} + v_s[n](\vec{r},t) \right) \phi_n(\vec{r},t) = i\frac{\partial}{\partial t} \phi_n(\vec{r},t), \tag{2.25}$$

where the time-dependent density is given by

$$n(\vec{r}, t) = \sum_{i=1}^{N} |\phi_i(\vec{r}, t)|^2. \tag{2.26}$$

---

[10]The Runge-Gross theorem is a particular case of the van Leeuwen theorem, where $v'_{ee} = v_{ee}$, $v'_{ext} = v_{ext}$ and $\Psi'(t=0) = \Psi(t=0)$.

2.4.3 The time-dependent exchange-correlation functional

The time-dependent xc potential $v_{xc}[n]$, is a functional of the density at the present and all previous times. It is the only part of the time-dependent KS potential that is unknown and therefore limits the applicability of TDDFT. Below we outline some of the known properties of the exact v_{xc}, and discuss the commonly employed adiabatic approximation to it.

2.4.3.1 Exact properties

When applied to a one-electron system, the KS potential reduces to the external potential, $v_s(\vec{r}, t) = v_{ext}(\vec{r}, t)$. Therefore, the xc potential must equal the negative of the Hartree potential, to ensure the KS system is self-interaction free:

$$v_{xc}(\vec{r}, t) = -v_H(\vec{r}, t) = -\int \frac{n(\vec{r}')}{|\vec{r} - \vec{r}'|} \, d^3r. \tag{2.27}$$

For any system, as both v_H and v_{xc} originate from the Coulomb repulsion between electrons, they cannot exert a net external force on the system, by Newton's third law. At the level of the xc potential, this means

$$\int n(\vec{r}, t) \nabla v_{xc}(\vec{r}, t) \, d^3r = 0, \tag{2.28}$$

and is known as the *zero-force theorem* [26].

The exact $v_{xc}[n]$ must also obey *generalised translational invariance* [26]: a linearly accelerated observer who resides in a reference frame at position $\vec{x}$ relative to the (original) lab frame will observe a rigidly translated density, $n'(\vec{r}, t) = n(\vec{r} + \vec{x}, t)$, and a rigidly translated xc potential:

$$v_{xc}[n'](\vec{r}, t) = v_{xc}[n](\vec{r}, t)|_{\vec{r} = \vec{r} + \vec{x}}. \tag{2.29}$$

There are two special cases of the above. One is when the observer's frame is moving at constant velocity, such that the translational invariance reduces to *Galilean invariance*. The second is when the system of interacting electrons is confined to a harmonic potential, subject to a uniform electric field at $t = 0$, such that the density rigidly moves in the manner of the underlying classical harmonic oscillator — this is known as the *harmonic potential theorem* [27].

The true v_s, and therefore v_{xc}, are in general functionals of n, $\Psi(t{=}0)$ and $\Phi(t{=}0)$.

These must be independent of which previous instant in the evolution of the system is to be used to designate the initial states, such that

$$v_{\text{xc}}[n, \Psi(t'), \Phi(t')](\vec{r}, t) = v_{\text{xc}}[n, \Psi(t''), \Phi(t'')](\vec{r}, t) \ \ \forall t > t', t'', \quad (2.30)$$

and is known as the *memory condition* [28].

2.4.3.2 The adiabatic approximation

The true time-dependent xc potential is dependent on the present and entire history of the density. However, if the perturbation applied is sufficiently weak, and slow, then the system remains in the instantaneous ground state, i.e. the adiabatic theorem of quantum mechanics [29]. In situations such as this, the exact xc potential at time t depends only on the instantaneous density $n(t)$ [30, 31]:

$$v_{\text{xc}}[n](\vec{r}, t) = v_{\text{xc}}^0[n_0](\vec{r}, t)|_{n_0(\vec{r}) \to n(\vec{r}, t)}, \quad (2.31)$$

where the ground-state xc potential v_{xc}^0 is a functional of the ground-state density n_0.

Most practical functional approximations are adiabatic, and trivially satisfy many of the properties of the exact (non-adiabatic) functional through their complete lack of memory-dependence. The simplest, and one of the most common, is the adiabatic LDA (ALDA) in which the instantaneous density is inputted into the ground-state LDA xc functional [Eq. (2.19)]. While these adiabatic functionals have steadily improved, they prove inadequate in many applications. This is discussed at the end of this chapter and in Chapter 5.

2.5 Linear response

In many applications of TDDFT, such as spectroscopies, the perturbing potential is weak enough to not induce a large density response away from the ground state. Here, first-order perturbation (linear response) theory is valid in which the variation of the system can be described as a functional of the ground-state density[11], i.e. employing ground-state DFT. We introduce this below.

---

[11] We are assuming the initial states Ψ_0 and Φ_0 are non-degenerate ground states. This is often the case in practice, in particular for optical spectra calculations (see Sec. 2.5.4), and is the case in all the work presented in this thesis.

2.5.1   The density-response function

Consider an interacting system, initially in the ground state, with a perturbing potential applied at $t = 0$:

$$v_{\text{ext}}(\vec{r}, t) = v_{\text{ext}}^0(\vec{r}) + \delta v_{\text{ext}}(\vec{r}, t), \tag{2.32}$$

which induces a small response in the electron density, $n(\vec{r}, t) = n_0(\vec{r}) + \delta n(\vec{r}, t)$, where δn may be expressed as a Taylor series with respect to δv_{ext}. In linear response theory, we are only interested in the leading term, and choose to neglect all those of higher-order, such that

$$\delta n(\vec{r}, t) = \int dt' \int d^3 r' \, \chi[n_0](\vec{r}, \vec{r}', t - t') \delta v_{\text{ext}}(\vec{r}', t'), \tag{2.33}$$

where $\chi[n_0](\vec{r}, \vec{r}', t - t')$ is the interacting density-response function[12] and is defined as

$$\chi[n_0](\vec{r}, \vec{r}', t - t') = \left. \frac{\delta n(\vec{r}, t)}{\delta v_{\text{ext}}(\vec{r}', t')} \right|_{v_{\text{ext}}^0}, \tag{2.34}$$

i.e. describing how the density will change at point $\vec{r}$ and time t, if the external potential is changed at point $\vec{r}'$ at an earlier time t'. It can be expressed in terms of the eigenstates of the unperturbed system through the "Lehmann representation" (see Appendix A.1.1):

$$\chi(\vec{r}, \vec{r}', \omega) = \lim_{\eta \to 0^+} \sum_n \left[\frac{\langle \Psi_0 | \hat{n}(\vec{r}) | \Psi_n \rangle \langle \Psi_n | \hat{n}(\vec{r}') | \Psi_0 \rangle}{\omega - (E_n - E_0) + i\eta} - \frac{\langle \Psi_0 | \hat{n}(\vec{r}') | \Psi_n \rangle \langle \Psi_n | \hat{n}(\vec{r}) | \Psi_0 \rangle}{\omega + (E_n - E_0) + i\eta} \right], \tag{2.35}$$

where $|\Psi_0\rangle$, E_0, $|\Psi_n\rangle$ and E_n are the ground state and its energy, and the $n-$th excited state and its energy, respectively, $\hat{n}$ is the density operator in the Heisenberg picture and ω is the frequency of the perturbation. χ has poles at the excitation energies of the system, $E_n - E_0$, and provides a description of neutral excitations[13].

Similarly, the corresponding KS system, upon a small change δv_s in the effective potential, will experience a response in the density:

$$\delta n(\vec{r}, t) = \int dt' \int d^3 r' \, \chi_0[n_0](\vec{r}, \vec{r}', t - t') \delta v_s(\vec{r}', t'), \tag{2.36}$$

which must be the same as that in the interacting system due to both systems having

---

[12]As with v_s, there is no initial-state dependence if the system begins in the ground state.

[13]The first term in the summation corresponds to absorption (poles at positive ω), while the second term corresponds to stimulated emission (poles at negative ω).

the same density at all points in space and time. Here, $\chi_0[n_0](\vec{r}, \vec{r}', t - t')$ is the non-interacting density-response function:

$$\chi_0[n_0](\vec{r}, \vec{r}', t - t') = \frac{\delta n(\vec{r}, t)}{\delta v_s(\vec{r}', t')}\bigg|_{v_s[n_0]}, \tag{2.37}$$

which in the Lehmann representation is given by (see Appendix A.1.2)

$$\chi_0(\vec{r}, \vec{r}', \omega) = \lim_{\eta \to 0^+} \sum_{i,j}(f_i - f_j)\frac{\phi_i^*(\vec{r})\phi_j(\vec{r})\phi_j^*(\vec{r}')\phi_i(\vec{r}')}{\omega - (\varepsilon_j - \varepsilon_i) + i\eta}, \tag{2.38}$$

where the ϕ_i, ε_i are the exact solutions to the Kohn-Sham equations of ground-state DFT [Eq. (2.14)], and f_i is the Fermi occupation (0 or 1) of ϕ_i. In a manner analogous to χ, which has poles at the excitation energies of the interacting system, χ_0 has poles at the excitation energies of the Kohn-Sham system, $\varepsilon_j - \varepsilon_i$.

2.5.1.1 Exact properties

Below we outline some of the basic properties of the exact interacting density-response function. When a perturbation is applied to a system, the induced density response, $\delta n(\vec{r}, t)$ [Eq. (2.33)], must be real, and hence so must $\chi(\vec{r}, \vec{r}', t - t')$. In frequency space, the following result is obtained:

$$\chi(\vec{r}, \vec{r}', \omega) = \chi^*(\vec{r}, \vec{r}', -\omega). \tag{2.39}$$

Substituting the Lehmann representation for χ [Eq. (2.35)] into the above equation leads to the basic symmetry property:

$$\chi(\vec{r}, \vec{r}', \omega) = \chi(\vec{r}', \vec{r}, \omega). \tag{2.40}$$

The positive infinitesimal in Eq. (2.35) means that χ is only analytic in the upper half of the complex plane. Through the use of contour integration techniques, it is possible to relate the real and imaginary parts of χ on the real ω-axis through the Kramers-Kronig relations [32, 33]:

$$\text{Re}\big[\chi(\vec{r}, \vec{r}', \omega)\big] = \mathcal{P}\int\frac{d\omega'}{\pi}\frac{1}{\omega' - \omega}\text{Im}\big[\chi(\vec{r}, \vec{r}', \omega')\big], \tag{2.41a}$$

$$\text{Im}\big[\chi(\vec{r}, \vec{r}', \omega)\big] = -\mathcal{P}\int\frac{d\omega'}{\pi}\frac{1}{\omega' - \omega}\text{Re}\big[\chi(\vec{r}, \vec{r}', \omega')\big]. \tag{2.41b}$$

For any one-electron system, χ simply reduces to the non-interacting density-response function:

$$\chi(\vec{r},\vec{r}',\omega) = \chi_0(\vec{r},\vec{r}',\omega). \tag{2.42}$$

2.5.2 The Dyson equation

By equating Eq. (2.33) and Eq. (2.36) we obtain

$$\int dt' \int d^3r' \, \chi(\vec{r},\vec{r}',t-t')\delta v_{\text{ext}}(\vec{r}',t') = \int dt' \int d^3r' \left[\chi_0(\vec{r},\vec{r}',t-t')\left\{ \delta v_{\text{ext}}(\vec{r}',t') + \right.\right.$$
$$\left.\left. \delta v_{\text{H}}(\vec{r}',t') + \delta v_{\text{xc}}(\vec{r}',t') \right\} \right], \tag{2.43}$$

where we have split v_s into its separate components [Eq. (2.24)]. To calculate the variations of the Hartree and xc components, we utilise the chain-rule for functional derivatives:

$$\delta v_{\text{H}}(\vec{r}',t') = \int dt''dt''' \int d^3r''d^3r''' \, \frac{\delta v_{\text{H}}(\vec{r}',t')}{\delta n(\vec{r}'',t'')} \frac{\delta n(\vec{r}'',t'')}{\delta v_{\text{ext}}(\vec{r}''',t''')} \delta v_{\text{ext}}(\vec{r}''',t''')$$
$$= \int dt''dt''' \int d^3r''d^3r''' \, u(\vec{r}',\vec{r}'')\chi(\vec{r}'',\vec{r}''',t''-t''')\delta v_{\text{ext}}(\vec{r}''',t'''), \quad (2.44\text{a})$$

$$\delta v_{\text{xc}}(\vec{r}',t') = \int dt''dt''' \int d^3r''d^3r''' \, \frac{\delta v_{\text{xc}}(\vec{r}',t')}{\delta n(\vec{r}'',t'')} \frac{\delta n(\vec{r}'',t'')}{\delta v_{\text{ext}}(\vec{r}''',t''')} \delta v_{\text{ext}}(\vec{r}''',t''')$$
$$= \int dt''dt''' \int d^3r''d^3r''' \, f_{\text{xc}}(\vec{r}',\vec{r}'',t'-t'')\chi(\vec{r}'',\vec{r}''',t''-t''')\delta v_{\text{ext}}(\vec{r}''',t'''), \tag{2.44b}$$

where $u(\vec{r},\vec{r}') = 1/|\vec{r}-\vec{r}'|$ is the Coulomb repulsion, and f_{xc} is the xc kernel. Substituting these into Eq. (2.43) and Fourier-transforming to frequency space gives us the relationship between χ and χ_0:

$$\chi(\vec{r},\vec{r}',\omega) = \chi_0(\vec{r},\vec{r}',\omega) + \int d^3r'' \int d^3r''' \left[\chi_0(\vec{r},\vec{r}'',\omega)\left\{ u(\vec{r}'',\vec{r}''') + f_{\text{xc}}(\vec{r}'',\vec{r}''',\omega) \right\} \times \right.$$
$$\left. \chi(\vec{r}''',\vec{r}',\omega) \right], \tag{2.45}$$

which is known as the Dyson equation [34].

If one ignores the classical electron-electron interaction ($u = 0$) and all exchange-correlation effects ($f_{\text{xc}} = 0$), one simply obtains $\chi = \chi_0$. Inputting the correct u but setting $f_{\text{xc}} = 0$ is known as the random phase approximation [35] (RPA) and is equivalent to time-dependent Hartree theory. Typically, one goes beyond both of these and

makes some relatively simple approximation to f_{xc}, e.g. the ALDA.

2.5.3 The exchange-correlation kernel

The xc kernel is defined as

$$f_{\text{xc}}[n_0](\vec{r},\vec{r}',\omega) = \left.\frac{\delta v_{\text{xc}}[n](\vec{r},\omega)}{\delta n(\vec{r}',\omega)}\right|_{n=n_0}, \tag{2.46}$$

and unlike the time-dependent xc potential $v_{\text{xc}}[n]$, is solely a functional of the ground-state density n_0. Nevertheless, it is an intricate quantity and its functional form remains unknown. Below we outline some of the known properties of the exact f_{xc}, and discuss the commonly employed adiabatic approximation to it. It is also convenient to define f_{xc} in terms of χ and χ_0 through manipulation of the Dyson equation [Eq. (2.45)]:

$$f_{\text{xc}}(\vec{r},\vec{r}',\omega) = \chi_0^{-1}(\vec{r},\vec{r}',\omega) - \chi^{-1}(\vec{r},\vec{r}',\omega) - u(\vec{r},\vec{r}'). \tag{2.47}$$

2.5.3.1 Exact properties

The density-response function χ is symmetric in $\vec{r}$ and $\vec{r}'$ [Eq. (2.40)], as is χ_0, leading to f_{xc} having the same property:

$$f_{\text{xc}}(\vec{r},\vec{r}',\omega) = f_{\text{xc}}(\vec{r}',\vec{r},\omega). \tag{2.48}$$

Both $v_{\text{xc}}(\vec{r},t)$ and the density response $\delta n(\vec{r},t)$ are real-valued functions, and therefore $f_{\text{xc}}(\vec{r},\vec{r}',t-t') = \delta v_{\text{xc}}(\vec{r},t)/\delta n(\vec{r}',t')|_{n_0}$ is also real. Consequently, it becomes complex in frequency space and satisfies

$$f_{\text{xc}}(\vec{r},\vec{r}',\omega) = f_{\text{xc}}^*(\vec{r},\vec{r}',-\omega), \tag{2.49}$$

in the same manner as χ [Eq. (2.39)] and χ_0.

χ is only analytic in the upper half of the complex ω-plane, which results in a connection between its real [Eq. (2.41a)] and imaginary [Eq. (2.41b)] parts through the Kramers-Kronig relations. Furthermore, it is also invertible in this upper plane. As this is also true for χ_0, Eq. (2.47) means we can define the following Kramers-Kronig relations for f_{xc}:

$$\text{Re}\left[f_{\text{xc}}(\vec{r},\vec{r}',\omega)\right] = \text{Re}\left[f_{\text{xc}}(\vec{r},\vec{r}',\infty)\right] + \mathcal{P}\int\frac{d\omega'}{\pi}\frac{\text{Im}\left[f_{\text{xc}}(\vec{r},\vec{r}',\omega')\right]}{\omega'-\omega}, \tag{2.50a}$$

$$\text{Im}\big[f_{\text{xc}}(\vec{r},\vec{r}',\omega)\big] = -\mathcal{P}\int \frac{d\omega'}{\pi}\, \frac{\text{Re}\big[f_{\text{xc}}(\vec{r},\vec{r}',\omega')\big] - \text{Re}\big[f_{\text{xc}}(\vec{r},\vec{r}',\infty)\big]}{\omega'-\omega}. \tag{2.50b}$$

The exact conditions of v_{xc} also yield results for f_{xc}. By taking the functional derivative of Eq. (2.28) and applying some further manipulation, we arrive at

$$\int f_{\text{xc}}(\vec{r},\vec{r}',\omega)\nabla' n_0(\vec{r}')\, d^3r' = \nabla v_{\text{xc}}^0(\vec{r}), \tag{2.51}$$

which ensures f_{xc} satisfies the zero-force theorem. Additionally, taking the functional derivative of Eq. (2.27) leads to the following requirement for a one-electron system:

$$f_{\text{xc}}(\vec{r},\vec{r}',\omega) = -u(\vec{r},\vec{r}'), \tag{2.52}$$

which guarantees that the KS system is self-interaction free.

2.5.3.2   The adiabatic approximation

By considering a system under the influence of a static perturbation $\delta v_{\text{ext}}(\vec{r})$, with the corresponding KS system experiencing a change in effective potential $\delta v_s(\vec{r})$, linearising the KS equations of ground-state DFT [Eq. (2.14)] gives the $\omega = 0$ (static) limit of f_{xc}:

$$f_{\text{xc}}(\vec{r},\vec{r}',0) = \frac{\delta v_{\text{xc}}^0[n_0](\vec{r})}{\delta n_0(\vec{r}')} = \frac{\delta^2 E_{\text{xc}}[n_0]}{\delta n_0(\vec{r})\delta n_0(\vec{r}')}, \tag{2.53}$$

which is purely real.

While the exact $f_{\text{xc}}(\vec{r},\vec{r}',\omega)$ is, in general, complex, spatially non-local and ω-dependent, most practical applications utilise an adiabatic approach, i.e. ignoring the ω-dependence, and thereby the imaginary component through Eq. (2.49). Of particular use is the ALDA, which is also spatially local:

$$f_{\text{xc}}^{\text{ALDA}}(\vec{r},\vec{r}') = \left.\frac{d^2\varepsilon_{\text{xc}}^h(\bar{n})}{d\bar{n}^2}\right|_{\bar{n}=n_0(\vec{r})}\delta(\vec{r}-\vec{r}'), \tag{2.54}$$

and has been derived by taking the functional derivative of Eq. (2.19).

Adiabatic TDDFT functionals are heavily used, and while there have been some successes, they prove inadequate in many applications of linear response theory. This is discussed at the end of this chapter.

2.5.4 Optical absorption spectra

TDDFT can be applied to a wide variety of important spectroscopies. If the perturbing electromagnetic field is weak enough, as is the case in optical (visible light) absorption spectra calculations of molecules and solids, we are sufficiently in the linear response regime. Furthermore, as the wavelength of visible light is typically much larger than the typical length scale of the system we can work in the dipole approximation, in which we neglect this spatial variation in the perturbing field. Here, the perturbing potential takes the form $\delta v_{\text{ext}}(\vec{r}, t) = \mathcal{E} x \cos(\omega t)$, which represents a monochromatic electric wave with amplitude $\mathcal{E}$ and angular frequency ω polarised along the x-axis, where the magnetic field component is weak enough to be neglected. A quantity of interest in spectroscopy is the photoabsorption cross-section $\sigma(\omega)$ [Fig. 2.1], otherwise known as the absorption spectrum, which provides a measure of how much of the incident radiation is absorbed by the system, and can be calculated from the imaginary part of the density-response function (see Appendix A.2):

$$\sigma(\omega) = -\frac{4\pi\omega}{c} \int d^3r \int d^3r' \, \text{Im}\left[\chi(\vec{r}, \vec{r}', \omega)\right] x \, x', \qquad (2.55)$$

where c is the speed of light.
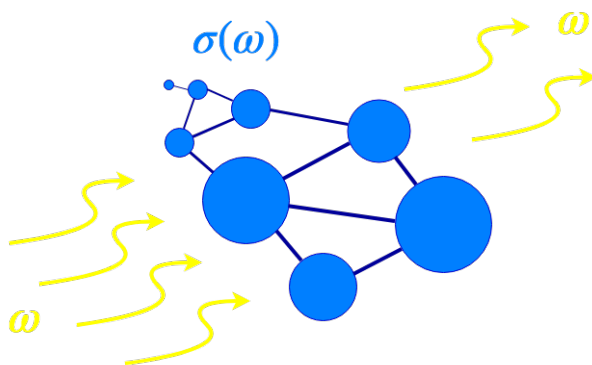
Fig. 2.1. If monochromatic light of angular frequency ω is incident on a system, such as a molecule, the photoabsorption cross-section $\sigma(\omega)$ gives a measure of how much of the light is absorbed by the system: σ multiplied by the intensity of the light I will give the total power absorbed P.

2.6 Limitations of practical applications

2.6.1 Ground-state calculations

DFT is the most widely used method to perform ground-state electronic structure calculations in condensed matter physics and many areas of materials science. It is computationally efficient and often provides better accuracy than more expensive methods, such as HF. However, its application is restricted by the limitations of available approximate xc functionals. These functionals can be arranged into a hierarchy of approximations, known as Jacob's ladder [36], with the first rung on the ladder being the LDA, which remains widely used in DFT calculations.

Despite its simplicity the LDA performs much better than first predicted: atomic and molecular ground-state energies, molecular equilibrium distances and geometries, Fermi surfaces of bulk metals, lattice constants of solids and vibrational frequencies and phonon energies in a wide range of materials are all close to their experimental values [37]. One of the reasons for the success of the LDA is error cancellation: exchange energies are typically overestimated, while correlation energies are typically underestimated [38, 39]. This stems from the LDA being based on a real, physical system (the HEG) and the fact that it satisfies a variety of exact sum rules [21].

While LDAs have been hugely successful in many cases [40, 41], their validity breaks down in a number of important situations, particularly when there is strong correlation. They are known to miss out some key features present in the exact xc functional. A notable failing is the inability to correctly cancel the spurious electron self-interaction [3, 7, 8], introduced by the Hartree potential. A consequence of this is the exponential decay of the LDA xc potential far from a finite system [3, 6], rather than following the Coulomb-like $-1/r$ decay present in the exact v_{xc} [5, 6]; see Fig. 2.2 for the example of the Helium atom. This results in errors in the energies of the KS orbitals [42], such as the HOMO, and hence the ionisation energy. It also prevents the modelling of negative ions, which are unstable when using the LDA, even when they are known to be stable through experiment. Binding energies also tend to be overestimated, with this more pronounced in finite systems. LDAs also fail to capture the derivative discontinuity [4, 9], the discontinuous nature of the derivative of the xc energy with respect to electron number N, at integer N. This leads to incorrect band gaps in solids, as well as the wrong dissociation limit of molecules, resulting in incorrect distributions of fractional charges [37]. In general, the LDA is good at qualitatively

describing physical properties, and has been instrumental in the application of DFT to electronic structure calculations, but is not sufficient for a variety of applications requiring "chemical accuracy" [37].
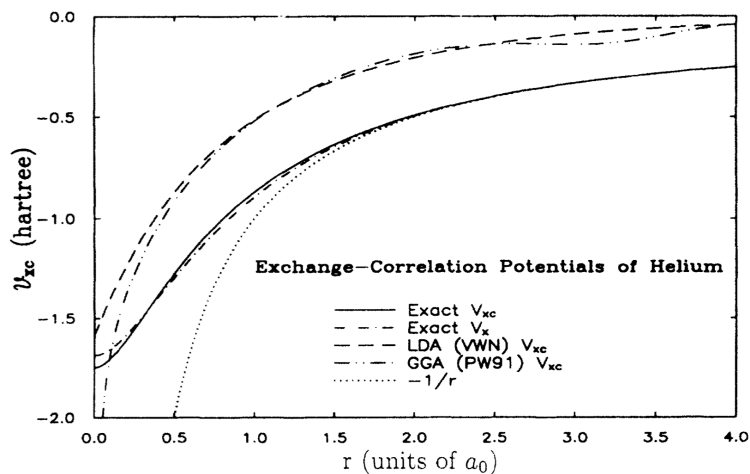
Fig. 2.2. The exact v_{xc} for the Helium atom, along with those obtained using the LDA (VWN [43]) and GGA (PW91 [44]), which have the wrong asymptotic behaviour due to their local and semi-local dependence on the density. (Figure 10 in Ref. 45.)

The second rung on Jacob's ladder of DFT is the generalised gradient approximation [46] (GGA). A step up from the LDA, the xc energy density in the GGA, $\varepsilon_{xc}^{GGA}(n(\vec{r}), \nabla n(\vec{r}))$, is dependent on the local density and its spatial gradient, and is therefore a semi-local functional. GGAs offer marked improvements and correct some of the deficiencies present in LDAs. While generally giving good xc energies, the associated xc potentials are less reliable, displaying the same incorrect asymptotic behaviour as the LDA [Fig. 2.2]. While integrated quantities such as energies are good, they sometimes overcompensate, e.g. often underestimating binding energies [47]. Additionally, they too are not sufficient for many chemical applications. Climbing the ladder leads to significant increases in computational cost which limit practical use.

2.6.2 Time-dependent calculations

The vast majority of applications of TDDFT are in the linear-response regime, with the aim of determining the excited-state properties of a wide variety of many-electron systems. This includes a number of important spectroscopies, including optical spectroscopy, with the general objective being to accurately describe the density response, excitation energies and absorption spectra of atoms, molecules and solids. While it offers a unique compromise between accuracy and computational efficiency, and has

resulted in much success, linear-response TDDFT still poses problems in many important circumstances. We discuss some of these below.

2.6.2.1 Single excitations

In a typical TDDFT calculation, computing χ through the Dyson equation [Eq. (2.45)] is a two-step process. First, a ground-state DFT calculation must be performed to compute χ_0 from the KS orbitals [Eq. (2.38)], which will not be the true χ_0 as some approximation to v_{xc} must be used. Second, an approximation to f_{xc} must be made, whose job is to shift the KS excitations onto the true excitations.

Generally, in finite systems e.g. atoms and small molecules, the choice of approximate ground-state functional used in the first step is the most important factor [48]. However, the use of some approximate kernel, i.e. going beyond the RPA, improves significantly upon the bare KS excitations, the choice of which becomes more important in systems with strong correlation [48]. For low-lying single excitations, good results are obtained using local, e.g. the LDA/ALDA, and semi-local functionals. Higher excitations, such as a Rydberg series, tend to be poorly described due to the incorrect asymptotic decay of v_{xc} in these functionals, with these excitations underestimated or not bound at all [7, 48–52]. This distinction in the performance of the LDA/ALDA tends to occur near the ionisation threshold ($-\varepsilon_{\text{HOMO}}^{\text{LDA}}$) [53], which is significantly lower than the true ionisation potential due to the incorrect exponential decay of v_{xc} [54]; the examples of N_2 and CO molecules are illustrated in Fig. 2.3. This failure to describe higher excitations can be rectified to some extent through asymptotically corrected functionals [7, 50, 55], or more sophisticated exact-exchange methods [56, 57] and hybrid functionals [58–63].

2.6.2.2 Multiple excitations

One of the biggest challenges is to describe multiple excitations. In a non-interacting system, a multiple excitation results from several electrons each absorbing a photon and being promoted to a higher-energy orbital, e.g. a double excitation describes the promotion of two electrons. However, only the single-particle excitations of the KS system are captured by the KS response function χ_0, with all multiple excitations absent. Therefore, the exact f_{xc} has to not only shift the single-particle excitations,
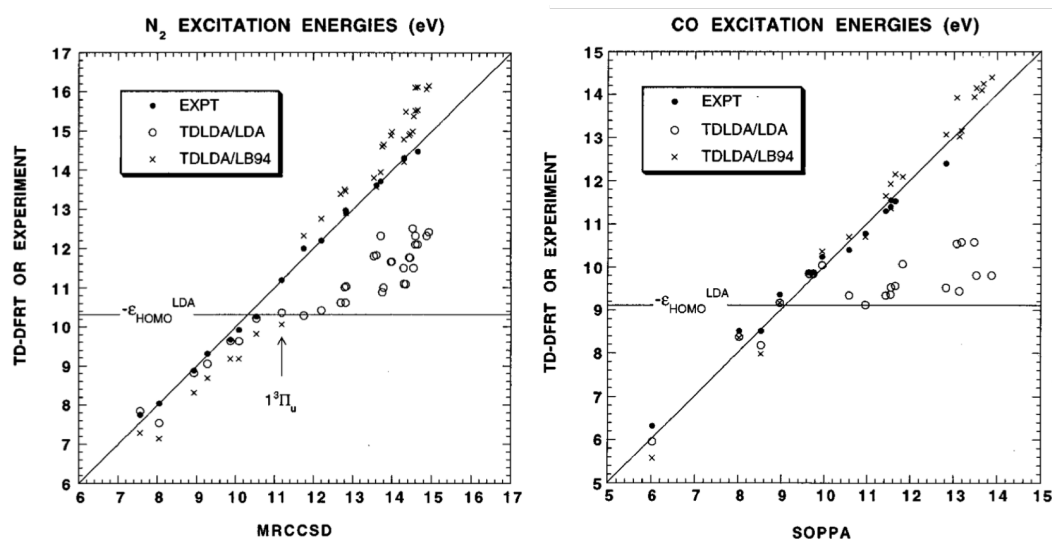
Fig. 2.3. Left: The first 35 vertical excitation energies of N_2 computed using the ALDA (TDLDA) kernel, with the ground-state v_{xc} used being either that of the LDA or the LB94 [55] which has the correct asymptotic behaviour. Also plotted are some experimental results and those obtained using a high-level theoretical method [64] (MR-CCSD). While the TDLDA/LDA performs well for the lowest excitations, it fails above the ionisation threshold, while the TDLDA/LB94 holds, demonstrating the importance of the long-range behaviour of the xc potential. (Figure 1 in Ref. 49.) Right: Similar to the left panel, but now plotting the first 23 vertical excitation energies of CO, and using an alternative theoretical method [65] (SOPPA). Again, the LDA proves insufficient above the ionisation threshold. (Figure 2 in Ref. 49.)

but introduce additional poles to describe the missing multiple excitations[14]. While adiabatic kernels tend to describe single-particle excitations well, *all* are incapable of describing multiple excitations as strong ω-dependence is known to be necessary [66–71]; an example is illustrated in Fig. 2.4.
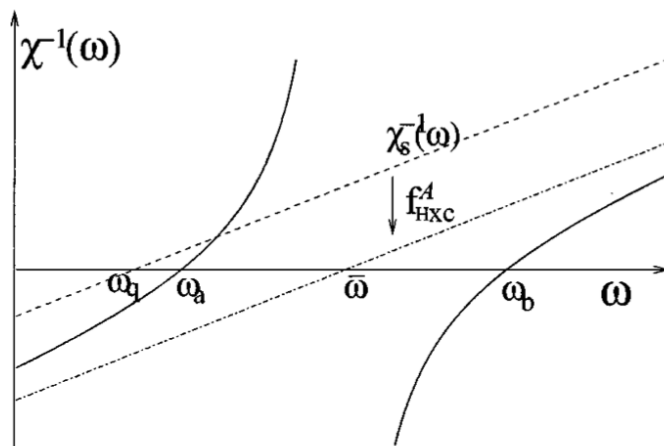
Fig. 2.4. The exact density-response functions when a double excitation mixes with a single excitation, well separated from the other excitations, in the limit that the Coulomb interaction is weak: The inverse of the KS response function χ_s^{-1} passes through zero at the single excitation ω_q, which an adiabatic kernel ($f_{Hxc}^A = f_{xc}^A + u$) shifts to $\bar{\omega}$. The inverse of the interacting response function χ^{-1} passes through zero at the true excitation energies, ω_a and ω_b, and displays strong frequency-dependence, which must also be present in the true xc kernel ($f_{xc} = \chi_s^{-1} - \chi^{-1} - u$). (Figure 1 in Ref. 66.)

2.6.2.3   Charge-transfer excitations

In systems that have regions of charge density spatially separated from one another, and so can be viewed as separate subsystems, charge can transfer from one subsystem to another. These types of processes are known as charge-transfer excitations and are not well described by standard TDDFT functionals. Consider an electron moving from one subsystem (the donor) to another (the acceptor), separated by a distance R. The lowest charge-transfer excitation energy ω_{ct}, is known exactly in the large separation limit:

$$\lim_{R \to \infty} \omega_{ct}^{\text{exact}} = I_d - A_a - \frac{1}{R}, \tag{2.56}$$

---

[14]Multiple excitations are less well defined in an interacting system. If one was to expand a many-electron excited state in the complete basis of single-electron orbitals, a doubly-excited state would be one dominated by a double-excited Slater determinant.

where I_d is the ionisation potential of the donor, A_a is the electron affinity of the acceptor and the last term is the electrostatic interaction energy of the electron-hole pair that has been created. In the large separation limit, the overlap between the occupied (HOMO in the donor) and unoccupied (LUMO in the acceptor) orbitals vanishes. Consequently, local (e.g. LDA) and semi-local (GGA) functionals yield an excitation energy equal to this orbital energy difference, $\varepsilon_a^L - \varepsilon_d^H$ [8, 72]. In the exact Kohn-Sham system $I_d = -\varepsilon_d^H$, and $A_a = -\varepsilon_a^L - \Delta_{xc}^a$, where Δ_{xc}^a is the xc correction to the KS gap of the acceptor. The LDA, GGA, etc. tend to underestimate the KS eigenvalues and completely neglect Δ_{xc}^a. Along with missing out the $-1/R$ term, this results in a significant underestimation of ω_{ct}.

Improved results are obtained through range-separated hybrids [73–77], which mix a TDDFT functional with Hartree-Fock, which treats exchange exactly. If one were to calculate excitation energies through full time-dependent HF theory, one would find Eq. (2.56) reducing to $\omega_{ct}^{HF} = \varepsilon_a^{L,HF} - \varepsilon_d^{H,HF} - 1/R$, with $I_d - A_a$ being well approximated by the difference in eigenvalues as a consequence of Koopmans' theorem [78], and the $-1/R$ term arising from the exchange integral, thereby describing charge-transfer excitations qualitatively correctly. This class of hybrid functionals, which reduce to full HF exchange at large R, offers an improvement over pure TDDFT methods; an example is illustrated in Fig. 2.5. Exact exchange (EXX) TDDFT, implemented through the optimised effective potential (OEP), is another approach which is capable of describing charge-transfer excitations [79, 80].

One case where all of the above fail is charge transfer between open-shell fragments [81, 82]. Here, the HOMO of the donor and LUMO of the acceptor are delocalised over the whole system. Although this means there is finite overlap between them, their energy difference approaches zero in the limit of large separation. Hence, the charge-transfer energy has to be described entirely by f_{xc} (plus the Coulomb repulsion), which must diverge with interatomic separation and have strong ω-dependence [31].

2.6.2.4 Semiconductors and insulators

Simple TDDFT functionals, e.g. ALDA, generally perform well in metallic systems, improving upon the RPA. This is less so for non-metallic systems. While electron energy loss spectra [83] (EELS) are well described in many semiconductors and insu-
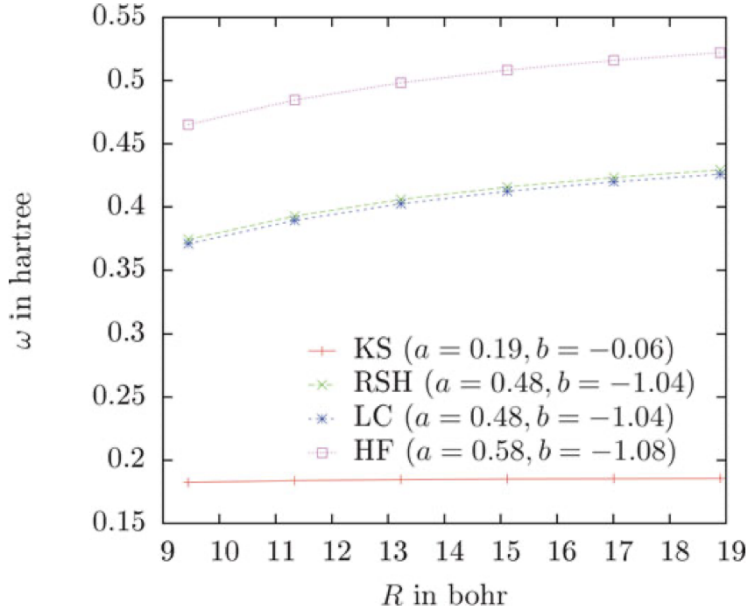
Fig. 2.5. The lowest charge-transfer excitation energy of the $C_2H_4 - C_2F_4$ dimer for increasing R, calculated using the ALDA (KS), Hartree-Fock (HF) and two range-separated hybrids (LC, RSH). Both hybrids show the correct $-1/R$ behaviour at large R, given by the HF exchange term, and are a significant improvement on the ALDA. (Figure 6 in Ref. 77.)

lators, the optical absorption spectra[15] are often poor [84]. The two main issues are underestimation of the optical gap (the energy at which continuous absorption begins), and missing out the excitonic peaks, which are created by electron-hole pair interactions. The example of bulk silicon is illustrated in Fig. 2.6. Both of these problems require a long-ranged f_{xc} [85–88] ($1/q^2$ behaviour in Fourier space), which is not the case for local (the ALDA is q-independent) and semi-local functionals. In order to correct the optical gap, an imaginary component of f_{xc} is also needed [87], which means the kernel must be ω-dependent [Eq. (2.49)], and is therefore beyond the capability of adiabatic functionals.

Attempts to address one or both of the above issues include EXX methods [89], and adding long-range contributions to f_{xc}, through long-range corrected kernels [84, 86, 88, 90], meta-GGAs [91] and hybrid functionals [88, 92]. Another approach involves calculations of the homogeneous electron gas [93–96]. Kernels derived from the Bethe-Salpeter equation (BSE) have had much success [97–99], but require an expensive many-body perturbation theory calculation involving the manipulation of large matrices as their input, severely limiting their applicability, and are outside the KS

---

[15]In the long wavelength limit, $q \to 0$.

TDDFT framework. Hence, this provides the motivation for the development of improved approximate TDDFT functionals.
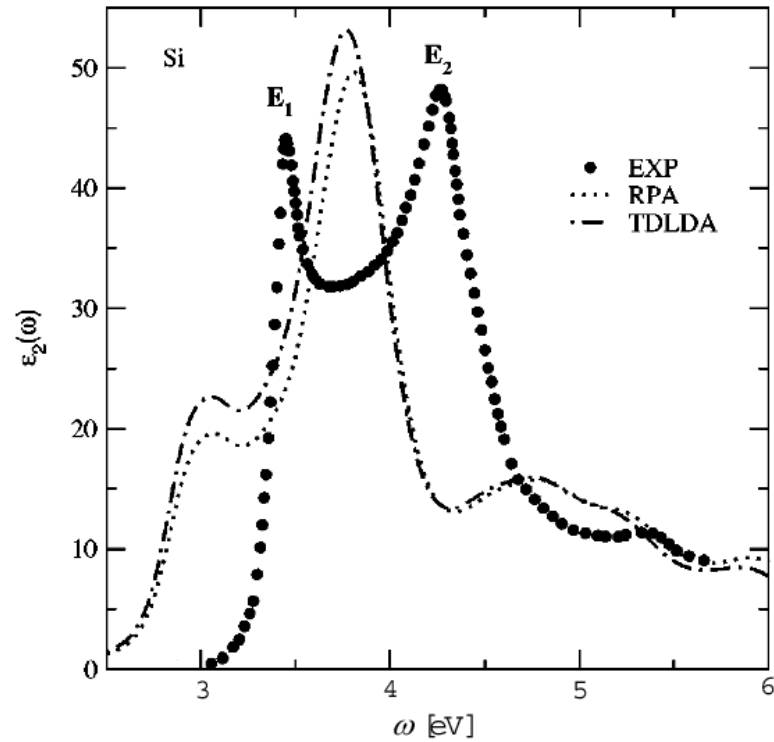
Fig. 2.6. The optical absorption spectrum of bulk silicon. Both the RPA and ALDA (TDLDA) underestimate the optical gap and fail to reproduce the excitonic peak. (Figure 3 in Ref. 100, reproduced from Figure 1 in Ref. 84.)

METHOD

In Chapter 2 we introduced many-electron quantum mechanics and its exact description of matter on the atomic scale. The equations governing it cannot be solved in practice due to the computational scaling with the number of particles and so other methods, such as time-dependent density-functional theory, must be used. In general these must be implemented numerically as analytic solutions do not exist. In this chapter, we outline how we perform the electronic structure calculations for the research presented in this thesis. Our approach is to study small, prototype systems of a few electrons, where we can solve the many-electron Schrödinger equation exactly, to within machine precision. Using optimisation methods, we can then determine the exact ground-state and time-dependent Kohn-Sham potential. This allows us to identify features present in the exact exchange-correlation functional that are missing from the commonly used approximations, in order to inform the development of improved approximate functionals. We can also implement approximations, both established and novel, to test their performance against the exact solutions.

3.1 The iDEA code

3.1.1 General overview

The interacting Dynamic Electrons Approach [17] (iDEA) is a Python-Cython [101, 102] software suite developed in Rex Godby's research group at the University of York since 2010. As mentioned on the previous page, the iDEA code models small, one-dimensional[1] prototype systems of spinless electrons for which we can compute exact solutions. Various approximate functionals (established and novel) have also been implemented for comparison. We choose to restrict ourselves to one dimension (1D) as this allows us to calculate the exact, fully-correlated many-electron wavefunction for a system of interacting electrons, i.e. thereby including exact electron exchange and correlation.

Spinless electrons obey the Pauli principle but are restricted to a single spin type. There are certain limitations to their use – they cannot model, for example, singlet and triplet states, or the formation of electron pairs through chemical bonding. However, these are not necessary for the research presented in this thesis. Meanwhile, the use of spinless electrons gives us access to richer correlation as they exhibit features that would need a larger number of spin-half electrons to become apparent, e.g. two spinless electrons experience the exchange effect, which is not the case for two spin-half electrons in an $S = 0$ state. Furthermore, spinless KS electrons occupy a greater number of KS orbitals, thereby increasing correlation.

Below we discuss in more detail the components of iDEA which were instrumental for the research presented in this thesis, with much of the functionality developed by the author[2].

3.1.2 Many-electron quantum mechanics implementation

The most computationally demanding part of iDEA involves generating the solutions to the TISE [Eq. (2.3)] and TDSE [Eq. (2.5)][3]. At present, this can be done for systems of up to four electrons, under the influence of an arbitrarily defined external potential

---

[1]The entirety of the work presented in this thesis was generated using iDEA and so we switch to one dimension hereafter.
[2]This development and testing is discussed in more detail in Sec. 3.1.5.
[3]A particularly expensive many-electron calculation can take approximately a few days to obtain well converged results.

$v_{\text{ext}}(x, t)$, and interacting via the softened Coulomb repulsion:

$$u(x, x') = \frac{1}{|x - x'| + a} \tag{3.1}$$

where $a = 1$ is an appropriate softening parameter to avoid a singularity at $x = x'$ [103][4].

3.1.2.1 The exact ground state

The first step is to calculate the ground state of the system through solving the TISE. This, along with most differential equations cannot in general be solved analytically, and must be done so numerically. In iDEA we do this through finite-difference methods on a real-space grid[5], i.e. the position variable x becomes discretised, functions becomes vectors and operators becomes matrices. We consider the many-electron Hamiltonian [Eq. (2.2)] in 1D:

$$\hat{H} = -\frac{1}{2} \sum_i \frac{\partial^2}{\partial x_i^2} + \sum_i v_{\text{ext}}(x_i) + \sum_i \sum_{j > i} u(x_i, x_j), \tag{3.2}$$

which becomes the Hamiltonian matrix:

$$H = \begin{vmatrix} H_{11} & H_{12} & \cdots & H_{1P} \\ H_{21} & H_{22} & \cdots & H_{2P} \\ \vdots & \vdots & \ddots & \vdots \\ H_{P1} & H_{P2} & \cdots & H_{PP} \end{vmatrix} \tag{3.3}$$

where $H_{ab} = \langle e_a | \hat{H} | e_b \rangle$. Here, e_a and e_b are members of some basis set $\{e_\mu\}$ that spans the Hilbert space. As we work on a real-space grid we employ the position basis: this can be visualised as a set of top-hat functions centred on each grid point that approach delta functions as the grid spacing $\delta x \to 0$. Therefore, $P = G^N$, where G is the number of grid points sampling the N-electron system, and the Hamiltonian matrix elements

---

[4] In Ref. 103 it is determined that $a = 1$ is the most appropriate. While our numerical results depend to some extent on the chosen value of a, the general conclusions drawn do not.

[5] We use a uniform grid spacing in iDEA: $x_{j+1} - x_j = \delta x \; \forall \; j$. We converge our results with respect to δx, and typically find ~ 100 grid points is sufficient to obtain ground-state densities that are close to machine precision. See Appendix C for details on the calculations presented in this thesis.

become

$$H_{ab} = \langle x_1, x_2, \ldots, x_N | \left\{ -\frac{1}{2} \sum_i \frac{\partial^2}{\partial x_i^2} + \sum_i v_{\text{ext}}(x_i) + \sum_i \sum_{j>i} u(x_i, x_j) \right\} | x_1', x_2', \ldots, x_N' \rangle,$$
(3.4)

where $|x_1', x_2', \ldots, x_N'\rangle$ is the position eigenstate with the $i-$th electron located at position x_i'. We approximate the second-order derivative using a stencil (see Appendix B.2).

Solving the TISE with H will generate exchange-antisymmetric (fermionic) and exchange-symmetric (bosonic) eigenvectors. In order to restrict ourselves to the fermionic eigenvectors, we construct a reduction matrix R, which restricts us to a subspace where $x_1 > x_2 > \ldots > x_N$; a fermionic wavefunction must be zero unless all the $x_1, x_2, \ldots, x_N$ are different, and other permutations follow from exchange-antisymmetry. The Hamiltonian matrix in this reduced space is given by RHR^T. If we determine the normalised eigenvectors $\{\psi_m\}$ of this reduced Hamiltonian, then the set of normalised, exchange-antisymmetric eigenvectors $\{\Psi_m\}$ of the full Hamiltonian can be obtained via $\Psi_m = R^T \psi_m$ (or vice versa, $\psi_m = R\Psi_m$).

After constructing the reduced Hamiltonian matrix we pass it to a linear algebra routine[6] from the SciPy library [105], which computes the eigenvectors and eigenvalues. The eigenvectors of the full Hamiltonian then follow from the procedure outlined above. The exact ground-state electron density is then determined by

$$n_0(x) = N \int dx_2 \int dx_3 \cdots \int dx_N \, |\Psi_0(\{x_i\})|^2,$$
(3.5)

where we have relabelled $x_1 = x$.

The method described above is used in Chapter 5 and Chapter 6. The results in Chapter 4 were generated using an earlier version of iDEA. Here, after constructing the Hamiltonian matrix, a trial wavefunction Ψ is chosen as an initial guess to Ψ_0, the true ground state[7]. This trial wavefunction can be expanded in the basis of the many-electron eigenstates of the system as they form a complete set, $\Psi = \sum_m c_m \Psi_m$. Upon propagation in imaginary time τ[8], it becomes (see Appendix B.1)

$$\Psi(\{x_i\}, \tau) = \sum_m c_m e^{-E_m \tau} \, \Psi_m(\{x_i\}),$$
(3.6)

---

[6]The 'eigsh' routine from the linear algebra section of the SciPy library which uses the Implicitly Restarted Lanczos Method [104].

[7]Typically a Hartree-Fock calculation is performed as this provides a reasonable starting point.

[8]We use the Crank-Nicolson method (see Appendix B.1.1: CN-method).

which allows us to calculate the ground state of the system:

$$E_{m+1} > E_m \ \forall \ m \implies \lim_{\tau \to \infty} \Psi(\{x_i\}, \tau) = \Psi_0(\{x_i\}), \tag{3.7}$$

provided that we ensure Ψ is correctly normalised.

3.1.2.2 The exact excited states

The linear algebra routine (eigsh) from the SciPy library allows more than one eigenvector (and corresponding eigenvalue) to be calculated, and so we use this to determine the excited states of the system.

In the earlier version of iDEA we used the Gram-Schmidt algorithm to compute the excited states. Eq. (3.7) shows that as we propagate a trial wavefunction through imaginary time we converge to the ground state of the system. After we have done this, as long as we "project out" the ground state at each imaginary time step[9], a trial wavefunction will converge to the first excited state of the system. The second excited state can then be calculated using the same method, but we now project out both the ground state and the first excited state, and so on. The Gram-Schmidt algorithm orthonormalises a set of linearly-independent vectors in an inner product space. In iDEA this corresponds to the many-electron eigenstates in Hilbert space, spanned by the position basis. To calculate the $m-$th excited state, i.e. ensuring the RHS of Eq. (3.7) $= \Psi_m$, we project out the previously determined states from the trial wavefunction at each time step:

$$\Psi(\{x_i\}, \tau) \longrightarrow \Psi(\{x_i\}, \tau) - \sum_{k=0}^{m-1} \langle \Psi | \Psi_k \rangle \Psi_k. \tag{3.8}$$

The excited states are necessary for calculations performed in Chapter 6. Some of the initial calculations, including those presented in Ref. 106, relied on the earlier method. We have verified these results by comparing with the new, improved method.

3.1.2.3 Exact time propagation

In the spirit of linear response theory, we take our system to initially be in the ground state, with a perturbation δv_{ext} applied at $t = 0$. We use static perturbations, i.e. representing switch-on processes, such that the Hamiltonian operator does not explicitly depend on time. In this case, the time-evolution operator [Eq. (A.1.14)] reduces to

---

[9]Just as we use uniform grid spacings, we also use uniform time steps: $t_{j+1} - t_j = \delta t$, $\tau_{j+1} - \tau_j = \delta \tau \ \forall \ j$.

$\hat{U}(t) = -it\hat{H}$, and the solution to the TDSE is trivial:

$$\Psi(\{x_i\}, t) = e^{-it\hat{H}}\Psi(\{x_i\}, t = 0). \tag{3.9}$$

From this we determine

$$\Psi(\{x_i\}, t) = e^{-i\delta t H}\Psi(\{x_i\}, t - \delta t), \tag{3.10}$$

which tells us how to compute the wavefunction at each time step from the wave-function at the previous time step $(t - \delta t)$[10]. We have replaced $\hat{H}$ with its matrix representation H, as numerically this constitutes a matrix equation. We solve this using a linear algebra routine from the SciPy library which computes the matrix exponential in Eq. (3.10) using a Padé approximant. At each time step, after determining the wavefunction, we calculate the exact time-dependent electron density by

$$n(x, t) = N \int dx_2 \int dx_3 \cdots \int dx_N \, |\Psi(\{x_i\}, t)|^2, \tag{3.11}$$

and relabel $x_1 = x$.

The old version of iDEA used the Crank-Nicolson method for this real time propagation, as it did for the imaginary time propagation (see Appendix B.1.1). No results presented in this thesis rely on this method, and so we neglect to discuss it in detail.

3.1.3 Kohn-Sham DFT/TDDFT implementation

One of the key functions of iDEA is the determination of the exact ground-state and time-dependent KS potential. This is done by reverse-engineering the exact electron density through optimisation procedures. This is discussed below.

3.1.3.1 Exact ground-state reverse-engineering

Until a perturbation is applied at $t = 0$, both the interacting and KS systems are in their respective ground state. To determine the exact KS potential we use a two-step process. The first step involves initialising with a trial potential, e.g. $v_s = v_{\text{ext}}$, and

---

[10]As we do with grid spacing, we converge out results with respect to δt, and typically find this must be smaller than δx. We find the choice of time step to be particularly important for the time-dependent reverse-engineering algorithm (see Sec. 3.1.3.2), which also requires a well converged ground state to avoid propagation of error. See Appendix C for details on the calculations presented in this thesis.

iteratively correct using the procedure

$$v_s(x) \longrightarrow v_s(x) + \mu \left[n'(x)^p - n(x)^p \right].$$ (3.12)

Here, μ and p are both constants which can be adjusted to optimise the rate of convergence of the trial density $n'(x)$, which is calculated through solving the ground-state KS equations [Eq. (2.14)] with the trial potential[11], to the exact ground-state density $n(x)$. This procedure raises the trial potential in regions where the trial density is too high ($n' > n$), lowers it in regions where the trial density is too low ($n' < n$), and clearly has the correct fixed point at $n' = n$. As we are working on a discretised grid, we calculate the mean absolute error (MAE) by summing over all grid points x_j:

$$\text{MAE} = \frac{1}{G} \sum_{j=1}^{G} |n'(x_j) - n(x_j)|.$$ (3.13)

Typically, the procedure outlined above generates MAE $\sim 10^{-12}$ and was used to generate the results in Chapter 4. The new version of iDEA involves a second step to reduce the MAE further. This invokes a root finder function from the SciPy library which uses a Powell hybrid method [107] to find the correct $v_s(x)$ such that $f(x) = 0 \; \forall \; x$. Here, $f(x)$ is the residual function:

$$f(x) = \frac{|n'(x) - n(x)|}{\sqrt{n(x)}},$$ (3.14)

where the square root emphasises the value of the residual in the low-density regions. Through this we reduce the error to machine precision, MAE $\sim 10^{-16}$.

3.1.3.2 Exact time-dependent reverse-engineering

A static perturbing field is applied to the interacting system at $t = 0$, such that $v_{\text{ext}}(x, t) = v_{\text{ext}}^0(x) + \delta v_{\text{ext}}(x)$. We initialise the trial KS potential to be $v_s(x, t = 0) = v_s^0(x) + \delta v_{\text{ext}}(x)$, and use the root finder to find the exact $v_s(x, t = 0)$: the time-dependent KS equations [Eq. (2.25)] are solved across one step, i.e. the occupied ground-state KS orbitals are propagated from $t = 0 \rightarrow t = \delta t$ (using the single-particle version of Eq. (3.10)), which gives access to $n'(x, t = \delta t)$. The trial potential is corrected to find the exact $v_s(x, t = 0)$, such that $n'(x, t = \delta t) = n(x, t = \delta t)$, i.e. the residual function

---

[11]We construct the single-particle Hamiltonian matrix and diagonalise to find the eigenvectors and eigenvalues.

[Eq. (3.14)] is minimised. To determine $v_s(x, t = \delta t)$ (the next time step), we take the trial potential to be the exact $v_s(x, t = 0)$, and use the root finder to correct it such that the time-dependent KS equations are satisfied across $t = \delta t \rightarrow t = 2\,\delta t$. We then repeat for all time steps, giving us access to the exact $v_s(x, t)$ [Fig. 3.1]. In general, this means finding the root of the residual function at each time step:

$$f(x, t) = \frac{|n'(x, t) - n(x, t)|}{\sqrt{n(x, t)}}. \tag{3.15}$$

As the time-dependent density matches that of the interacting system, the current density j also matches via the continuity equation:

$$\frac{\partial}{\partial t} n(x, t) + \frac{\partial}{\partial x} j(x, t) = 0. \tag{3.16}$$
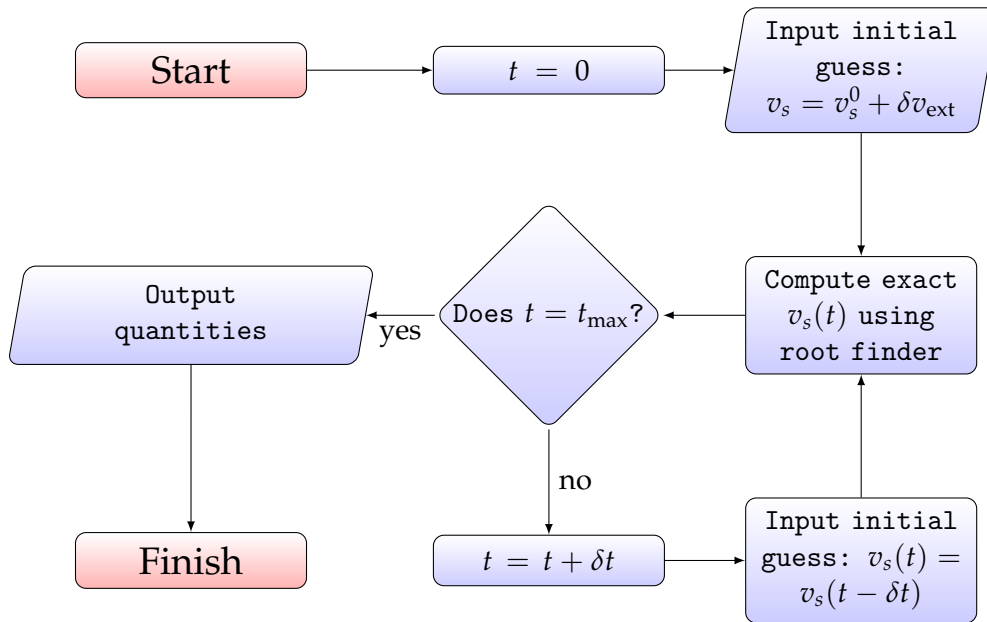
Fig. 3.1. A flowchart describing the time-dependent reverse-engineering algorithm in iDEA, used to calculate the exact $v_s(x, t)$.

3.1.3.3 Self-consistent LDA calculations

The ground-state KS equations [Eq. (2.14)] constitute a non-linear eigenproblem: the density one obtains from solving them [Eq. (2.15)] is required as their input due to the functional dependence of $v_s[n]$. In order to solve them, some sort of self-consistent field (SCF) procedure must be used, of which there are many [108]. Finding a solution is what it means to attain self-consistency.

We have implemented various SCF methods in iDEA in order to test the performance of approximate functionals, e.g. the LDA, against the exact solution, which we have determined through our reverse-engineering algorithm. These include conjugate gradient minimisation [109], Pulay mixing [110], mixing the Hamiltonian matrix directly and linear mixing of the KS potential. The linear mixing scheme is the simplest, most widely used and is illustrated in Fig. 3.2. Once we have used the LDA to determine the approximate ground-state solution, we simply apply it adiabatically [Eq. (2.31)] to solve the time-dependent KS equations [Eq. (2.25)], i.e. through inputting the ground-state xc functional [Eq. (2.19)]. Details of our calculations, including the LDA xc functionals used, are given in Chapter 4.
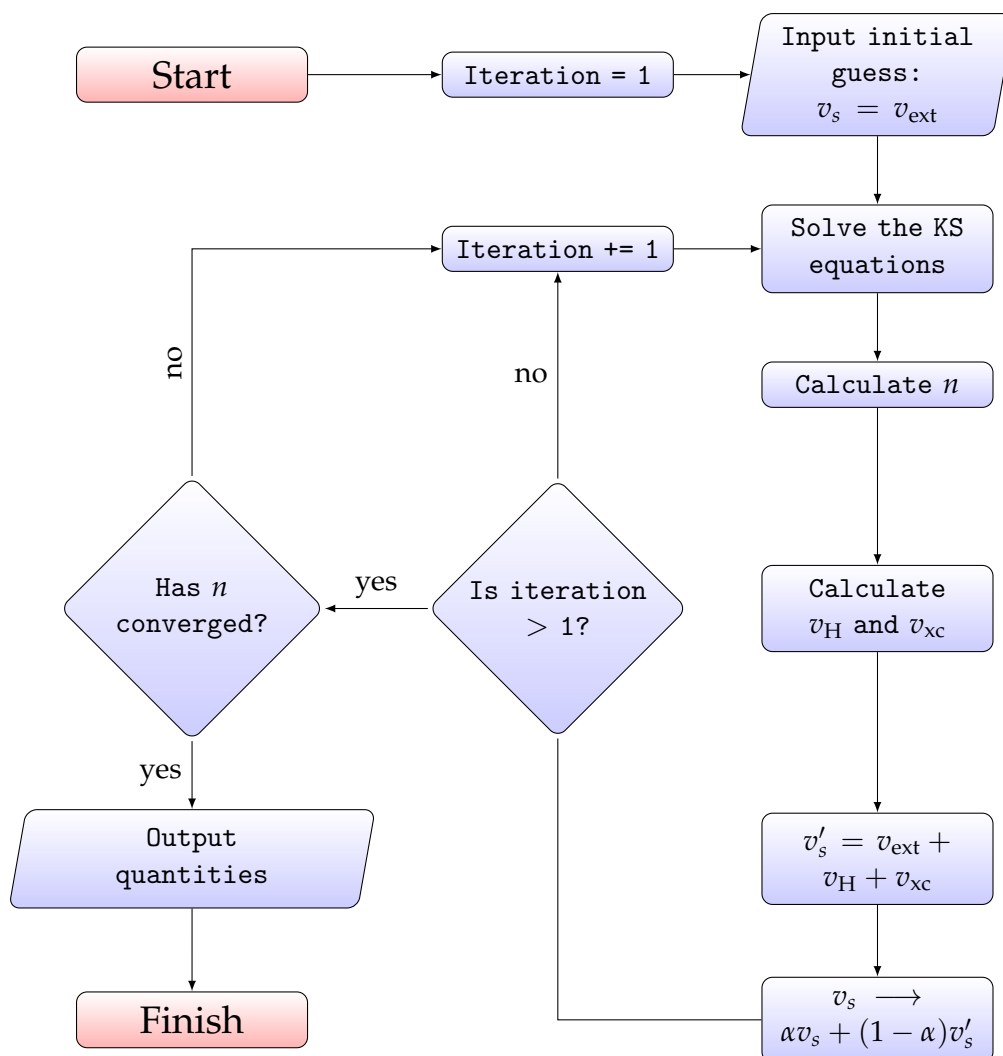
Fig. 3.2. A flowchart describing the linear mixing scheme: one of the many schemes used to perform self-consistent ground-state LDA calculations in iDEA.

3.1.4   Linear response implementation

After solving the many-electron Schrödinger equation exactly and reverse-engineering the electron density to determine the exact KS system, we are able to calculate the exact interacting and non-interacting density-response functions, χ and χ_0, and hence the exact xc kernel f_{xc}. As well as identifying its properties, this allows us to analyse the performance of common approximations, e.g. the RPA and ALDA. We discuss this below.

3.1.4.1   The density-response functions

We have obtained the many-electron eigenstates $\{\Psi_m\}$ through solving the many-electron Schrödinger equation, which allows us to calculate the exact χ [Eq. (2.35)]. We make use of the following identity:

$$\lim_{b \to 0^+} \frac{1}{a + ib} = \mathcal{P}\left(\frac{1}{a}\right) - i\pi\delta(a), \tag{3.17}$$

from which we obtain the imaginary part of χ:

$$\text{Im}\big[\chi(x, x', \omega)\big] = \pi \sum_n \Big[- \langle\Psi_0|\hat{n}(x)|\Psi_n\rangle\langle\Psi_n|\hat{n}(x')|\Psi_0\rangle\, \delta(\omega - (E_n - E_0))$$

$$+ \langle\Psi_0|\hat{n}(x')|\Psi_n\rangle\langle\Psi_n|\hat{n}(x)|\Psi_0\rangle\, \delta(\omega + (E_n - E_0))\Big]. \tag{3.18}$$

The amplitudes ($\langle\Psi_0|\hat{n}(x)|\Psi_n\rangle$ etc.) are determined from the many-electron eigenstates (see Appendix B.3.1). It is customary to replace the positive infinitesimal η in Eq. (2.35) with a small positive number[12], such that the δ functions in the above expression become Lorentzian distributions:

$$f(\omega, \pm(E_n - E_0), \gamma) = \frac{1}{\pi\gamma} \frac{\gamma^2}{(\omega \mp (E_n - E_0))^2 + \gamma^2}, \tag{3.19}$$

where $\omega = \pm(E_n - E_0)$ specifies the peak of the distribution and γ is a scale parameter. The Kramers-Kronig relation [Eq. (2.41a)] allows us to calculate the real part of χ from

---

[12]This broadens the peaks in the optical absorption spectrum [Eq. (2.55)] for ease of viewing. The specific values we use in our calculations are given in Appendix C.3.

the imaginary part:

$$\text{Re}\big[\chi(x,x',\omega)\big] = \mathcal{P}\int \frac{d\omega'}{\pi}\,\frac{1}{\omega'-\omega}\text{Im}\big[\chi(x,x',\omega')\big]$$

$$= \sum_n \left[\frac{\langle \Psi_0|\hat{n}(x)|\Psi_n\rangle\langle\Psi_n|\hat{n}(x')|\Psi_0\rangle}{(\omega-(E_n-E_0))^2+\gamma^2}\,(\omega-(E_n-E_0)) \right.$$
$$\left. - \frac{\langle\Psi_0|\hat{n}(x')|\Psi_n\rangle\langle\Psi_n|\hat{n}(x)|\Psi_0\rangle}{(\omega+(E_n-E_0))^2+\gamma^2}\,(\omega+(E_n-E_0)) \right]. \qquad (3.20)$$

We calculate the real and imaginary components of the exact χ_0 [Eq. (2.38)] in a similar manner:

$$\text{Im}\big[\chi_0(x,x',\omega)\big] = \pi\sum_{i,j}(f_j-f_i)\,\phi_i^*(x)\phi_j(x)\phi_j^*(x')\phi_i(x')\,f(\omega,\varepsilon_j-\varepsilon_i,\gamma), \qquad (3.21a)$$

$$\text{Re}\big[\chi_0(x,x',\omega)\big] = \mathcal{P}\int\frac{d\omega'}{\pi}\,\frac{1}{\omega'-\omega}\text{Im}\big[\chi_0(x,x',\omega')\big]$$
$$= \sum_{i,j}(f_i-f_j)\frac{\phi_i^*(x)\phi_j(x)\phi_j^*(x')\phi_i(x')}{(\omega-(\varepsilon_j-\varepsilon_i))^2+\gamma^2}\,(\omega-(\varepsilon_j-\varepsilon_i)). \qquad (3.21b)$$

3.1.4.2 The exact exchange-correlation kernel

The Dyson equation [Eq. (2.45)] in 1D is written as

$$\chi(x,x',\omega) = \chi_0(x,x',\omega) + \int dx''\int dx'''\left[\chi_0(x,x'',\omega)\big\{u(x'',x''')+f_{\text{xc}}(x'',x''',\omega)\big\}\times\right.$$
$$\left.\chi(x''',x',\omega)\right].$$
$$(3.22)$$

This can be rearranged to give an expression for the xc kernel:

$$f_{\text{xc}}(x,x',\omega) = \chi_0^{-1}(x,x',\omega) - \chi^{-1}(x,x',\omega) - u(x,x'), \qquad (3.23)$$

which we can calculate as we have access to the exact χ and χ_0. However, the inverses of χ and χ_0 are not well defined. For instance, a spatially uniform perturbation, $\delta v_{\text{ext}}(x,\omega) = c(\omega)$, induces no change in density for all ω, so both χ and χ_0 have a zero eigenvalue and therefore a zero determinant. Numerical methods are employed to overcome this, and are discussed in Chapter 6.

3.1.4.3 Applying the RPA and ALDA

As discussed in Chapter 2, computing χ through the Dyson equation is a two-step process in a practical TDDFT calculation. First, a ground-state DFT calculation must be performed to compute χ_0, which will not be the true χ_0 as some approximation to v_{xc} must be used. Second, an approximation to f_{xc} must be made. Both of these introduce error into the final χ that is computed through the Dyson equation.

In iDEA, unlike in practical calculations, we are able to generate exact solutions. Therefore, when analysing the performance of the RPA ($f_{xc} = 0$) and ALDA kernels [Eq. (2.54)], we can choose to start from the exact χ_0, or some approximate χ_0, e.g. constructed from the ground-state LDA orbitals. This allows us to clearly distinguish between both sources of error. The RPA and ALDA were used to generate results presented in Chapter 6 and more detail is given there.

3.1.4.4 Computing the optical absorption spectrum

The optical absorption spectrum [Eq. (2.55)] in 1D is given by

$$\sigma(\omega) = -\frac{4\pi\omega}{c} \int dx \int dx' \, \mathrm{Im}\big[\chi(x, x', \omega)\big] \, x \, x'. \tag{3.24}$$

We compute this for the interacting system by inputting Eq. (3.18) into the above expression. If we input Eq. (3.21a) instead, we obtain $\sigma(\omega)$ for the exact KS system[13]. Finally, if we perform an RPA or ALDA calculation, we simply input the imaginary component of the approximate χ that was computed.

3.1.5 Development and testing of iDEA

iDEA has been developed over several years with improvements made to existing code structure and the addition of new functionality. Below we discuss the components of iDEA that were created by the author and appropriate testing of the code.

3.1.5.1 Many-electron module

The many-electron module existed in a more rudimentary form but was substantially rewritten by the author, including through the development of Cython extensions. This achieved a speedup factor of ~ 20 for a typical ground-state calculation and ~ 10

---

[13]We have computed the exact ground-state KS potential, and hence orbitals, to give us the exact χ_0. The $\sigma(\omega)$ that follows is that of the exact KS system.

for a typical time propagation. The Gram-Schmidt algorithm was also implemented, allowing the initial computation of excited states, which were used for the calculations presented in Ref. 106. This was replaced with the improved method of computing the excited states through the linear algebra routine from the SciPy library.

Unit tests had been developed previously for the ground-state calculation and time propagation, and we checked that the improved many-electron module continued to pass them all. This included generating numerical results for a variety of systems and comparing to previously obtained results, as well as checking the results obtained for systems with known solutions, e.g. electrons in a harmonic potential with the Coulomb repulsion set equal to zero. We also used this system of non-interacting electrons to test the implementation of the Gram-Schmidt algorithm, i.e. the calculation of the excited states. After this test was passed, we increased the Coulomb repulsion from zero to a fraction of its true strength, i.e. $u(x, x') = \alpha(|x - x'| + 1)^{-1}$, where $\alpha \ll 1$. We then checked that the corrections to the eigenvalues of the excited states agreed with those obtained from first-order perturbation theory. When the Gram-Schmidt algorithm was replaced with the SciPy routine, we verified that these tests continued to be passed.

3.1.5.2 Reverse-engineering module

The ground-state reverse-engineering module was also rewritten to achieve speedups in calculations, and to include the root finder, thereby reaching machine precision when determining the KS potential. We ran the code for several systems that we had previously generated results for (including in published papers) and verified that the results obtained were the same.

The time-dependent reverse-engineering initially used a different type of algorithm that often failed[14]. Therefore, this was modified to more closely resemble the ground-state algorithm, including the use of the root finder (as discussed in Sec. 3.1.3.2). Again, we checked the results against those obtained from previous versions of the code.

3.1.5.3 LDA module

The LDA module was originally developed by the author and used the linear mixing scheme [Fig. 3.2]. Improvements were made, such as the addition of other SCF

---

[14]This has not been discussed as no results presented in this thesis were generated from it.

methods, by other researchers in the group. The code uses novel LDA xc functionals (see Chapter 4) and therefore known results do not exist. In order to test this module, we first verified that the results obtained using the linear mixing scheme reduces to Hartree theory if we set $v_{\mathrm{xc}} = 0$. Secondly, we checked that each SCF method converges to the same result as one another for a variety of systems (including where $v_{\mathrm{xc}} \neq 0$).

3.1.5.4 Linear response module

The linear response module was developed by the author[15]. The first set of tests consisted of setting the Coulomb interaction to zero and checking that χ (constructed from the many-electron eigenstates) and χ_0 (constructed from the KS orbitals) were equal to one another, for a variety of systems. As a further test, we computed the ground-state density n_0, and many-electron eigenstates, and hence χ, of two interacting electrons[16] in a harmonic potential. We then computed the ground-state density n_0', of two interacting electrons in the same harmonic potential but with a weak linear field applied, i.e. $v_{\mathrm{ext}} \to v_{\mathrm{ext}} + \varepsilon x$. We checked that χ obeyed (the Fourier transform of) Eq. (2.33) at $\omega = 0$: $\delta n = n_0' - n_0 = \int \chi \varepsilon x \, dx'$. We repeated the test for the KS system by verifying that χ_0 obeyed (the Fourier transform of) Eq. (2.36) at $\omega = 0$: $\delta n = \int \chi_0 \, \delta v_s \, dx'$.

By inverting χ and χ_0 we obtain f_{xc}. In every calculation we then input f_{xc} and χ_0 into the Dyson equation. We check that the resultant χ is equal to the exact χ. We also verify that f_{xc} satisfies the zero-force sum rule [Eq. (2.51)]. This is discussed in more detail in Chapter 6.

---

[15]The inversion of the density-response functions to obtain f_{xc} was improved by Nick Woods, a collaborator, and is discussed in Chapter 6.
[16]We repeated this test for three interacting electrons as well.

LOCAL DENSITY FUNCTIONALS BASED ON ELECTRON GAS AND FINITE SYSTEMS[1]

As discussed in Chapter 2, a widely used approximation to the exchange-correlation (xc) functional in ground-state density functional theory (DFT) is the local density approximation (LDA), typically derived from the properties of the homogeneous electron gas (HEG). In this chapter, we introduce a set of alternative LDAs constructed from one-dimensional systems of one, two, and three electrons that resemble the HEG within a finite region. We also construct a HEG-based LDA appropriate for spinless electrons in one dimension. By comparing the finite and HEG LDAs with one another we demonstrate that local approximations constructed from finite systems are a viable alternative, and explore the nature of any differences between them. As expected, all LDAs are inadequate in low-density systems where correlation is strong. However, we find that the finite LDAs give better densities and energies in high-density exchange-dominated systems, arising partly from a better description of the self-interaction correction.

---

[1]This chapter represents collaborative work that has been published: M. T. Entwistle, M. Casula and R. W. Godby, 'Comparison of local density functionals based on electron gas and finite systems', *Phys. Rev. B* **97**, *235143 (2018)*. The sections of this chapter have been adapted from the publication. Additionally, some of the introductory remarks and background work relate to a previous paper: M. T. Entwistle, M. J. P. Hodgson, J. Wetherell, B. Longstaff, J. D. Ramsden and R. W. Godby, 'Local density approximations from finite systems', *Phys. Rev. B* **94**, *205134 (2016)*. The research presented in this previous paper was conducted before I became a PhD student.

4.1   Introduction

The LDA [2] (see Sec. 2.2.3.1) is a widely used approximation in DFT and assumes that the true xc functional is solely dependent on the electron density at each point in the system. LDAs are traditionally derived from knowledge of the xc energy of the HEG [20], a model system where the exchange energy[2] is known analytically and the correlation energy[3] is usually calculated using quantum Monte Carlo simulations. LDAs have been hugely successful in many cases [40, 41], however, their validity breaks down in a number of important situations [83, 111–118], particularly when there is strong correlation. They are known to miss out some critical features that are present in the exact xc potential (see Sec. 2.6.1), such as the cancellation of the spurious electron self-interaction [3, 7, 8], or the Coulomb-type $-1/r$ decay of the xc potential far from a finite system [5, 6], instead following an incorrect exponential decay [3, 6]. This results in errors in the energies of the KS orbitals [42], such as the HOMO, and hence the ionisation energy. Binding energies also tend to be overestimated. Furthermore, LDAs fail to capture the derivative discontinuity [4, 9, 119, 120], the discontinuous nature of the derivative of the xc energy with respect to electron number N, at integer N. This leads to incorrect band gaps in solids, as well as the wrong dissociation limit of molecules, resulting in incorrect distributions of fractional charges [37].

In a previous paper[4] [121], we introduced a set of LDAs which, in contrast to the traditional HEG LDA, were constructed from systems of one, two, and three electrons which resembled the HEG within a *finite* region. Illustrating our approach in one dimension (1D), we found that the three LDAs were remarkably similar to one another. In this chapter, we construct a 1D HEG LDA through suitable diffusion Monte Carlo [122] (DMC) techniques, along with a revised set of LDAs constructed from finite systems. We compare the finite and HEG LDAs with one another to demonstrate that local approximations constructed from finite systems are a viable alternative, and explore the nature of any differences between them. Broadly, we wish to understand the strengths and weaknesses of alternative approaches to constructing local xc functionals, in order to tailor approximations for use in ab initio calculations. This may also prove useful when extending functionals to the time-dependent regime.

---

[2]We take the exchange energy to be the exchange energy of a self-consistent Hartree-Fock calculation.
[3]We take the correlation energy to be the difference between the exact energy of the many-electron system and the energy of a self-consistent Hartree-Fock calculation.
[4]The research presented in this previous paper was conducted before I became a PhD student.

In order to test the LDAs, we employ the iDEA code [17] (described in Chapter 3) to solve the many-electron Schrödinger equation exactly for model finite systems in order to determine the exact, fully-correlated, many-electron wave function. Using this to obtain the exact electron density, we then utilise the reverse-engineering algorithm to find the exact KS system. In our calculations we use spinless electrons which interact via the appropriately softened Coulomb repulsion [103] $(|x - x'| + 1)^{-1}$.

4.2 Set of LDAs

4.2.1 LDAs from finite systems

In Ref. 121 we chose a set of finite locally homogeneous systems in order to mimic the HEG, which we referred to as "slabs" [Fig. 4.1]. We generated sets of one-electron ($1e$), two-electron ($2e$), and three-electron ($3e$) slab systems over a typical density range (up to 0.6 a.u.) and in each case calculated the exact xc energy E_{xc}. From this we parameterised the xc energy density $\varepsilon_{xc} = E_{xc}/N$ in terms of the electron density of the plateau region of the slabs, repeating for the $1e$, $2e$, and $3e$ set. To generate these slab systems we developed an optimisation module[5] (in iDEA) which finds the correct external potential v_{ext} for a target system with a desired electron density $n_T(x)$[6]. After making an initial guess for the system, the exact many-body wave function is calculated and v_{ext} is refined iteratively, following the method used for the ground-state KS potential (see Sec. 3.1.3.1). To approximate the xc energy of an inhomogeneous system, the LDA focuses on the local electron density at each point in the system:

$$E_{xc}^{LDA}[n] = \int n(x)\varepsilon_{xc}(n) \, dx,$$
(4.1)

where in a conventional LDA $\varepsilon_{xc}(n)$ is the xc energy density of a HEG of density n. This approximation becomes exact in the limit of the HEG, and so it is a reasonable requirement for the finite LDAs to become exact in the limit of the slab systems.

Due to the initial parameterisation of $\varepsilon_{xc}(n)$ focusing on the plateau regions of the slabs (i.e. ignoring the inhomogeneous regions at the edges), we used a *refinement process* [121] in order to fulfil this requirement. This involved applying each LDA to the set of slab systems from which it was constructed. Small errors in the

---

[5]The optimisation module was not needed for the $1e$ slab systems as E_{xc} is known exactly in $1e$ systems: it is the negative of the Hartree energy [Eq. (2.9b)].
[6]See Appendix C.1.1 for the parametric form of the slab systems.
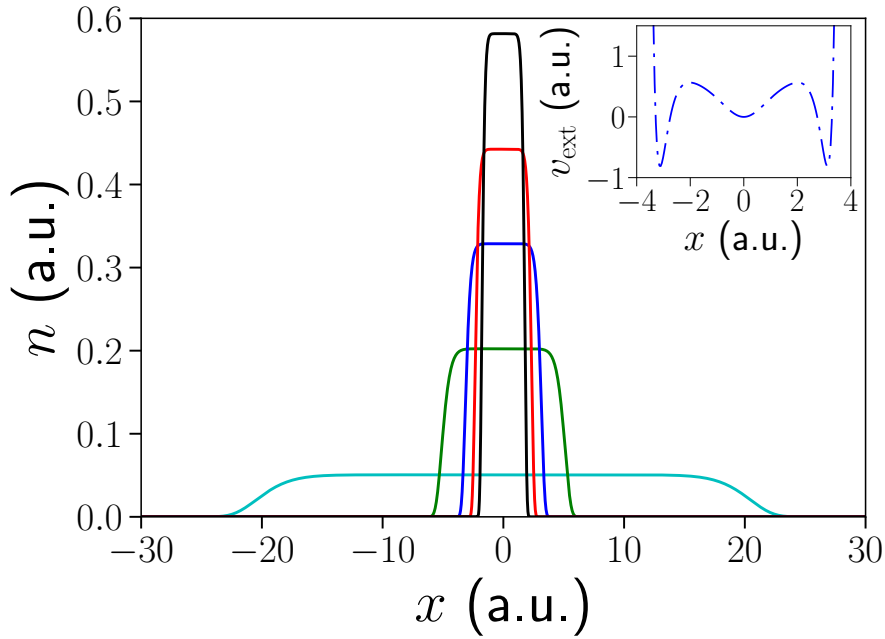
Fig. 4.1. The exact many-body electron density (solid lines) for a selection of the two-electron slab systems. The density is locally homogeneous across a plateau region and decays exponentially at the edges. Inset: the external potential for a typical two-electron slab system (middle density in main figure).

xc energy ΔE_{xc} were found due to neglecting the regions of inhomogeneous density. These calculated errors were then used to determine refined forms for ε_{xc} in the LDAs , $\varepsilon_{xc}(n) \to \varepsilon_{xc}(n) - \Delta E_{xc}(n)/N$. These refined forms for ε_{xc} reduced ΔE_{xc} from $2\% - 3\%$ to below 0.5% when applied to the slab systems. This refinement process was thus determined to be sufficient.

The refined form for the xc energy density in the three finite LDAs has now been increased from the four-parameter fit in Ref. 106 to a seven-parameter fit[7]:

$$\varepsilon_{xc}(n) = (A + Bn + Cn^2 + Dn^3 + En^4 + Fn^5)n^G, \tag{4.2}$$

where the optimal parameters for each LDA are given in Table 4.1. The functional form of the original four-parameter fit was chosen after exploring a variety of different fits and finding it to most closely match the data. With the increased precision of our calculations, in the refined fit, we have determined seven parameters to be the optimal number after performing some statistical tests, such as the Fisher F-test etc.

---

[7]We have significantly increased the precision of the calculations for the slab systems in order to do this. The numerical difference between the new seven-parameter fits and original four-parameter fits is less than 1% in ε_{xc} across the density range used in constructing the LDAs (except in the very low-density region $n < 0.06$ a.u.). This has allowed us to resolve the differences between the four LDAs in fine detail.

Table 4.1: Optimal fit parameters for $\varepsilon_{xc}(n)$ in the finite LDAs. The last two rows contain the mean absolute error (MAE) and root-mean-square error (RMSE) of the fits, which are approximately one order of magnitude smaller than those of the original four-parameter fits. $\varepsilon_{xc}(n)$ is graphed in Sec. 4.2.4 below.

Parameter	1*e* value	2*e* value	3*e* value
A	-1.2202	-1.0831	-1.1002
B	3.6838	2.7609	2.9750
C	-11.254	-7.1577	-8.1618
D	23.169	12.713	15.169
E	-26.299	-12.755	-15.776
F	12.282	5.3817	6.8494
G	7.4876×10^{-1}	7.0955×10^{-1}	7.0907×10^{-1}
MAE	1.3×10^{-4}	1.2×10^{-4}	9.9×10^{-5}
RMSE	1.9×10^{-3}	5.1×10^{-4}	3.8×10^{-4}

The xc potential v_{xc} is defined as the functional derivative of the xc energy which in the LDA reduces to a simple form[8]:

$$v_{xc}^{\text{LDA}}(n) = \varepsilon_{xc}(n(x)) + n(x)\frac{d\varepsilon_{xc}}{dn}\bigg|_{n(x)}. \tag{4.3}$$

4.2.2 HEG exchange functional

In Ref. 121 we solved the Hartree-Fock equations to find the exact exchange energy density ε_x for a fully spin-polarised ($\zeta = 1$ where $\zeta \equiv (N^\uparrow - N^\downarrow)/N$)[9] 1D HEG of density n consisting of an infinite number of electrons interacting via the softened Coulomb repulsion $u(x - x') = (|x - x'| + 1)^{-1}$:

$$\varepsilon_x(n) = -\frac{1}{8\pi^2 n}\int_{-\pi n}^{\pi n} dk \int_{-\pi n}^{\pi n} dk'\, u(k' - k), \tag{4.4}$$

where the Fourier transform of $u(x - x')$ is integrated over the plane defined by the Fermi wave vector $k_F = \pi n$.

Solving Eq. (4.4) for the range of densities we used in the finite LDAs, we parameterised $\varepsilon_x(n)$. Once again, we have increased our fit from four parameters to seven parameters, as in Eq. (4.2) above[10]. The optimal parameters are given in Table 4.2. The $\varepsilon_x(n)$ curve is shown in the inset of Fig. 4.2

---

[8]See Appendix C.1.1 for the parametric form of the xc potential in the finite LDAs.
[9]Here, $N^\uparrow$ and $N^\downarrow$ are the densities of the spin-up and spin-down electrons, respectively. As we restrict ourselves to spinless electrons (i.e. a single spin type), this corresponds to full spin polarisation.
[10]See Appendix C.1.2 for the parametric form of the exchange potential in the HEG LDA.

Table 4.2: Optimal fit parameters for $\varepsilon_x(n)$ in the HEG LDA. The last two rows contain the mean absolute error (MAE) and root-mean-square error (RMSE) of the fit.

Parameter	Value	Parameter	Value
A	-1.1511	E	-20.896
B	3.3440	F	9.4861
C	-9.7079	G	7.3586×10^{-1}
D	19.088		
MAE	6.5×10^{-5}		
RMSE	7.2×10^{-4}		

4.2.3   HEG correlation functional[11]

We use the lattice regularized diffusion Monte Carlo (LRDMC) algorithm [122] to compute the ground-state energy of the fully spin-polarised HEG over a wide range of densities, much higher than the 0.6 a.u. limit used in the finite LDAs. This is in order to ensure the resultant parameterisation of the correlation energy density ε_c reduces to the known high-density and low-density limits. We determine ε_c by subtracting the kinetic energy and ε_x contributions from the total energy.

To parameterise the correlation energy density we use a fit of the form[12]

$$\varepsilon_c(r_s) = -\frac{A_{\text{RPA}}r_s + Er_s^2}{1 + Br_s + Cr_s^2 + Dr_s^3} \frac{\ln\left(1 + \alpha r_s + \beta r_s^2\right)}{\alpha}, \tag{4.5}$$

where r_s is the Wigner-Seitz radius and is related to the density (in 1D) by $2r_s = 1/n$. The optimal parameters (with estimated errors) are given in Table 4.3. The fit applied to the data is shown in Fig. 4.2.

The high-density limit (infinitely-weak correlation) of the parameterisation is

$$\varepsilon_c(r_s \to 0) = -A_{\text{RPA}}r_s^2, \tag{4.6}$$

and its low-density limit (infinitely-strong correlation) is

$$\varepsilon_c(r_s \to \infty) = -\frac{2E}{\alpha D}\frac{\ln(r_s)}{r_s}. \tag{4.7}$$

Therefore, the parametric form in Eq. (4.5) is appropriate as it correctly reproduces the expected behaviour of the correlation energy density in the high-density limit [123,

---

[11]The calculations in this section were performed by M. Casula.
[12]See Appendix C.1.2 for the parametric form of the correlation potential in the HEG LDA.

Table 4.3: Optimal fit parameters with estimated errors in parentheses for $\varepsilon_c(r_s)$ in the HEG LDA. The last two rows contain the mean absolute error (MAE) and root-mean-square error (RMSE) of the fit. Note: A_{RPA} has been determined from the high-density limit for ε_c (in which the random phase approximation (RPA) is exact [123, 124]), which is exactly fulfilled by our fit, and hence has no associated error.

Parameter	Value	Parameter	Value
A_{RPA}	9.415195×10^{-4}	E	$2.61(3) \times 10^{-6}$
B	$2.601(5) \times 10^{-1}$	α	$1.254(2)$
C	$6.404(7) \times 10^{-2}$	β	$28.8(1)$
D	$2.48(3) \times 10^{-4}$		
MAE	2.4×10^{-5}		
RMSE	1.3×10^{-4}		
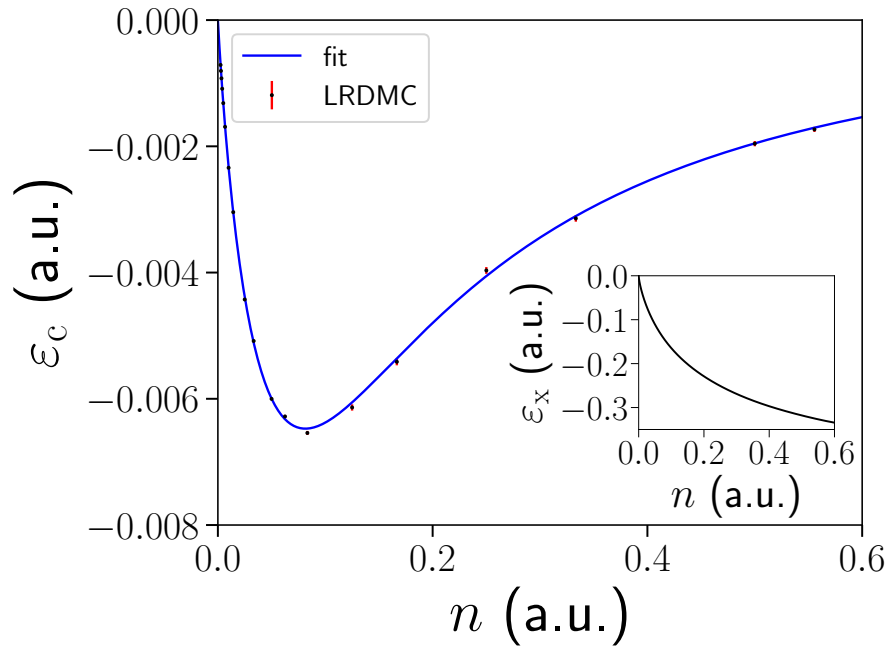
Fig. 4.2. The ε_c (with associated error bars) for a set of HEGs over the density range used in the finite LDAs. The fit applied (solid blue) becomes exact in the known high-density and low-density limits. Inset: The ε_x curve in the HEG LDA.

124] ($\varepsilon_c \propto r_s^2$) and low-density limit ($\varepsilon_c \propto \ln(r_s)/r_s$).

4.2.4 Comparison of 1*e*, 2*e*, 3*e* and HEG LDAs

Summing together the HEG exchange and correlation parametric fits, we can now compare the HEG LDA that we have developed against the three finite LDAs. The striking similarity between the four ε_{xc} curves can be seen in Fig. 4.3(a). While very similar in the low-density range, there are some differences between them. These are highlighted in Fig. 4.3(b) which, using the 1*e* LDA as a reference, plots its difference with the remaining LDAs. There is a competing balance between exchange and correlation. At low densities, these differences can be mainly attributed to ε_c, which is entirely absent in the 1*e* LDA, and increases in magnitude as we progress to 2*e* to 3*e* to HEG [Fig. 4.4]. As we move to higher densities in which the magnitude of ε_c decreases, and the magnitude of ε_x increases, the order of the four ε_{xc} curves reverses. They increasingly separate as we move to higher densities with the 1*e* LDA, which consists entirely of self-interaction correction, giving the largest magnitude for ε_{xc}. By plotting the difference between the 1*e* LDA (where correlation is absent) and the exchange part of the HEG LDA (i.e. removing the correlation term), it can be seen that the 1*e* LDA yields a larger exchange energy density than the HEG LDA at all densities [Fig. 4.5].

The refinement process used in the construction of the finite LDAs focused on giving the correct E_{xc} in the limit of the slab systems, but did not ensure that the correct v_{xc}, and by extension electron density, were reproduced (a property of HEG LDAs). Hence, it is of interest to examine the *self-consistent* application of our LDAs to the slabs. By doing so we find that the finite LDAs are completely inadequate at reproducing the densities of the slab systems. In order to understand this we analyse the *exact* v_{xc} for a variety of the slab systems (i.e. we reverse-engineer the exact *n*). We compare the exact v_{xc} against the exact *n* and find that there is a high non-local dependence on *n* (see Fig. 4.6 for an example). This implies that *no* local density functional can accurately reproduce v_{xc} and hence *n* for the slab systems. In light of this, the success of the finite LDAs reported below is all the more surprising.
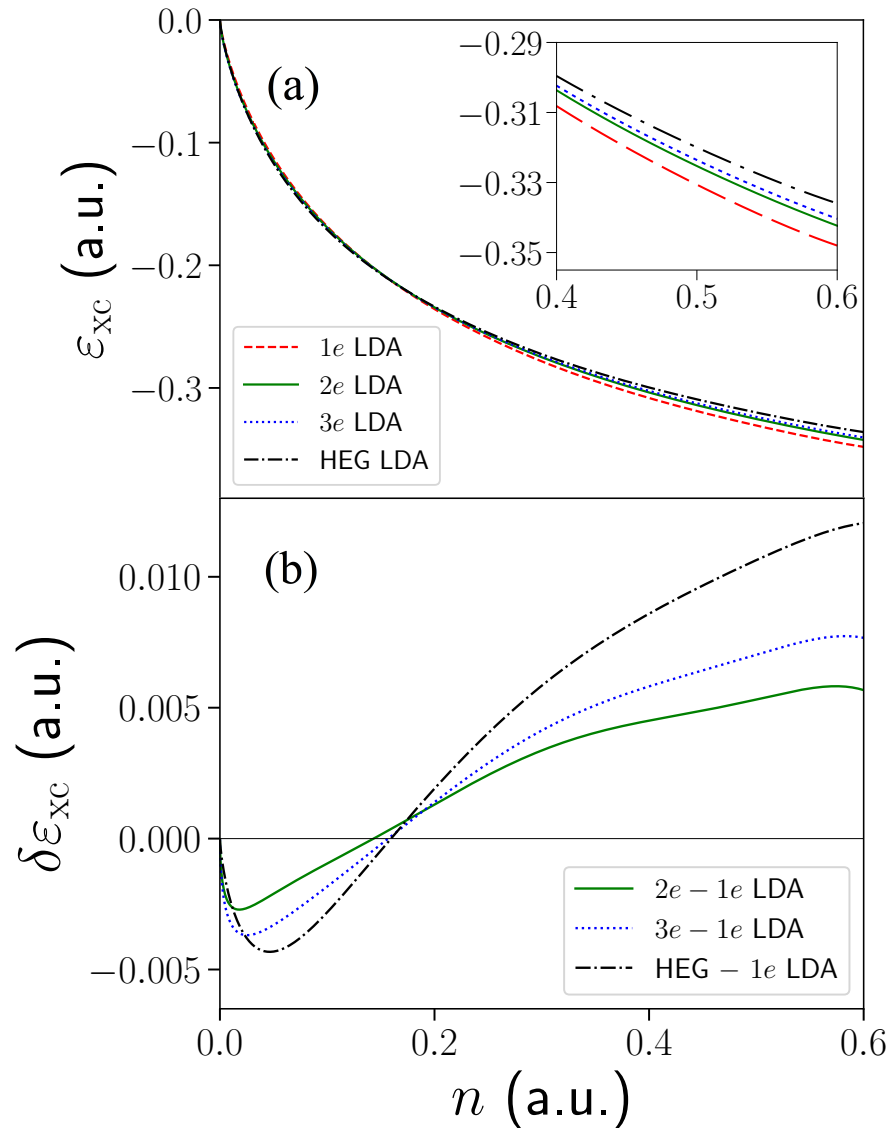
Fig. 4.3. (a) The ε_{xc} curves in the $1e$ (dashed red), $2e$ (solid green), $3e$ (dotted blue) and HEG (dotted-dashed black) LDAs. Inset: Close-up of the four curves at higher densities. The similarity between them is striking, with a clear progression from $1e$ to $2e$ to $3e$ to HEG. (b) The $1e$ LDA is used as a reference here. Plotted is its difference ($\delta\varepsilon_{xc} = \varepsilon_{xc} - \varepsilon_{xc}^{1e}$) with the $2e$ (solid green), $3e$ (dotted blue) and HEG (dotted-dashed black) LDAs.
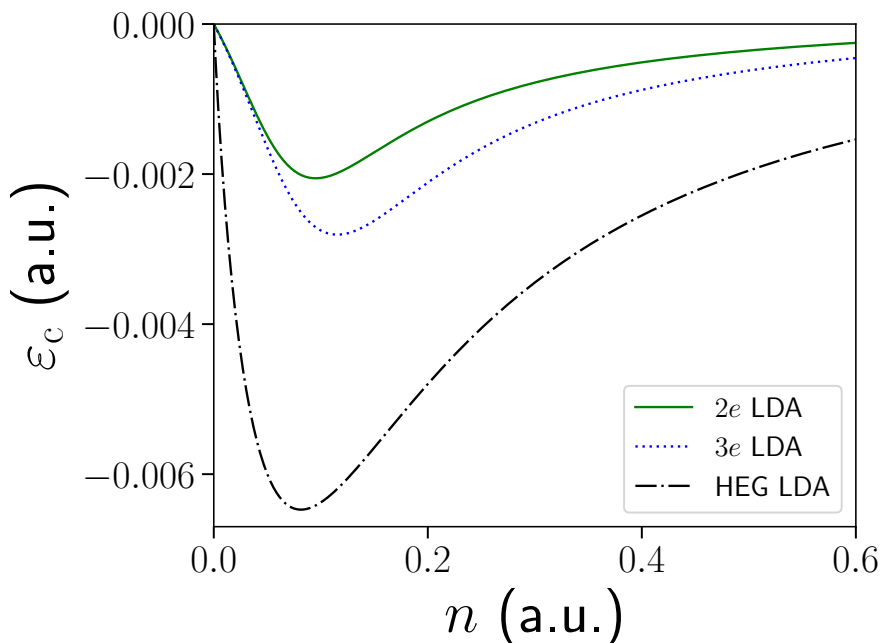
Fig. 4.4. We calculate the exact ε_c for the 2*e* (solid green line) and 3*e* (dotted blue line) slab systems through Hartree-Fock calculations. We plot these against the ε_c curve in the HEG LDA (dotted-dashed black line). The ε_c in the HEG LDA is much larger ($\sim$2–3 that of the 3*e* LDA and $\sim$3–4 that of the 2*e* LDA). While not a perfect comparison due to the refinement process used in the construction of the finite LDAs, it gives a useful indication of the size of ε_c in their ε_{xc} curves.
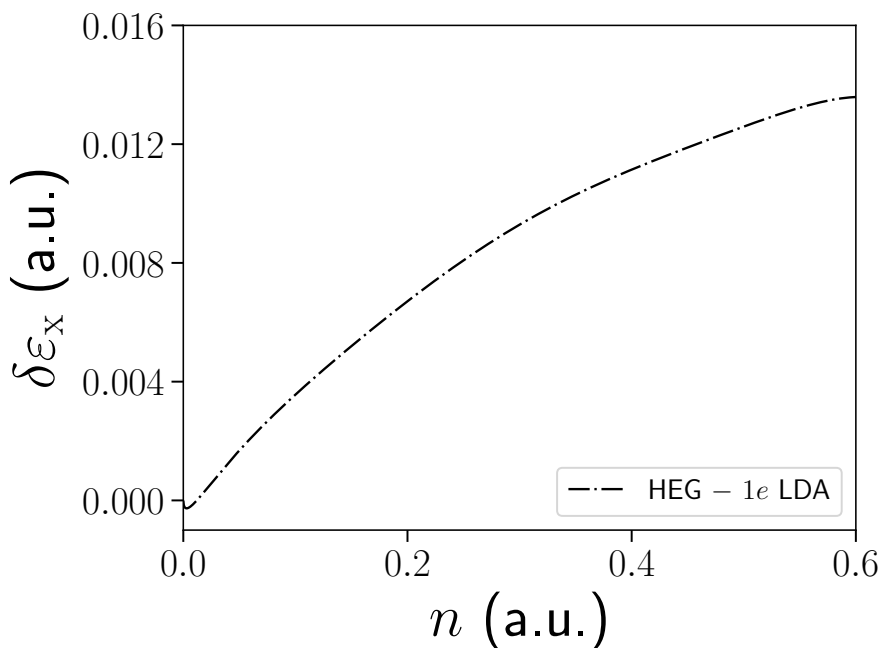
Fig. 4.5. The ε_x curve in the 1*e* LDA ($\varepsilon_x = \varepsilon_{xc}$) is used as a reference here. Plotted is its difference ($\delta\varepsilon_x = \varepsilon_x - \varepsilon_x^{1e}$) with the ε_x curve in the HEG LDA ($\varepsilon_x = \varepsilon_{xc} - \varepsilon_c$). It can be seen that the 1*e* LDA yields a larger exchange energy density than the HEG LDA at all densities. Note: This is not true in the very low-density region ($n < 0.012$), which we attribute to errors in the fits.
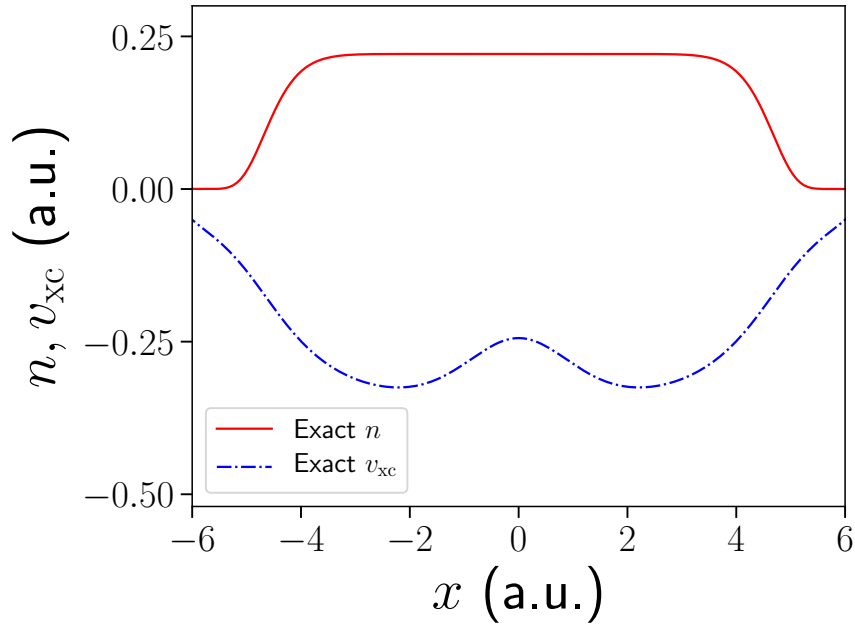
Fig. 4.6. The exact electron density (solid red line) and xc potential (dotted-dashed blue line) for a typical two-electron slab system with a locally homogeneous density of ≈ 0.22 a.u. across the plateau region. There is a high non-local dependence of v_{xc} on n, which implies that *no* local density functional can accurately reproduce v_{xc} and hence n for the slab systems.

4.3 Testing the LDAs

In the previous section we observed the close similarity between the four LDAs. In this section we apply them to a range of model systems[13] in order to identify the differences between them.

4.3.1 Weakly correlated systems

System 1 (2e harmonic well). We first consider a pair of interacting electrons in a strongly confining harmonic potential well ($\omega = \frac{2}{3}$ a.u.) where correlation is very weak[14]. We calculate the exact many-body electron density using iDEA, and compare it against the densities obtained from applying the LDAs self-consistently. There is a progression from the 1*e*–2*e*–3*e*–HEG LDA and so we choose to plot the 1*e* and HEG LDA densities (i.e. the 2*e* and 3*e* LDA densities lie between these) against the exact [Fig. 4.7(a)].

---

[13]See Appendix C.1 for the parameters of the model systems, and details on our calculations to obtain converged results.

[14]We calculate the absolute error between the exact electron density and the density obtained from a self-consistent Hartree-Fock calculation ($\delta n = n^{\mathrm{HF}} - n^{\mathrm{exact}}$), and find the net absolute error to be $\int |\delta n|\, dx \approx 1.4 \times 10^{-3}$. The correlation energy is 0.13% of the exchange-correlation energy, -0.62 a.u.

Table 4.4: Total energies and xc energies for the set of weakly correlated systems (1–3), from exact calculations and from applying the four LDAs self-consistently ($\delta E^{\text{LDA}} = E^{\text{LDA}} - E^{\text{exact}}$). Estimated errors are ± 1 in the last decimal place, unless otherwise stated in parentheses.

System	E_{total} (a.u.)				
	Exact	$\delta E^{1e}_{\text{total}}$	$\delta E^{2e}_{\text{total}}$	$\delta E^{3e}_{\text{total}}$	$\delta E^{\text{HEG}}_{\text{total}}$
2e harmonic well	1.6932	0.0037	0.0126	0.0153	0.0211
3e harmonic well	3.1875	-0.0073	0.0065	0.0108	0.0199
2e double well	-1.0301	0.0237	0.0286	0.0296	0.0323
System	E_{xc} (a.u.)				
	Exact	$\delta E^{1e}_{\text{xc}}$	$\delta E^{2e}_{\text{xc}}$	$\delta E^{3e}_{\text{xc}}$	$\delta E^{\text{HEG}}_{\text{xc}}$
2e harmonic well	-0.6192	0.0045	0.0137	0.0165	0.0225
3e harmonic well	-0.9305(5)	-0.0058(5)	0.0085(5)	0.0129(5)	0.0223(5)
2e double well	-0.5349	0.0256	0.0317	0.0331	0.0363

Both LDAs match the exact density well, and so we plot their absolute errors ($\delta n = n^{\text{LDA}} - n^{\text{exact}}$) to more clearly identify their differences [Fig. 4.7(b)]. The $1e$ LDA has a slightly smaller net absolute error ($\int |\delta n| \, dx$). While the HEG LDA gives a slightly better electron density in the central region (dip in the density), the $1e$ LDA better matches the decay of the density towards the edges of the system, and perhaps more interestingly, the two peaks in the density where the self-interaction correction is largest.

Due to the importance of energies in DFT calculations, we also compare the exact E_{xc} and total energy E_{total}, with those obtained from applying the LDAs self-consistently [Table 4.4]. While all the LDAs give good approximations to both quantities, there are some significant differences due to this system being dominated by regions of high density, and the ε_{xc} curves separating in this limit (see Fig. 4.3). As with the approximations to the electron density, there is a progression from the $1e$–$2e$–$3e$–HEG LDA, with the $1e$ LDA reducing the absolute errors ($\delta E = E^{\text{LDA}} - E^{\text{exact}}$) in the HEG LDA by a factor of $5 - 6$.

System 2 (3e harmonic well). Next, we consider a harmonic potential well with three electrons, but slightly less confining ($\omega = \frac{1}{2}$), in order to avoid an unphysically high electron density ($n > 0.6$ a.u.). As in the $2e$ harmonic well system, we find a progression from the $1e$–$2e$–$3e$–HEG LDA, with all LDAs giving good electron densities (see Fig. 4.8(a) for the $1e$ and HEG LDA densities plotted against the exact). Again, the $1e$ LDA has the smallest net absolute error, and outperforms the rest of the LDAs in the regions where the density peaks [Fig. 4.8(b)].
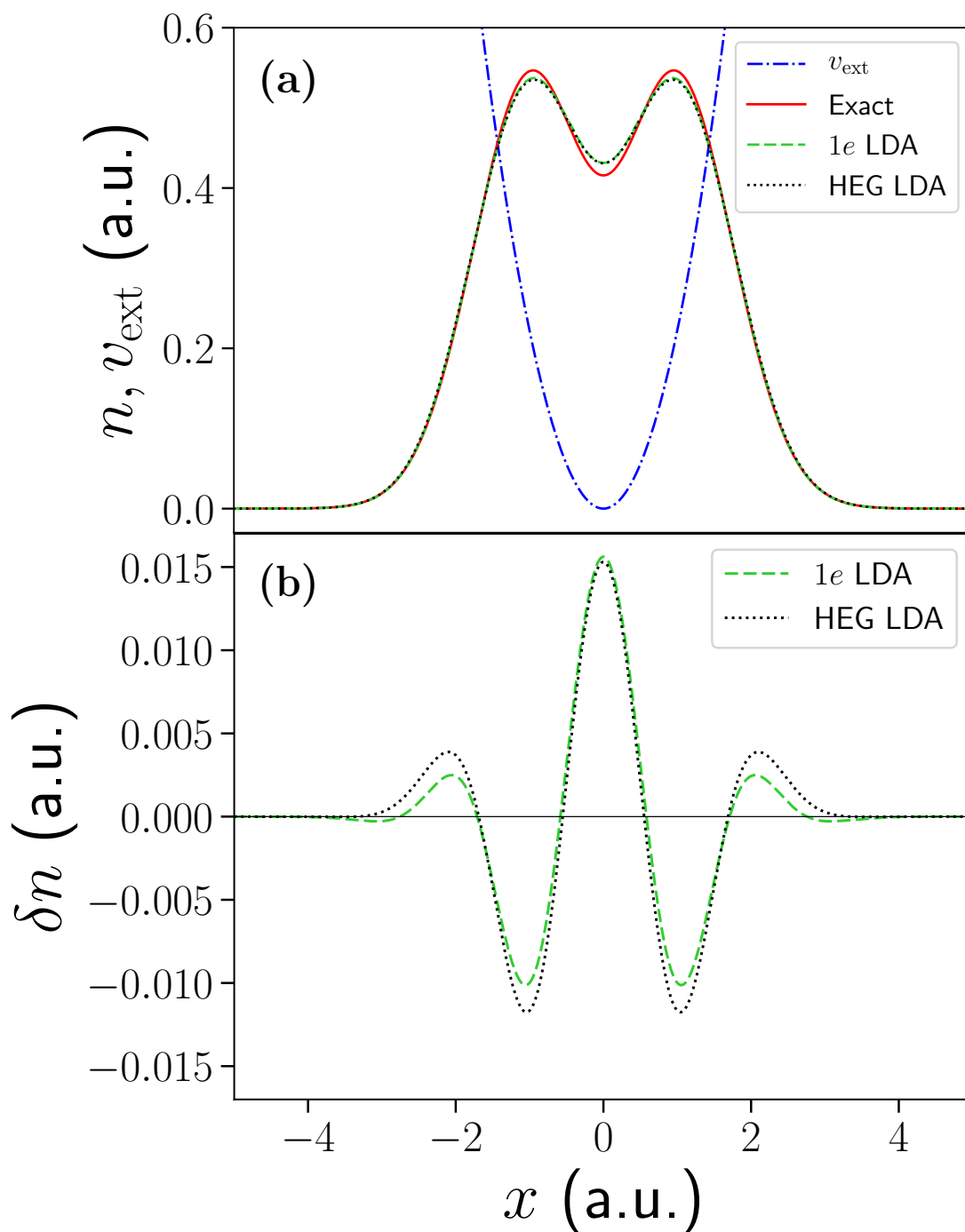
Fig. 4.7. System 1 (two electrons in a harmonic potential well). (a) The external potential (dotted-dashed blue line), together with the exact electron density (solid red line), and the densities obtained from applying the 1e (dashed green line) and HEG (dotted black line) LDAs. Both LDAs are in very good agreement with the exact result. (b) The absolute error in the density ($\delta n = n^{\text{LDA}} - n^{\text{exact}}$) in the 1$e$ (dashed green line) and HEG (dotted black line) LDAs, allowing their differences to be more clearly identified.
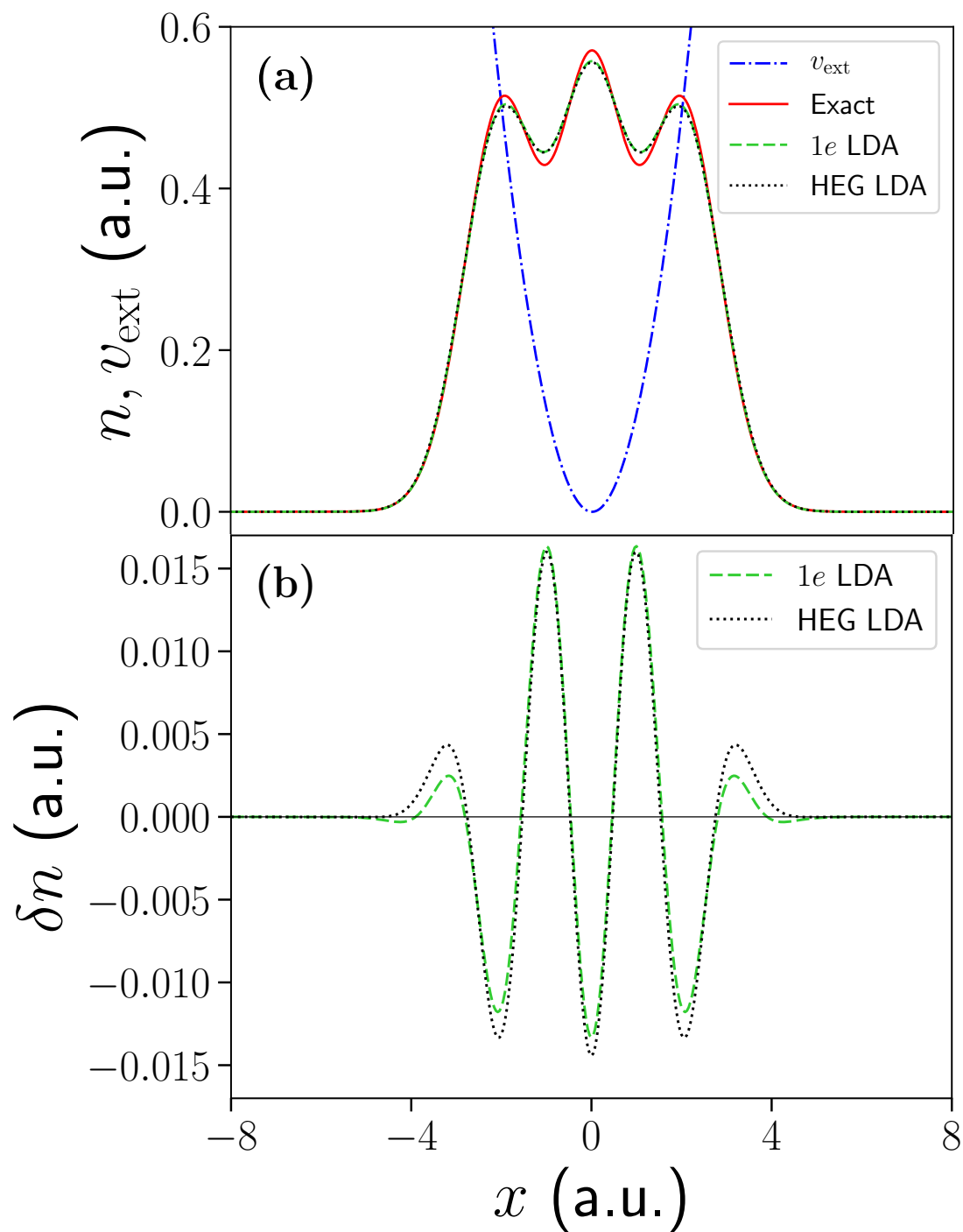
Fig. 4.8. System 2 (three electrons in a harmonic potential well). (a) The external potential (dotted-dashed blue line), together with the exact electron density (solid red line), and the densities obtained from applying the 1*e* (dashed green line) and HEG (dotted black line) LDAs. Much like the 2*e* harmonic well system, both LDAs match the exact density well. (b) The absolute error in the density in the 1*e* (dashed green line) and HEG (dotted black line) LDAs. Again, the 1*e* LDA outperforms the HEG LDA in the density peaks, which is dominated by the self-interaction correction.

We also compare the exact E_{xc} and E_{total} against the LDAs [Table 4.4]. All LDAs give good energies, with some noticeable differences between them due to this system being dominated by regions of high density, like in the 2*e* harmonic well system. However, the *magnitude* of E_{xc} in the 1*e* LDA is greater than the exact (i.e. it overestimates the amount of exchange + correlation), and subsequently it gives a total energy lower than the exact. While the absolute error in E_{xc} for each LDA is similar to that in E_{total}, this overestimation of exchange + correlation in the 1*e* LDA results in the 2*e* LDA giving the best total energy.

4.3.2 A system dominated by the self-interaction correction

The one-electron orbitals of the HEG are plane waves extended over the entire (infinite) system and are therefore free of self-interaction. Hence, the self-interaction correction (SIC) is *absent* in xc functionals constructed from the HEG. However, the xc energy of the 1*e* slab systems (which were used to construct the 1*e* LDA) consists entirely of SIC. In the first two model systems, we found that the 1*e* LDA (and the other finite LDAs) better describes the electron density in regions where the SIC is strongest, than the HEG LDA. We now investigate this further.

System 3 (2e double well). We choose a system with two electrons confined to a double-well potential. The wells are separated, such that the electrons are *highly localised* and can be considered as two separate subsystems [Fig. 4.9(a)]. This results in the Hartree potential being small outside of the wells, and being dominated by the electron self-interaction within the wells. Consequently, a large proportion of the xc potential is self-interaction correction. Applying the LDAs, we find the usual progression 1*e*–2*e*–3*e*–HEG. Focusing on the peaks in the electron density, the 1*e* LDA substantially reduces the error present in the HEG LDA [Fig. 4.9(b)]. To understand this, we analyse the xc potential [Fig. 4.9(c)]. The 1*e* LDA better reproduces the large dips in v_{xc}, corresponding to the peaks in the electron density. Hence, the SIC is more effectively captured. While the LDA errors in E_{xc} are larger than in the first two systems, they are still small (4.8–6.8%) [Table 4.4]. The absolute errors in E_{total} are similar.

Fig. 4.9. System 3 (two electrons in a double-well potential). (a) The external potential (dotted-dashed blue line), together with the exact electron density (solid red line), and the densities obtained from applying the 1e (dashed green line) and HEG (dotted black line) LDAs. The wells are separated, such that the electrons are highly localised. (b) The absolute error in the density in the 1e (dashed green line) and HEG (dotted black line) LDAs. The 1e LDA is far superior in the regions where the density peaks, and hence where the Hartree potential is large and dominated by the electron self-interaction. (c) The exact xc potential (solid red line), and the xc potentials given by the 1e (dashed green line) and HEG (dotted black line) LDAs. The dips in v_{xc} are more closely matched by the 1e LDA due to it better capturing the self-interaction correction, present in the exact v_{xc}.

Table 4.5: Total energies and xc energies for the set of strongly correlated systems (4–5), from exact calculations and from applying the four LDAs self-consistently ($\delta E^{\text{LDA}} = E^{\text{LDA}} - E^{\text{exact}}$). Estimated errors are ± 1 in the last decimal place, unless otherwise stated in parentheses.

System	E_{total} (a.u.)				
	Exact	$\delta E^{1e}_{\text{total}}$	$\delta E^{2e}_{\text{total}}$	$\delta E^{3e}_{\text{total}}$	$\delta E^{\text{HEG}}_{\text{total}}$
2e atom	-1.5099	0.0053	0.0044	0.0032	0.0022
3e atom	-2.3282(5)	0.0121(5)	0.0085(5)	0.0057(5)	0.0029(5)
System	E_{xc} (a.u.)				
	Exact	$\delta E^{1e}_{\text{xc}}$	$\delta E^{2e}_{\text{xc}}$	$\delta E^{3e}_{\text{xc}}$	$\delta E^{\text{HEG}}_{\text{xc}}$
2e atom	-0.3728	0.0084	0.0101	0.0099	0.0111
3e atom	-0.493(4)	0.029(4)	0.029(4)	0.027(4)	0.028(4)

4.3.3 Systems where correlation is stronger

System 4 (2e atom). We now consider a system where the relative size of electron correlation increases significantly[15]: two electrons confined to a *softened* atomic-like potential, $v_{\text{ext}} = -a/(|x| + a)$, where $a = 20$. Although we find the same progression (1*e*–2*e*–3*e*–HEG) as seen in the first three model systems, in which correlation was weak, all LDAs give inadequate electron densities. This can be seen by plotting the 1*e* and HEG LDA densities against the exact [Fig. 4.10(a)]. The LDAs give densities that are not even qualitatively correct, e.g. predicting a single peak in the centre of the system, which is absent in the exact density. The net absolute errors are much larger than in the weakly correlated systems, however, the 1*e* LDA once again gives the smallest [Fig. 4.10(b)]. We find that although the LDA densities are poor, the xc energies are surprisingly good [Table 4.5]. This can be attributed *somewhat* (see Sec. 4.3.4 for investigation of further causes) to errors in the density being partially cancelled by errors inherent in the approximate xc energy functional [125]. We infer this by noting the progression (HEG–3*e*–2*e*–1*e*) when we apply the LDAs to the *exact* density, in contrast to the self-consistent solutions in Table 4.5. As in the weakly correlated systems, the absolute errors in E_{total} are smaller than in E_{xc}, due to a partial cancellation of errors from the Hartree energy component. It is much more apparent in this system due to the LDAs incorrectly predicting a central peak in the electron density [Fig. 4.10(a)].

System 5 (3e atom). Finally, we consider three electrons in an external potential of

---

[15]We calculate the absolute error between the exact electron density and the density obtained from a self-consistent Hartree-Fock calculation ($\delta n = n^{\text{HF}} - n^{\text{exact}}$), and find the net absolute error to be $\int |\delta n|\, dx \approx 7.4 \times 10^{-2}$. The correlation energy is 1.1% of the exchange-correlation energy, -0.37 a.u.
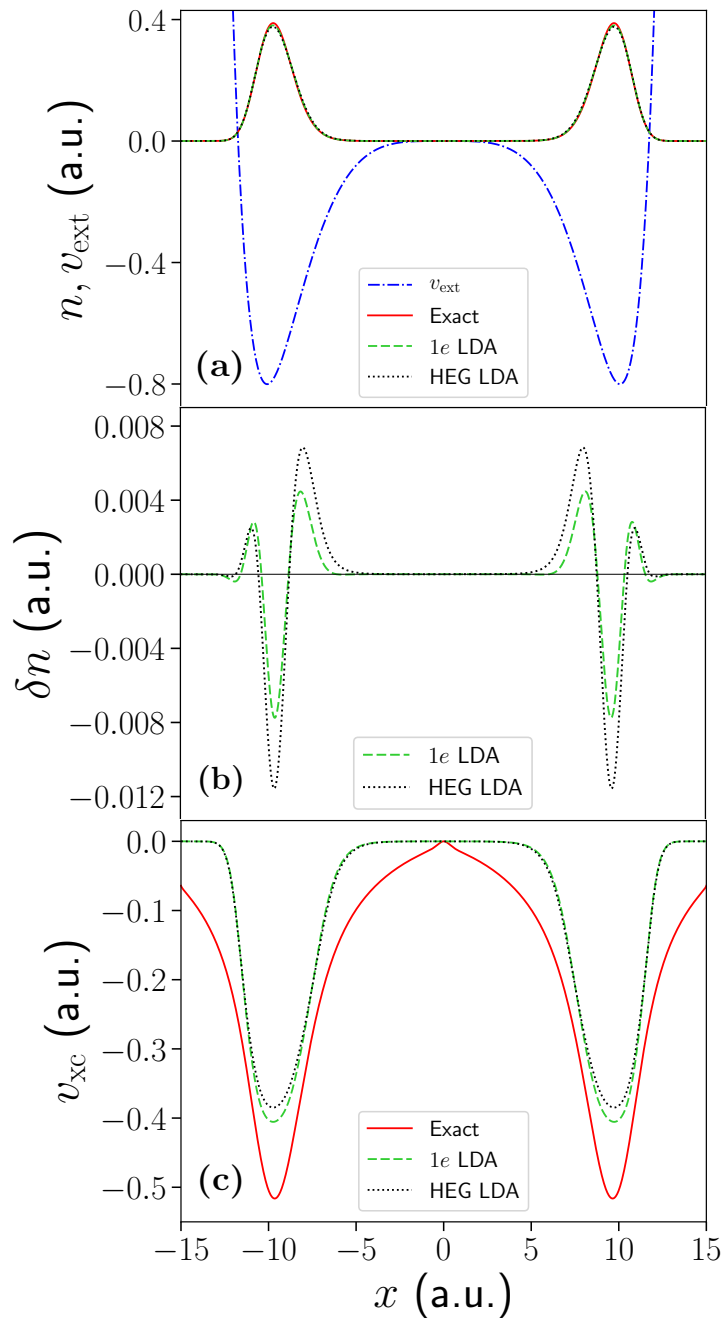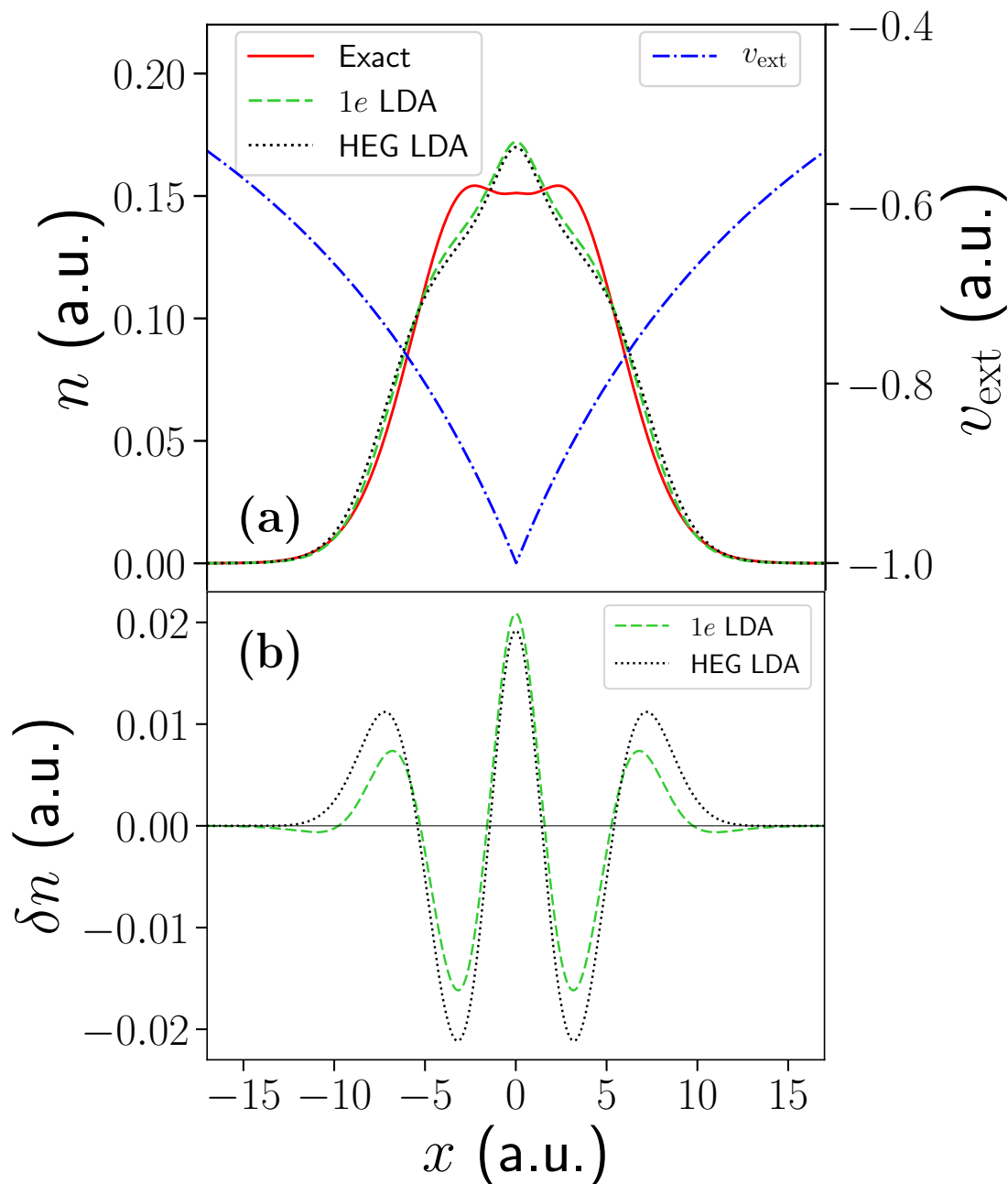
Fig. 4.10. System 4 (two electrons in a softened atomic-like potential). (a) The external potential (dotted-dashed blue line), together with the exact electron density (solid red line), and the densities obtained from applying the 1e (dashed green line) and HEG (dotted black line) LDAs. Unlike in the weakly correlated systems, the LDAs give poor electron densities. (b) The absolute error in the density in the 1e (dashed green line) and HEG (dotted black line) LDAs. While the net absolute errors are much larger than in the weakly correlated systems, the 1e LDA still performs the best.

the same form as the 2*e* atom, but less confining, with $a = 50$. Along with the usual progression (1*e*–2*e*–3*e*–HEG), we find a similar result to the 2*e* atom, with the LDAs giving poor electron densities [Fig. 4.11(a)]. Although the densities are qualitatively correct, unlike in the 2*e* atom, the LDAs significantly underestimate the peaks in the electron density. Subsequently, the absolute errors are very large [Fig. 4.11(b)]. The 1*e* LDA, along with giving the lowest net absolute error, most accurately reproduces the peaks in the density, where the SIC is largest. While the absolute errors in E_{xc} are larger than in the 2*e* atom, they are still small [Table 4.5]. Again, this partially arises from applying approximate xc energy functionals to incorrect densities. As in the 2*e* atom, the absolute errors in E_{total} are much lower than those in E_{xc}, due to a partial cancellation of errors from the Hartree energy component.

4.3.4 Cancellation of errors between exchange and correlation

HEG-based LDAs have been known to typically underestimate the *magnitude* of the exchange energy E_x, while overestimating the magnitude of the correlation energy E_c [38, 39]. This stems from the fact that the HEG is a real, physical system and HEG-based LDAs thereby satisfy a variety of exact sum rules [21]. Consequently, while the total E_{xc} is underestimated in magnitude, the approximation proves to be better than was originally expected due to a partial cancellation of errors.

We investigate how well our HEG LDA approximates E_x and E_c in the model systems, and how this contributes to accurate values for E_{xc}. To do this we perform Hartree-Fock calculations for each of the model systems, and together with the exact solutions obtained through iDEA, are able to divide the exact E_{xc} into its exchange and correlation components. We then apply the HEG LDA, which is split into separate E_x and E_c functionals, for comparison [Table 4.6]. In all systems, the HEG LDA underestimates the magnitude of E_x, while it overestimates the magnitude of E_c. However, due to the exchange energy being the dominant component of E_{xc}, even in strongly correlated systems, this only leads to a partial cancellation of errors.

The 1*e* LDA yields a larger magnitude for ε_x than the HEG LDA across the entire density range studied (up to 0.6 a.u.) [Fig. 4.5], which arises from a better description of the SIC [Sec. 4.3.2]. In the 1*e* LDA correlation is absent. Consequently, the 1*e* xc energies that follow from Tables 4.4 and 4.5 can be considered as approximations to E_x. We note that the 1*e* LDA substantially reduces the error in E_x that arises in the
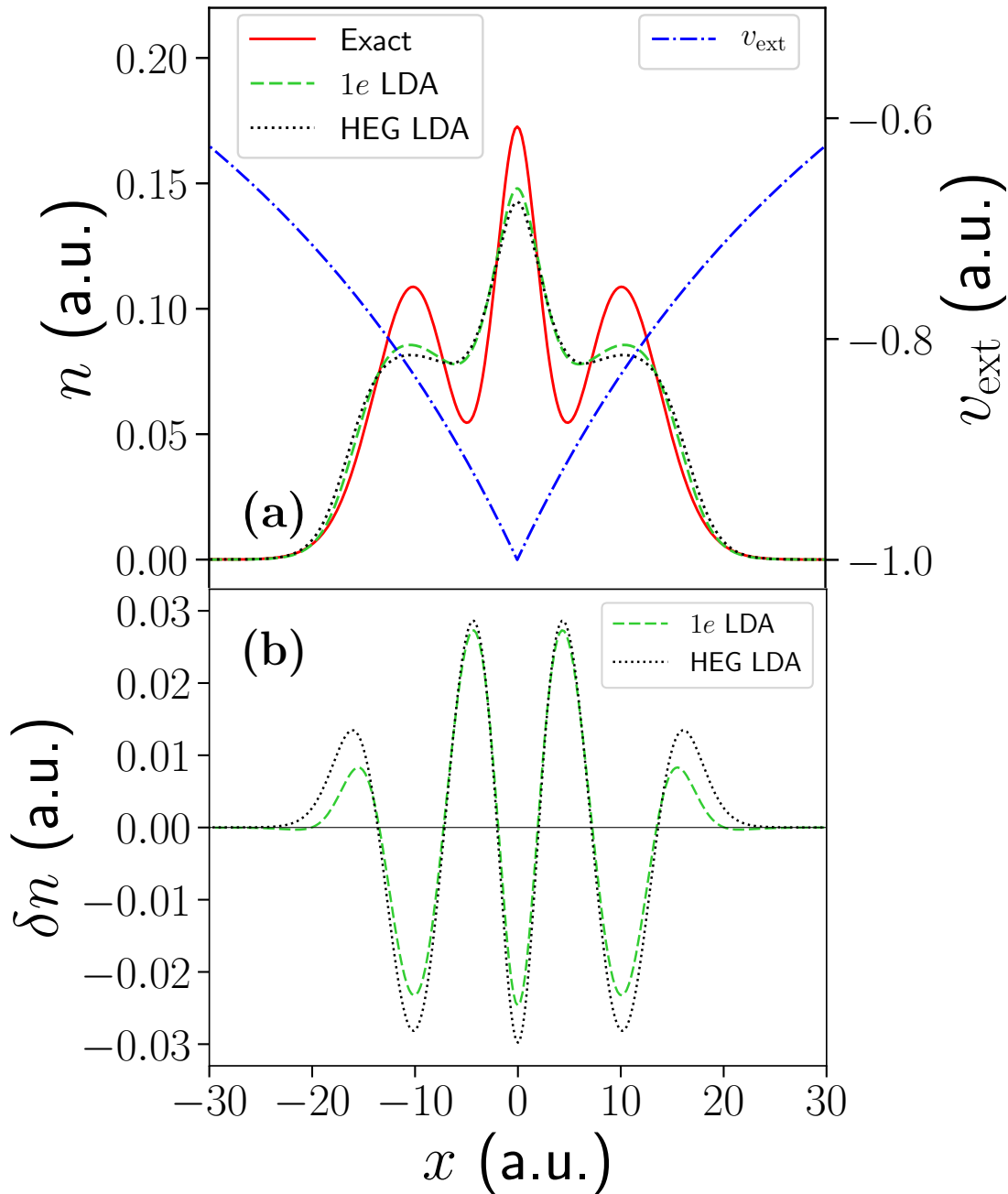
Fig. 4.11. System 5 (three electrons in a softened atomic-like potential). (a) The external potential (dotted-dashed blue line), together with the exact electron density (solid red line), and the densities obtained from applying the 1*e* (dashed green line) and HEG (dotted black line) LDAs. Like in the 2*e* atom, the LDAs give poor electron densities. The 1*e* LDA more accurately reproduces the peaks in the density, where the SIC is largest. (b) The absolute error in the density in the 1*e* (dashed green line) and HEG (dotted black line) LDAs. Again, the net absolute errors are large, with the 1*e* LDA giving the smallest.

Table 4.6: Exchange energies and correlation energies for all systems (1-5), from exact calculations and from applying the HEG LDA self-consistently ($\delta E^{\mathrm{LDA}} = E^{\mathrm{LDA}} - E^{\mathrm{exact}}$). Estimated errors are ± 1 in the last decimal place, unless otherwise stated in parentheses.

System	E_{x} (a.u.)	
	Exact	$\delta E_{\mathrm{xc}}^{\mathrm{HEG}}$
2e harmonic well	-0.6184	0.0268
3e harmonic well	-0.9286(5)	0.0276(5)
2e double well	-0.5349	0.0441
2e atom	-0.3686	0.0185
3e atom	-0.488(3)	0.041(3)
System	E_{c} (a.u.)	
	Exact	$\delta E_{\mathrm{xc}}^{\mathrm{HEG}}$
2e harmonic well	-0.0008	-0.0043
3e harmonic well	-0.0019	-0.0053
2e double well	-0.0000	-0.0077
2e atom	-0.0042	-0.0074
3e atom	-0.0043(5)	-0.0142(5)

HEG LDA[16]. We infer that this error reduction will also extend to the 2*e* and 3*e* LDAs.

4.4 Conclusions

We have constructed an LDA based on the homogeneous electron gas (HEG) through suitable quantum Monte Carlo techniques and find that it is remarkably similar in many regards to a set of three LDAs constructed from finite systems. Applying them to test systems to explore the differences between them, we find that the finite LDAs give better densities and energies in highly confined systems in which correlation is weak. Most interestingly, the LDA constructed from systems of just one electron most accurately describes the self-interaction correction. All LDAs give poor densities in systems where correlation is stronger, but give reasonably good energies, with the HEG LDA giving the best total energies. Across all test systems, the HEG LDA underestimates the magnitude of the exchange energy and overestimates the magnitude of the correlation energy, leading to a partial cancellation of errors. As a consequence of the finite LDAs giving a better description of the self-interaction correction, we infer that they would reduce the error in the exchange energy. Furthermore, we expect

---

[16]This is also true in the 2*e* double-well system where correlation is negligible, and the exchange energy is dominated by the SIC.

---

that finite LDA functionals will also provide a better treatment of the SIC for spin-ful electrons. Their derivation and usage could lead to an improved description of the electronic structure in many situations, such as at the onset of Wigner oscillations which manifest in the density and are a sign of incipient Wigner localisation driven by the interaction between electrons [126, 127].

As discussed extensively in Sec. 2.6, local approximations are widely used in many applications of DFT and, through adiabatic application, TDDFT. Even in non-adiabatic applications, the ground-state functional used in a TDDFT calculation is crucial to its predictive power, e.g. when solving the Dyson equation to compute the density-response function χ. In this chapter, we have identified the relative strengths and weaknesses of constructing ground-state local approximations from finite systems rather than the HEG. This insight could lead to better accuracy in a variety of applications, and through extension to the time-dependent regime, the development of improved non-adiabatic functionals from finite systems.

EXACT NON-ADIABATIC PART OF THE KOHN-SHAM POTENTIAL AND ITS FLUIDIC APPROXIMATION[1]

As discussed in Chapter 2, the validity of time-dependent DFT (TDDFT) in practical applications is often restricted by the limitations of available approximate functionals for electron exchange and correlation. Typically, an adiabatic approximation based on ground-state DFT is used for this part of the time-dependent Kohn-Sham potential, thereby neglecting all memory effects. In this chapter, we consider the purest application of the concept of the adiabatic functional to the *complete* KS potential, and present a simple geometrical "fluidic" approximation to the non-adiabatic part. For a variety of model systems, we calculate the exact time-dependent electron density, and find that the fluidic approximation corrects a large part of the error arising from the "exact adiabatic" approach, even when the system is evolving far from adiabatically.

---

[1]This chapter represents work that has been published: M. T. Entwistle and R. W. Godby, 'Exact nonadiabatic part of the Kohn-Sham potential and its fluidic approximation', *Phys. Rev. Materials 4, 035002 (2020)*. The sections of this chapter have been adapted from the publication.

5.1 Introduction

As discussed in Sec. 2.4.3, the true time-dependent xc potential is a functional of the density at the present and all previous times $v_{xc}[n]$. However, most approximate functionals utilise an adiabatic approach, in which the instantaneous electron density is implicitly assumed to be in its ground state, thereby neglecting all memory effects [30, 31] (see Sec. 2.4.3.2):

$$v_{xc}[n](x,t) = v_{xc}^0[n_0](x,t)|_{n_0(x) \to n(x,t)}. \tag{5.1}$$

While these ground-state approximations have steadily improved [2, 3, 44, 46, 128–135] (moving up Jacob's ladder [36]; see Sec. 2.6.1), by definition they cannot approach the exact TDDFT potential: it is necessary to address the non-adiabatic contributions in order for TDDFT to be capable of predictive accuracy in relation to a multitude of applications to diverse fields such as the determination of electronic excitation energies including those of a charge-transfer nature [12], electron dynamics [13] including non-perturbative charge-transfer dynamics [14], time-resolved spectroscopy [15] and electron scattering [16].

It has been argued [26, 27, 136, 137] that the exact non-adiabatic functional often requires strong non-local temporal and spatial dependence on the density. A number of properties of the exact functional (see Sec. 2.4.3.1), such as the harmonic potential theorem (HPT) [27] and zero-force theorem (ZFT) [26], have been used to identify limitations of previous approximate TDDFT functionals. Adiabatic functionals trivially satisfy many of these exact conditions through their complete lack of memory-dependence, yet prove inadequate in many applications [8, 12–16, 31, 53, 66, 67, 138–143] (see Sec. 2.6.2). The development of non-adiabatic functionals that continue to satisfy these exact properties is non-trivial. For example, it was shown that modifying the adiabatic local density approximation (ALDA) by introducing time-nonlocality, such as in the Gross-Kohn [144] (GK) approximation, is inappropriate [26, 27].

The best-known approximate non-adiabatic functional is that developed by Vignale and Kohn [137, 145, 146] (VK). This was constructed by studying the responses to slowly-varying perturbations of the homogeneous electron gas, and they found a time-dependent xc vector potential as a functional of the local current and charge densities j and n, thereby implicitly obtaining a scalar potential which depends non-locally on the density. While the VK formalism has proved promising [147–157], not

least through it obeying the HPT and ZFT, its validity is limited [158–162] owing to the constraints under which it was derived.

5.1.1 Decomposition of the Kohn-Sham potential

As discussed above, most approximate TDDFT functionals are adiabatic, which is typically understood to mean combining a ground-state xc potential v_{xc}^0, with the time-dependent external and Hartree potentials. While the Hartree potential is purely adiabatic, as it depends solely on the instantaneous density, the external potential will, in general, contain a component which induces a non-adiabatic response in the density[2]. Strictly speaking, there is some level of inconsistency in this approach, with mixing and matching of adiabatic and non-adiabatic components.

In this chapter, in order to clearly distinguish between adiabatic and non-adiabatic contributions, we consider the purest application of the concept of the adiabatic functional to the *complete* KS potential, $v_s[n]$: at each instant, the DFT KS potential v_s^A, whose *ground-state* density is equal to the exact time-dependent density. The remainder of the exact v_s constitutes the unambiguously non-adiabatic part Δv_s, to which we also propose an approximation. The two components are defined as

$$v_s^A[n](x,t) = v_s^0[n_0](x,t)\big|_{n_0(x)\to n(x,t)}, \tag{5.2a}$$

$$\Delta v_s[n](x,t) = v_s[n](x,t) - v_s^A[n](x,t), \tag{5.2b}$$

where v_s^0 is the exact ground-state KS potential.

5.2 Fluidic approximation

In developing an approximation to Δv_s, it is helpful to consider the situation in different inertial frames, related through a Galilean transformation, as noted by Tokatly *et al.* [140, 163–166]. While v_s^A requires zero correction in any inertial frame when the density is fully static in one of these frames (a consequence of generalised translational invariance; Eq. (2.29)), in the more general case the non-adiabatic corrections to v_s^A may be expected to be at their smallest in the local, instantaneous rest frame of the density, defined by a transformation velocity of the local velocity field $u(x,t) = j(x,t)/n(x,t)$. In particular, the effects of acceleration ($\dot{u} \neq 0$) and dispersion ($\partial_x u \neq 0$) have least

---

[2]A switch-on process is a good example, whereby a perturbing field is suddenly applied to the system in question. While there is a "jump" in the external potential v_{ext}, the density n will not respond in kind.

Chapter 5 Exact non-adiabatic part of the Kohn-Sham potential and its fluidic approximation

effect in a frame where u itself is zero[3]. Conveniently, introducing a vector potential $A = -u(x, t)$ in the original frame of reference is (apart from an unimportant temporal phase factor) equivalent to a Galilean transformation to the local instantaneous rest frame[4] [163, 164]. As described above, the non-adiabatic correction should be minimal in the latter frame, and here we adopt the simple assumption that it is zero. We term this the *fluidic* approximation. The resulting non-adiabatic correction in the original frame is therefore

$$\Delta v_s(x, t > 0) = -\int_{-\infty}^{x} \frac{\partial}{\partial t} u(x', t > 0) \, dx', \tag{5.3}$$

where we have gauge-transformed A into a scalar potential. It is evident that the density-dependence of this Δv_s is non-local in both space and time [137]. For a more in-depth explanation of the above justification, see Appendix D.

5.3   Calculations

Our calculations[5] employ the iDEA code to solve the many-electron Schrödinger equation to determine the exact $n(x, t)$. We then determine the exact $v_s(x, t)$ through time-dependent reverse-engineering (see Sec. 3.1.3.2). We also obtain the exact $v_s^{\mathrm{A}}(x, t)$ by applying *ground-state* reverse-engineering (see Sec. 3.1.3.1) to the instantaneous density at each time step[6]. The *exact non-adiabatic* component Δv_s is then $v_s - v_s^{\mathrm{A}}$.

5.3.1   System 1: two-electron Gaussian well

As a first test of the fluidic approximation, we consider two interacting electrons in a potential well, which takes the form of an inverted Gaussian function. Initially in the ground state, a uniform electric field, $-\varepsilon x$, is applied at $t = 0$, driving the electrons to the right and inducing a current [Fig. 5.1(a)]. The sudden application of the perturbation means that we are well outside of the adiabatic limit, and this can be seen by solving the time-dependent KS equations with the exact adiabatic KS potential, $v_s(t) = v_s^{\mathrm{A}}(t)$. By plotting the change in the electron density from the ground state,

---

[3]The rate of change of kinetic energy is proportional to $u\dot{u}$ (as in classical mechanics), and so is smallest when u is zero. Also, if the density is moving with velocity u it will more rapidly encounter a region in which a larger non-adiabatic correction is required.

[4]The stated A causes the wavefunction in the original frame to become the wavefunction in the instantaneous rest frame multiplied by $\exp(-iu^2t/2)$.

[5]See Appendix C.2 for the parameters of the model systems, and details on our calculations to obtain converged results.

[6]Our graphs show the various adiabatic and non-adiabatic KS potentials, etc., evaluated on the *exact* time-dependent density, so that any errors in the potentials or densities are entirely attributable to errors in the functionals, not the input to the functionals.

δn, we find $v_s^{\mathrm{A}}(t)$ on its own to be wholly inadequate ($\approx 13\%$ error[7] in n at $t = 8$ a.u.), while adding the fluidic approximation substantially reduces this error to less than 1% [Fig. 5.1(b)].

To understand these results we analyse the non-adiabatic correction to the KS potential in both its scalar and its vector forms. We find very good agreement between the exact ΔA_s and that obtained using the fluidic approximation $-u(x, t)$ [Fig. 5.2(a)]. The velocity field u (the negative of the fluidic curve in Fig. 5.2(a)) quickly becomes strongly non-uniform in both space and time as the electrons explore excited states – far removed from a universal rest frame. Similarly close agreement between the exact and fluidic Δv_s [Fig. 5.2(b)] is evident when the non-adiabatic correction is cast into its scalar form through Eq. (5.3).

5.3.2 Systems 2A, 2B and 2C: two- and three-electron atoms

We now consider a set of systems of interacting electrons in atomic-like external potentials which decay much more slowly at large x, $v_{\mathrm{ext}} = -a/(|x| + a)$ with $a = 20$, thereby increasing correlation. At time $t = 0$, a static sinusoidal perturbation of the form $\varepsilon \cos(0.75x)$ is applied, where ε is 0.02 for System 2A (two electrons), 0.02 for System 2B (three electrons) and 0.1 for System 2C (three electrons).

In System 2A the sudden perturbation at $t = 0$ acts to push the two electrons apart [Fig. 5.3(a)]. This results in a velocity field that is varying in both space and time, as in System 1; in this case even the sign of u is not the same for all x, which takes us even further away from a universal rest frame. Correspondingly, we find the exact adiabatic potential to be insufficient ($\approx 5\%$ error in n at $t = 5$ a.u.), while adding the fluidic approximation reduces this error to $\approx 1\%$ [Fig. 5.3(b)]. System 2B contains three interacting electrons in the same v_{ext} as System 2A. The additional electron results in a ground-state density that is much less spatially uniform [Fig. 5.4(a)]. We run the simulation for 5 a.u. of time and find similar results: v_s^{A} produces an error in n of $\approx 5\%$, and the fluidic approximation reduces this to $\approx 1\%$ [Fig. 5.4(b)].

As mentioned above, the fluidic approximation assumes that a system remains close to its ground state in the local instantaneous rest frame. In order to stretch this approximation severely, in System 2C the perturbing potential is much stronger, resulting in a much larger response of the density [Fig. 5.5(a)]. The fluidic approxima-

---

[7]The integrated absolute error, $\int dx \, |n_1(x, t) - n_2(x, t)|$, expressed as a percentage of the total number of electrons.
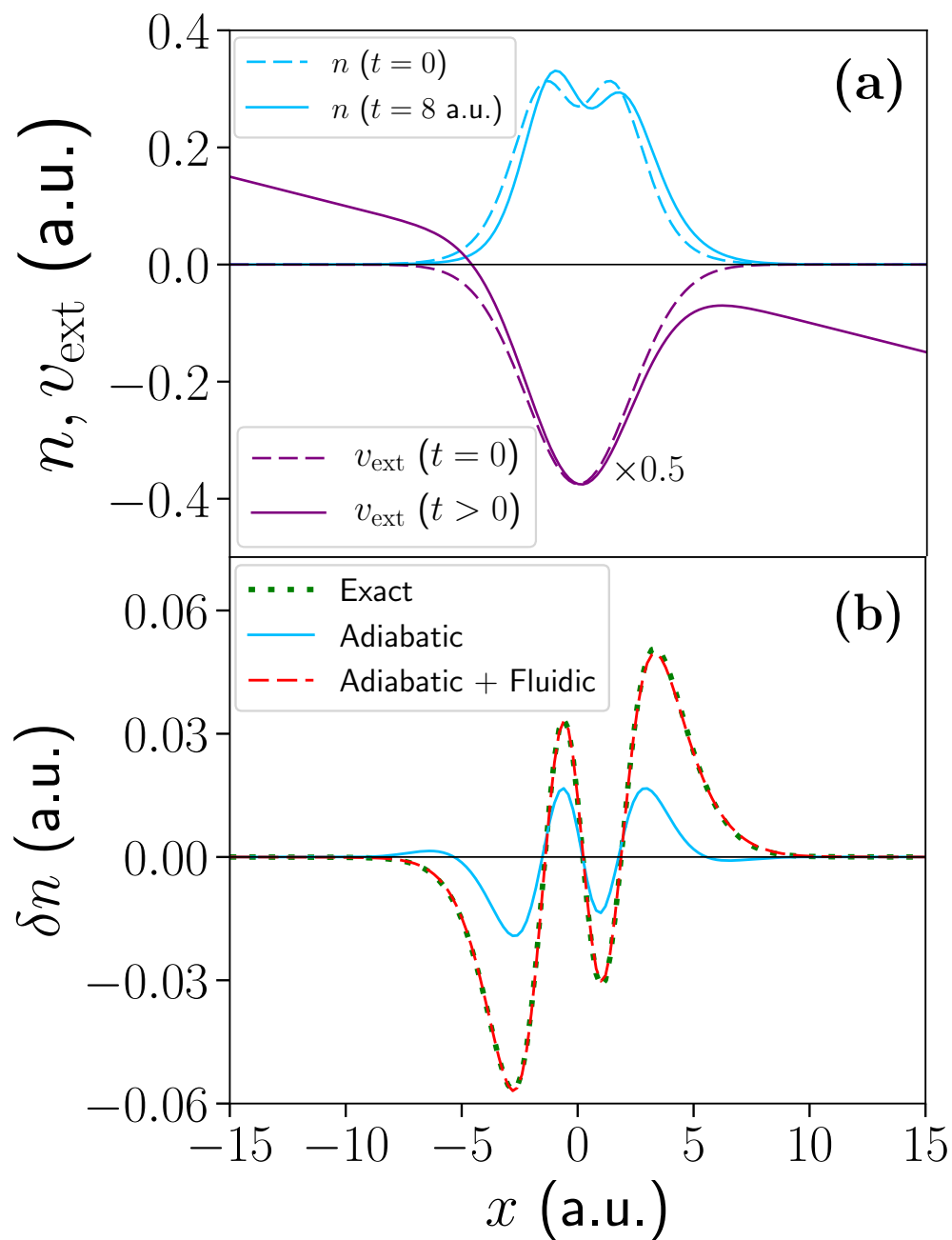
Fig. 5.1. System 1: two interacting electrons in a Gaussian potential well, with a uniform electric field applied at $t = 0$, driving the electrons to the right and inducing a current. (a) The ground-state external potential (dashed purple) and exact ground-state electron density (dashed blue), along with the perturbed external potential (solid purple) and exact time-dependent electron density at $t = 8$ a.u. (solid blue). (b) The change in the exact electron density ($\delta n(x,t) = n(x,t) - n(x,0)$) at $t = 8$ a.u. (short-dashed green), along with that obtained when using the exact v_s^A (solid blue), and when adding the exact v_s^A with the fluidic approximation $\Delta A_s = -u$ (dashed red). The exact adiabatic potential is clearly inadequate, but its error is substantially reduced by the fluidic approximation.
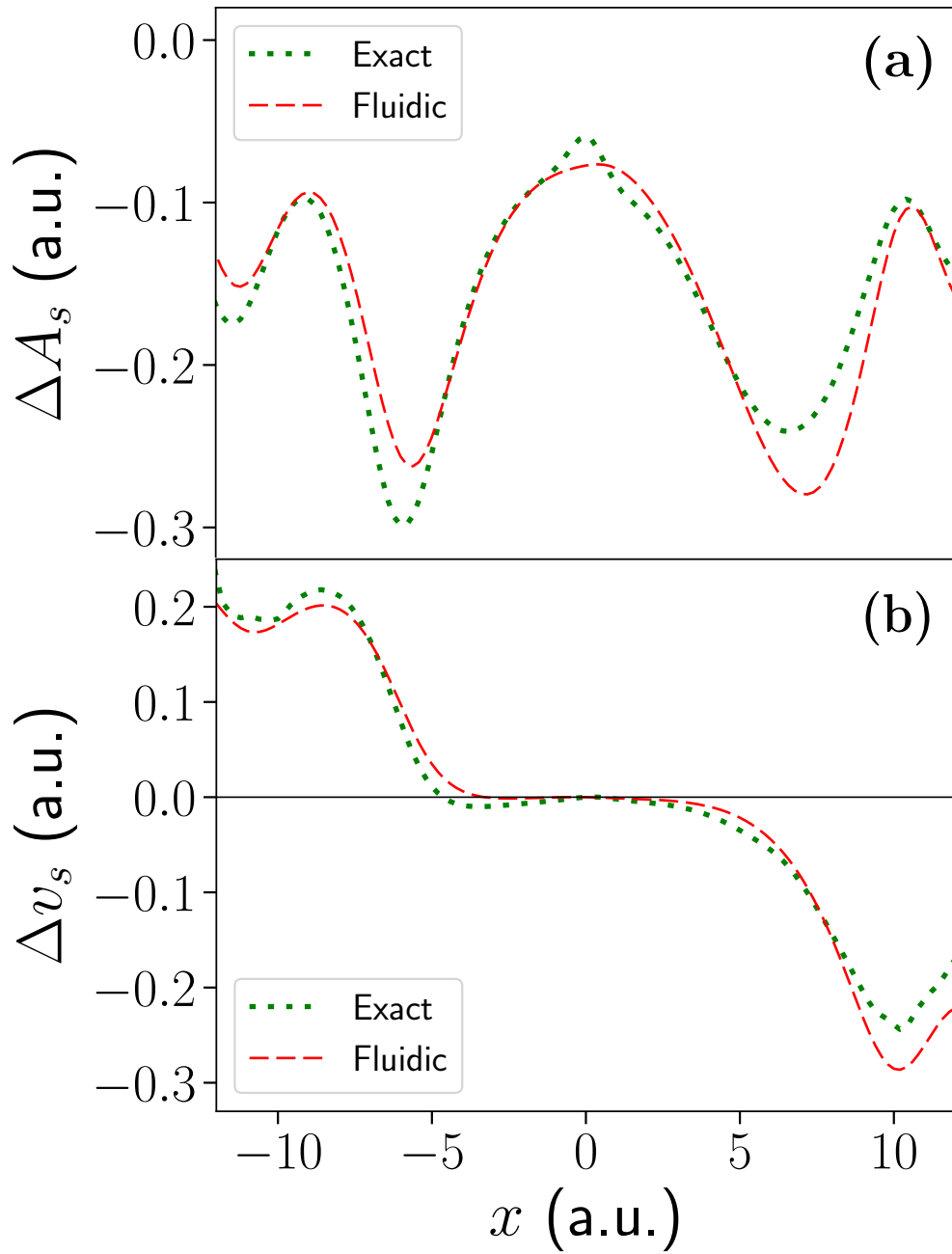
Fig. 5.2. The non-adiabatic correction to the KS potentials for System 1. (a) The exact ΔA_s (short-dashed green) and that obtained using the fluidic approximation $\Delta A_s = -u$ (dashed red), at $t = 8$ a.u. (b) The corresponding exact (short-dashed green) and fluidic (dashed red) Δv_s in its scalar form. The fluidic approximation performs very well, even though the velocity field is non-uniform in both space and time. (The exact adiabatic approximation, of course, amounts to setting $\Delta A_s = \Delta v_s = 0$.)
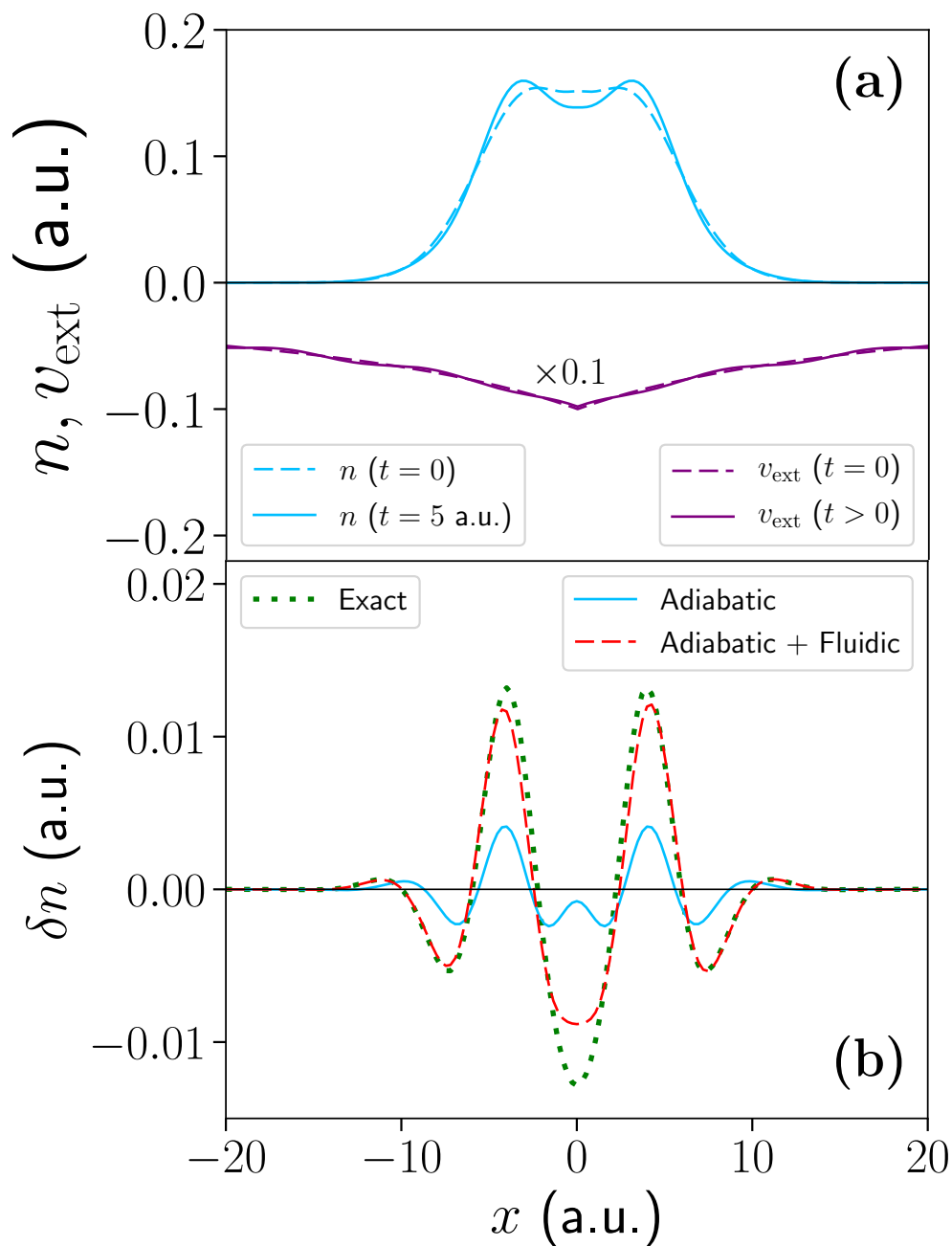
Fig. 5.3. System 2A: two interacting electrons in an atomic-like potential, with a static sinusoidal perturbation applied at $t = 0$, pushing the electrons apart. (a) The ground-state external potential (dashed purple) and exact ground-state electron density (dashed blue), along with the perturbed external potential (solid purple) and exact time-dependent electron density at $t = 5$ a.u. (solid blue). (b) The change in the exact electron density at $t = 5$ a.u. (short-dashed green), along with that obtained when using the exact v_s^A (solid blue), and when adding the exact v_s^A with the fluidic approximation (dashed red). As in System 1 (two-electron Gaussian), the exact adiabatic potential is insufficient, but its error is substantially reduced by the fluidic approximation.
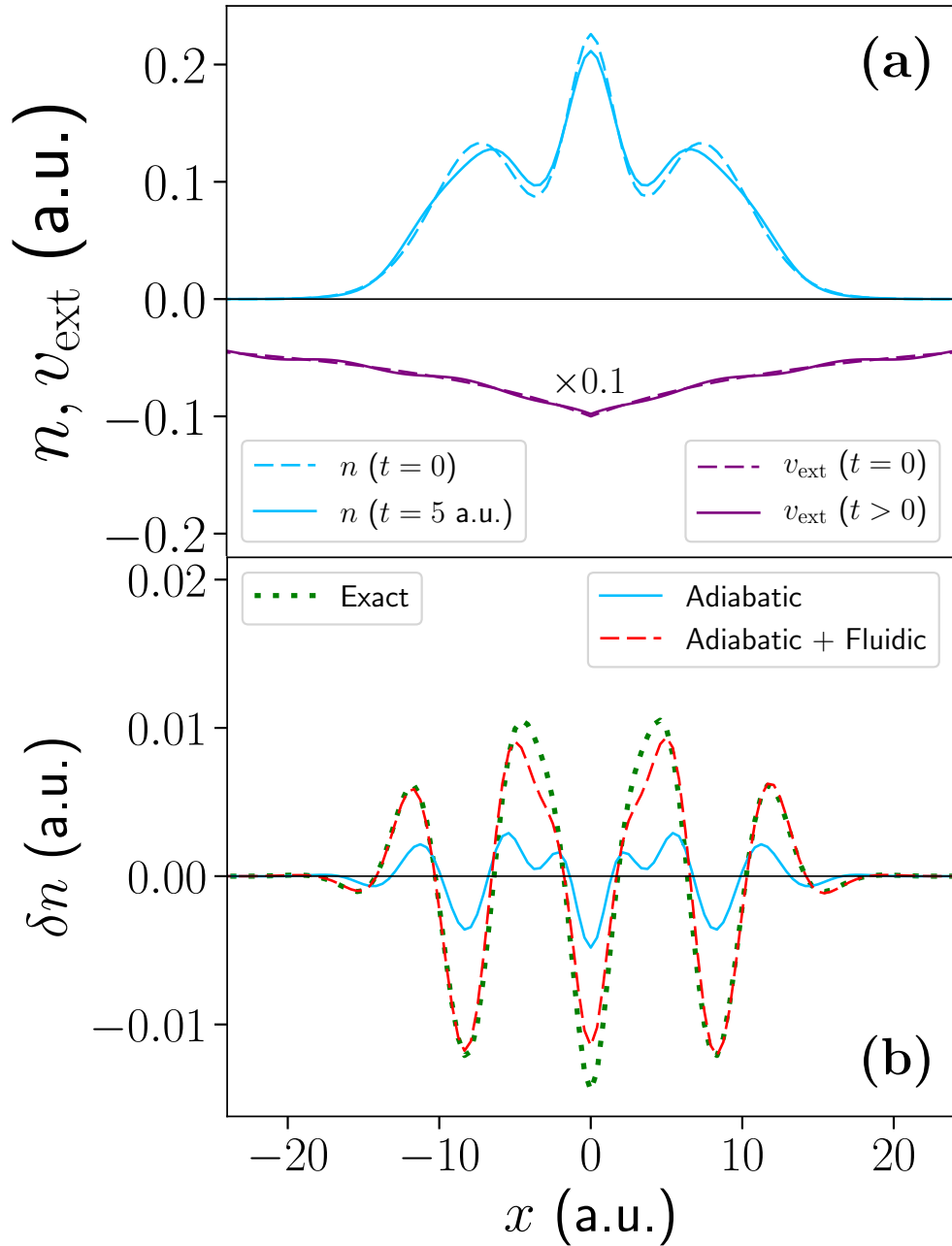
Fig. 5.4. System 2B: three interacting electrons in an atomic-like potential, with a static sinusoidal perturbation applied at $t = 0$, pushing the electrons apart. (a) The ground-state external potential (dashed purple) and exact ground-state electron density (dashed blue), along with the perturbed external potential (solid purple) and exact time-dependent electron density at $t = 5$ a.u. (solid blue). (b) The change in the exact electron density at $t = 5$ a.u. (short-dashed green), along with that obtained when using the exact v_s^A (solid blue), and when adding the exact v_s^A with the fluidic approximation (dashed red). Once again, the exact adiabatic potential performs poorly, but its error is substantially reduced by the fluidic approximation.

tion still succeeds in reducing the error in the density, from $\approx$ 25% where only the exact adiabatic potential is used, to $\approx$ 6%, at $t = 5$ a.u. [Fig. 5.5(b)]. At later times, the dynamic (time-dependent) xc effects become very significant. To confirm this, we replace the xc component of the exact time-dependent v_s with the fixed ground-state v_{xc}[8], thereby suppressing the dynamic part, and find this potential to be wholly inadequate ($\approx$ 62% error in n at $t = 18$ a.u.). Here, the exact adiabatic KS potential is better ($\approx$ 17% error), while adding the fluidic approximation improves it further ($\approx$ 15% error) [Fig. 5.5(c)].

5.3.3   Exact conditions

A number of properties of the exact xc functional are known (see Sec. 2.4.3.1), and these are often used to identify the limitations of approximate functionals. We now explore whether the fluidic approximation satisfies these exact conditions.

We begin with the *one-electron limit*, where the exact xc functional, when applied to a one-electron system, reduces to the negative of the Hartree potential v_H, thereby cancelling the spurious self-interaction. This means that v_s is described exactly by a known functional [13, 31, 138], which has been termed [167] the single orbital approximation – itself capable of capturing features such as steps in the KS potential [13, 103] – whose non-adiabatic part is

$$\Delta v_s(x,t) = -\int_{-\infty}^{x} \frac{\partial}{\partial t} u(x',t)\ dx' - \frac{1}{2} u^2(x,t). \tag{5.4}$$

We note that the first term is the fluidic approximation [Eq. (5.3)]. We have studied systems of one electron in the external potentials from Systems 1, 2A and 2C, and confirm that the full Eq. (5.4) yields the exact v_s; here, the effect on the density of including the $-u^2/2$ term ranges from $<$0.1% (potential 2A) to 14% (potential 2C), so that the fluidic approximation alone is already satisfactory. Indeed, in our two- and three-electron systems, the effect of adding the additional term to the fluidic approximation is small and typically slightly deleterious.

The *zero-force theorem* [26] follows from Newton's third law and requires the net force exerted on the system by v_H and v_{xc} to vanish. At the level of the KS potential:

$$\int n(x,t)\partial_x \Delta v_s(x,t)\ dx = \int n(x,t)\partial_x v_{ext}(x,t)\ dx, \tag{5.5}$$

---

[8]Using the exact ground-state v_{xc}, commonly known as the "adiabatically exact" approximation, allows us to identify errors solely attributable to the lack of memory dependence.
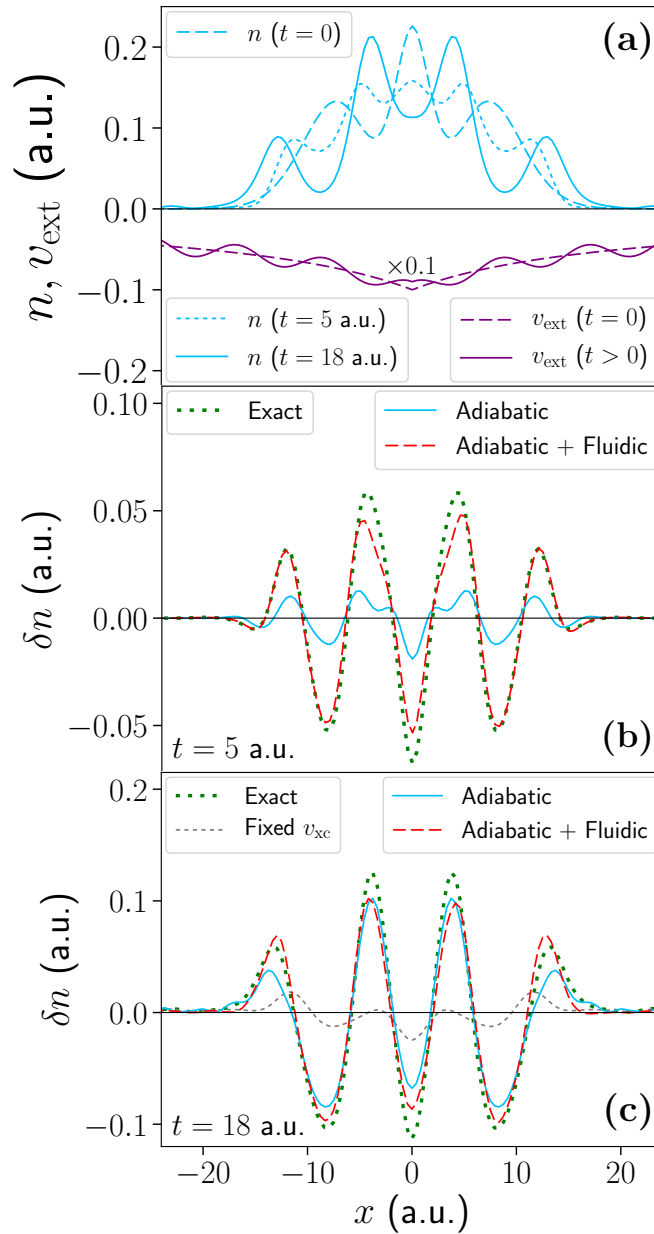
Fig. 5.5. System 2C: three interacting electrons in an atomic-like potential, with a strong, static sinusoidal perturbation applied at $t = 0$, pushing the electrons apart. (a) The ground-state external potential (dashed purple) and exact ground-state electron density (dashed blue), along with the perturbed external potential (solid purple) and exact time-dependent electron density at $t = 5$ a.u. (short-dashed blue) and $t = 18$ a.u. (solid blue). (b) The change in the exact electron density at $t = 5$ a.u. (short-dashed green), along with that obtained when using the exact v_s^A (solid blue), and when adding the exact v_s^A with the fluidic approximation (dashed red). Even though the density is strongly disrupted, the fluidic approximation remains successful. (c) The same as (b) but at $t = 18$ a.u. where the dynamic xc contribution is very significant, evident by the completely inadequate result obtained with the fixed v_{xc} (short-dashed grey) (see main text). Here, the exact v_s^A is better, but adding the fluidic approximation improves it further.

since the exact v_s^A satisfies the theorem in its own right. In the fluidic approximation for System 1[9], the left and right hand sides of this equation are within 11% of one another, so that the theorem appears to be approximately obeyed.

The *harmonic potential theorem* [27], which is a special case of generalised translational invariance [Eq. (2.29)], shows that in a system of interacting electrons in a harmonic potential, subject to a uniform electric field at $t = 0$, the density rigidly moves in the manner of the underlying classical harmonic oscillator. We have shown that the fluidic approximation adds exactly the non-adiabatic correction required (see Appendix D.4; apart from an unimportant time-dependent constant) by the HPT. We have also confirmed this numerically for two interacting electrons in a harmonic potential.

A constraint that can be challenging for non-adiabatic functionals is the *memory condition* [116], which notes that $v_{xc}(t)$ and hence $v_s(t)$ must be independent of which previous instant in the evolution of the system is to be used to designate the initial states:

$$v_s[n, \Psi(t'), \Phi(t')](x, t) = v_s[n, \Psi(t''), \Phi(t'')](x, t) \ \ \forall t > t', t''. \tag{5.6}$$

This is violated by the VK functional [31]. Eq. (5.3) demonstrates that the fluidic approximation satisfies this memory condition by virtue of its dependence only on the instantaneous rate of change of u, and not its full history.

5.3.4 System 3: two-electron tunnelling system

As a challenging test of the fluidic approximation, we finally consider two interacting electrons in a tunnelling system. Initially v_{ext} is a symmetric double-well potential, with one electron localised in each well. At $t = 0$, the left-hand well is raised and the right-hand well lowered, initiating tunnelling through the barrier [Fig. 5.6(a)]. A tunnelling electron has an imaginary momentum, meaning that the (real) velocity field is of less physical significance. Correspondingly, the fluidic approximation recovers less of the adiabatic density error, but nevertheless reduces it from $\approx 8\%$ to $\approx 4\%$, at $t = 15$ a.u. Accordingly, the tunnelling rate from the left-hand side to the right-hand side is initially improved, but this is not the case at later times [Fig. 5.6(b)].

---

[9]Systems 2A, 2B and 2C satisfy the theorem owing to their symmetry, so do not form a useful test.
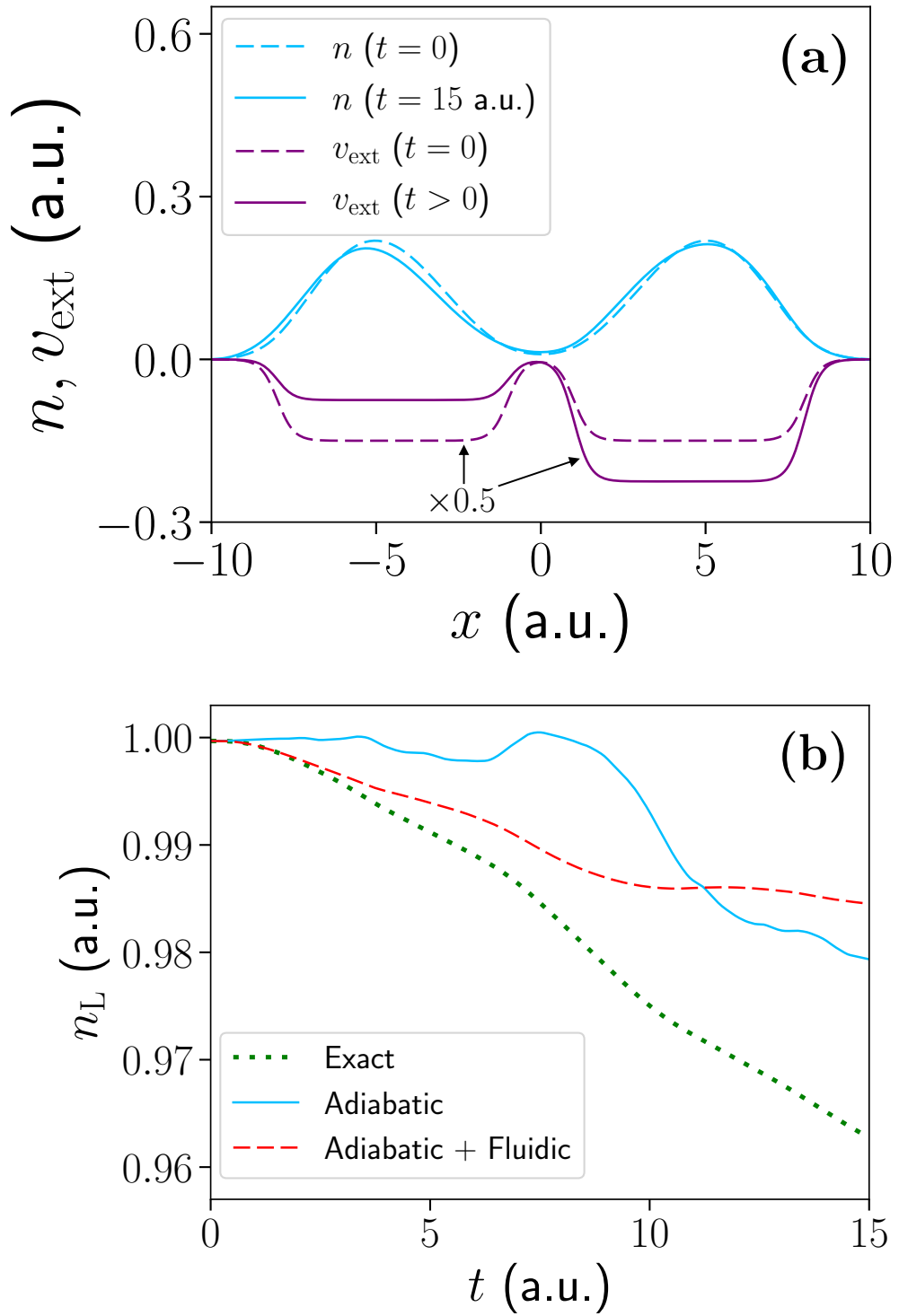
Fig. 5.6. System 3: two interacting electrons in a tunnelling system. (a) The ground-state external potential (dashed purple) and exact ground-state electron density (dashed blue), along with the perturbed external potential (solid purple) and exact time-dependent electron density at $t = 15$ a.u. (solid blue). (b) The exact total electron number on the left-hand side ($x < 0$) (short-dashed green); also the exact adiabatic (solid blue) and fluidic approximation (dashed red).

5.4 Conclusions

In summary, we have calculated the *exact* adiabatic and non-adiabatic parts of the KS potential, v_s^A and Δv_s, for a variety of model systems. Δv_s is precisely defined by our procedure, and represents the part of the time-dependent KS potential that is *intrinsically unobtainable from a ground-state functional*. Our key finding is that a simple geometrical approximation to this non-adiabatic KS potential – making use of a Galilean transformation to the local instantaneous rest frame – recovers most of the density error attributable to the exact adiabatic approach: typically $80 - 95\%$ in the ballistic systems studied.

As discussed extensively in Sec. 2.6.2, most approximate TDDFT functionals utilise an adiabatic approach, which severely limits the application of TDDFT to a multitude of diverse fields. Here, an adiabatic approach typically entails combining the time-dependent external and Hartree potentials with a ground-state xc potential. In contrast, in this chapter we have considered the purest application of the concept of the adiabatic functional to the complete KS potential, with the remainder constituting the unambiguously non-adiabatic part, thereby removing any inconsistency. We have found that combining the exact v_s^A with a simple fluidic approximation to Δv_s performs well, even in highly non-adiabatic situations. Studies of additional systems should further illuminate this decomposition of the KS potential of TDDFT in highly non-adiabatic situations, with the fluidic approximation providing a solid foundation for a hierarchy of approximations to Δv_s. This may provide an alternative method to conduct TDDFT calculations and lead to improved results in situations where the typical adiabatic xc functionals are insufficient. Identifying the most appropriate implementation of the fluidic approximation in practical calculations forms another line of research.

EXACT EXCHANGE-CORRELATION KERNELS FOR MODEL SYSTEMS[1]

As discussed in Chapter 2, the validity of time-dependent DFT (TDDFT) in practical applications is predicated on the available approximate exchange-correlation (xc) functionals. The exchange-correlation kernel, f_{xc}, is the key quantity in many important spectroscopies, but the most commonly used approximate kernels are adiabatic and (semi-) local, thereby severely restricting their success. In this chapter, we calculate the exact $f_{xc}(x, x', \omega)$ for prototype systems, in order to inform the development of improved approximate functionals. We find that, up to the first excitation energy, the exact f_{xc} has weak frequency-dependence and a simple, though non-local, spatial form. For higher excitations, the spatial behaviour and frequency-dependence become more complex. The accuracy of the underlying exchange-correlation potential is of crucial importance.

---

[1]This chapter represents work that has been published: M. T. Entwistle and R. W. Godby, 'Exact exchange-correlation kernels for optical spectra of model systems', *Phys. Rev. B* **99**, *161102(R) (2019)*. The sections of this chapter have been adapted from the publication. Additionally, parts of some sections (Sec. 6.2, Sec. 6.3.3 and Sec. 6.3.4) have been extended and represent collaborative work that is being prepared for publication: M. T. Entwistle, N. D. Woods and R. W. Godby, 'Insights from exact exchange-correlation kernels'.

6.1   Introduction

As discussed in Sec. 2.4, TDDFT is in principle an exact and efficient theory of the excited-state properties of many-electron systems, including a wide variety of important spectroscopies such as optical absorption spectra of molecules and solids. However its application is restricted by the limitations of the available approximate functionals for electron exchange and correlation – in particular the exchange-correlation kernel f_{xc}, the functional derivative of the exchange-correlation potential with respect to the electron density (see Sec. 2.5.3). Within the framework of linear response theory (see Sec. 2.5), the induced density is described by the interacting density-response function, the functional derivative $\chi = \delta n / \delta v_{ext}$. χ is related to the non-interacting density-response function of the KS system, $\chi_0 = \delta n / \delta v_s$, by the Dyson equation $\chi = \chi_0 + \chi_0 (u + f_{xc}) \chi$ [Eq. (2.45)]. χ_0 is to be obtained from a ground-state DFT calculation. χ can then be used to compute, for example, the optical absorption spectrum of the system [Eq. (2.55)]:

$$\sigma(\omega) = -\frac{4\pi\omega}{c} \int dx \int dx' \, \text{Im}\big[\chi(x, x', \omega)\big] \, x \, x'. \qquad (6.1)$$

In practice, both v_{xc} and f_{xc} must be approximated. While there have been some successes and linear-response TDDFT offers a unique compromise between accuracy and computational efficiency, problems remain in many important circumstances, as discussed in Sec. 2.6.2. In finite systems, the use of accurate approximate kernels becomes important in systems with strong correlation or when a description of higher excitations (such as Rydberg series) is needed. Furthermore, the commonly used adiabatic TDDFT functionals, such as the adiabatic LDA (ALDA), are incapable of describing multiple excitations or excitations of a charge-transfer nature. They also fail in extended systems. For example, the optical absorption spectra of many semiconductors and insulators are not even qualitatively described, with excitonic effects and many-electron excitations omitted, and the optical gap underestimated. Here, approximations for f_{xc} achieve little improvement over the random phase approximation (RPA), in which f_{xc} is neglected entirely. Attempts to improve approximations for f_{xc} include exact-exchange methods, diagrammatic expansions using perturbative methods, and adding long-range contributions. Another approach involves calculations of the homogeneous electron gas (HEG). Kernels derived from the Bethe-Salpeter equation have had some success, but require a relatively expensive many-body perturba-

tion theory calculation as their input, and are outside the KS TDDFT framework.

There have been a limited number of studies conducted on analysing the character of the exact f_{xc}, all of which focus on its frequency-dependence. One approach has been to calculate the exact adiabatic f_{xc} for model systems [168], in order to investigate its performance upon application and deduce when memory effects become important. This approach has been used in simple Hubbard systems [169, 170] and extended by analysing additional properties, such as the frequency-dependence of the full f_{xc} around double excitations. Other research has explored how this frequency-dependence of f_{xc} turns the single-particle quantities of exact KS TDDFT into many-body excitations [171] and its behaviour for long-range excitations has been analysed in order to develop approximate kernels [82]. Whilst this previous research has provided important understanding of the nature of the exact f_{xc}, it has its own limitations by its focus on individual characteristics.

In this chapter, we explore the properties of exact xc kernels, in order to inform the development of improved approximate functionals. We show the explicit spatial dependence of the exact dynamic f_{xc} – which when combined with its frequency-dependence, displays its full features. As stated above, the usual approximations to f_{xc} are known to have severe limitations, and attempts to improve upon them have often focused on addressing the frequency-independence of adiabatic kernels, or introducing non-locality to local kernels, rather than a mixture of the two. We believe that calculating the full dynamic f_{xc} opens up this possibility. Furthermore, knowledge of the spatial dependence of the exact f_{xc} provides a strong indication of whether it is amenable to approximation, e.g. through a simple non-local kernel.

6.2 Computing f_{xc}

As mentioned in Sec. 2.5.3 and Sec. 3.1.4.2, the Dyson equation can be rearranged to give an expression for the xc kernel in terms of χ and χ_0:

$$f_{xc}(x, x', \omega) = \chi_0^{-1}(x, x', \omega) - \chi^{-1}(x, x', \omega) - u(x, x'). \tag{6.2}$$

6.2.1 Inverting the density-response functions[2]

As discussed in Sec. 3.1.4.2, the inverses of χ and χ_0 are not well defined, with both having zero, and near-zero, eigenvalues. The zero eigenvalue (and hence zero determinant) present in both χ and χ_0 represents the vanishing density response that arises from a spatially uniform perturbation, $\delta v_{ext}(x, \omega) = c(\omega)\ (= \delta v_s(x, \omega))$ [172]. Near-zero eigenvalues, which also pose numerical difficulties when calculating the inverses of the response functions, represent perturbations that induce small density responses, e.g. those with very high spatial frequencies with respect to system size. To overcome these issues, we find pseudo-inverses of χ and χ_0 using truncated singular-value decomposition (SVD). Here, an eigendecomposition of each matrix is performed [172]:

$$\chi^{-1}(x, x', \omega) = \sum_l \frac{1}{\lambda_l(\omega)} \zeta_l(x, \omega) \zeta_l^*(x', \omega), \tag{6.3a}$$

$$\chi_0^{-1}(x, x', \omega) = \sum_l \frac{1}{\lambda_{l,s}(\omega)} \zeta_{l,s}(x, \omega) \zeta_{l,s}^*(x', \omega), \tag{6.3b}$$

where $\{\lambda_l, \zeta_l\}$ and $\{\lambda_{l,s}, \zeta_{l,s}\}$ are the eigenvalue-eigenvector pairs of χ and χ_0, respectively. The pseudo-inverses $\chi^\dagger$ and $\chi_0^\dagger$ are the solutions to [173]

$$\min_{\chi^\dagger} \|\chi \chi^\dagger - I\|, \tag{6.4a}$$

$$\min_{\chi_0^\dagger} \|\chi_0 \chi_0^\dagger - I\|, \tag{6.4b}$$

where $\|\ \|$ is the Euclidean norm and I is the identity matrix. We attain these by removing eigenvalues below machine precision in Eq. (6.3a) and Eq. (6.3b). These eigenvectors with near-zero eigenvalues define our "null" space: the directions in which perturbations to our potential produce negligible density response, and do not meaningfully contribute to the true response functions and absorption spectra. We are in effect inverting our response functions in the remaining "active" space: the directions in which perturbations to our potential produce meaningful density response. We have to be careful when determining these active spaces, but find there is a near-perfect overlap between the active space of the interacting system and that of the KS system, resulting in the eliminated null spaces effectively cancelling.

---

[2]In Ref. 106 we performed our calculations using this SVD procedure. However, we only retained the few largest eigenfunctions of χ and χ_0 when inverting in their respective subspaces. The implementation of this SVD procedure was subsequently improved by N. D. Woods, ensuring all eigenfunctions with corresponding eigenvalues above machine precision are retained, and so the results presented in this chapter vary slightly from those presented in the publication, to reflect the increased accuracy obtained.

6.2.2 Verification of procedure

From the modified response functions we obtain a kernel f_{xc}. We confirm the validity of this procedure by verifying that the calculated f_{xc}, together with the unmodified χ_0, closely reproduces the unmodified χ via the Dyson equation. Additionally, we ensure that the zero-force sum rule is obeyed (see Appendix C.3) – a well known property of the exact f_{xc} (see Sec. 2.5.3.1; Eq. (2.51)).

6.2.3 Gauge freedom in f_{xc}

As stated above, a spatially uniform perturbation, or constant vector $|c\rangle$, will induce a density response $0|c\rangle$. This is true in both the interacting and KS systems, and so both χ and χ_0 share this eigenvector. As such, an eigendecomposition of each response function will include the term $0|c\rangle\langle c|$. Now, Eq. (6.2) can be rearranged to give

$$\chi = \left[I - \chi_0(f_{xc} + u)\right]^{-1}\chi_0. \tag{6.5}$$

If we were to add a term $\alpha|c\rangle\langle c|$ to f_{xc}, we can see this leads to the additional product $\chi_0\,\alpha|c\rangle\langle c|$ within the inverse. As the eigenvectors of χ_0 form an orthonormal basis, the only surviving term is $0|c\rangle\langle c|\alpha|c\rangle\langle c| = 0|c\rangle\langle c|$, and so the resultant χ will remain the same. We are therefore free to add a constant to f_{xc}, in much the same way we are free to add a constant to v_{xc}. We choose the convention $f_{xc} + u \to 0$ as $|x - x'| \to \infty$.

6.3 Calculations

6.3.1 Adiabatic limit and low frequency

System 1: two-electron harmonic well. We begin by considering a system of two interacting electrons confined to a harmonic well potential ($\omega_0 = 0.25$ a.u.), where ω_0 is the angular frequency of the well [Fig. 6.1(a)]. We compute the exact optical absorption spectrum of the system, and find only the first excitation at $\omega = \omega_0$ appears[3] [Fig. 6.1(b)]. Additionally, we compute the absorption spectrum of the exact Kohn-Sham system, in which the absorption frequency is slightly too low (≈ 0.01 a.u.). We

---

[3]For a one-electron harmonic well system, at the level of linear response theory, only one excitation appears in the absorption spectrum, due to selection rules. Specifically, as we are working in the dipole approximation, a transition can only occur between states whose principal quantum numbers differ by unity. As the system is initially in the ground state (n = 0), the only allowed transition is to the first excited state (n = 1). Here, we observe this in the two-electron harmonic well system.

also calculate the RPA and ALDA absorption spectra, in which the RPA and ALDA kernels[4] are combined with the *exact*[5] χ_0. This last point provides a strong reminder of the challenge of f_{xc}: starting from the exact Kohn-Sham orbitals, which require the exact Hartree and xc potentials of the unperturbed system, a much better absorption peak is obtained by ignoring the induced changes in the Hartree and xc potentials (χ_0) than by accounting for the first exactly and either neglecting (RPA) or approximating (ALDA) the second. Furthermore, if we choose to start from the LDA orbitals and energies, the approximate χ_0 obtained (not shown) has an absorption frequency that is ≈ 0.03 a.u. lower than the true absorption frequency, which is a factor of 3 greater than that of the exact χ_0 (≈ 0.01 a.u. too low). This highlights the importance of obtaining a good approximation to the ground-state xc potential v_{xc}, as discussed in Sec. 2.6.2.1.

We now turn to the spatial characteristics of f_{xc} [Fig. 6.2]. We observe that while f_{xc} has real and imaginary parts (see later), the real part alone is sufficient to reproduce the position and weight of the first excitation ($\omega = \omega_0$). Fig. 6.2(a) and Fig. 6.2(b) show $\text{Re}(f_{xc})$ at $\omega = 0$ and ω_0, respectively. The behaviour of f_{xc} away from the diagonal, $x \neq x'$, represents the kernel's non-locality, and it is evident that this is fairly simple in nature; analysis [Fig. 6.2(c)] shows it to be similar to the negative of the Coulomb interaction, with which it therefore tends to cancel in the expression for χ. The ω-dependence of f_{xc} up to the first excitation is seen to be extremely weak, as observed in other model systems [169–171]. We analyse this more closely in Fig. 6.2(d).

To gain insight into these observations, we analyse the exact χ and χ_0. Fig. 6.3 shows $\text{Re}(\chi)$ and $\text{Re}(\chi_0)$; up to the first excitation, these exhibit strong – but closely similar – ω-dependence. The similarity arises in part from the exact many-electron wavefunction being well approximated by the exact Kohn-Sham wavefunction[6], which reflects the dominance of exchange (including self-interaction correction) in the harmonic potential system[7]. Therefore χ^{-1} and χ_0^{-1} largely cancel, so that f_{xc} is similar to $-u$, with weak ω-dependence.

---

[4]We use the LDA constructed from two-electron "slab" systems, as reported in Ref. 174 and presented in Chapter 4.

[5]We use the exact χ_0 (constructed through knowledge of the exact ground-state v_{xc}) so that any error in the resultant χ can be attributed solely to the approximate xc kernels used.

[6]We define this as a Slater determinant of the occupied KS orbitals.

[7]E. Richardson, private communication.
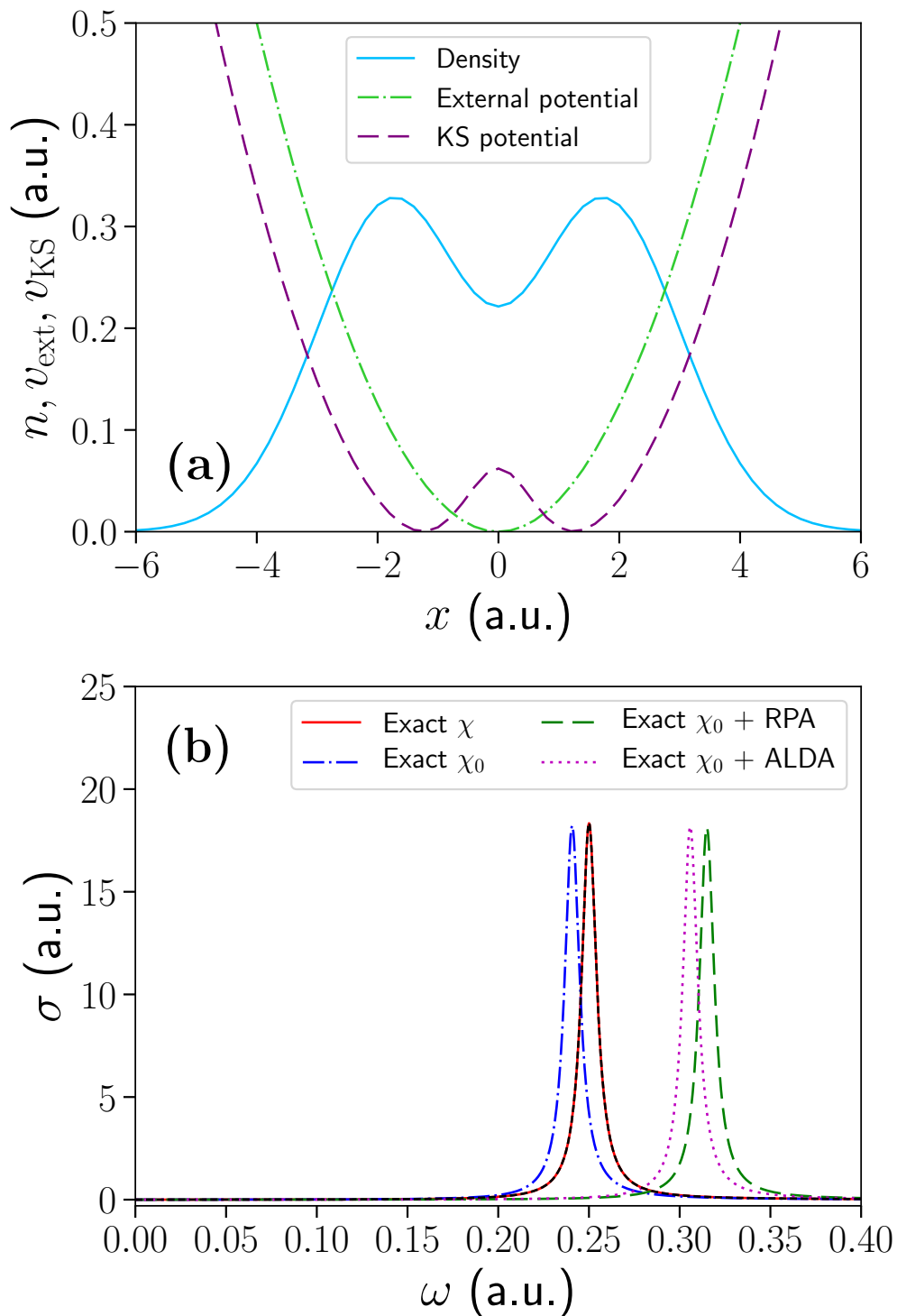
Fig. 6.1. System 1: two interacting electrons in a harmonic potential. (a) The electron density (solid blue), along with the external (dotted-dashed green) and exact Kohn-Sham (dashed purple) potentials. (b) The absorption spectra (detailing the first excitation) of the exact (solid red) and Kohn-Sham (dotted-dashed blue) systems, along with the RPA (dashed green) and ALDA (dotted magenta) approximations. We check that the calculated f_{xc} is correct by solving the Dyson equation and comparing the resultant absorption spectrum (short-dashed black) with the exact.

$$\mathrm{Re}(f_{\mathrm{xc}})$$
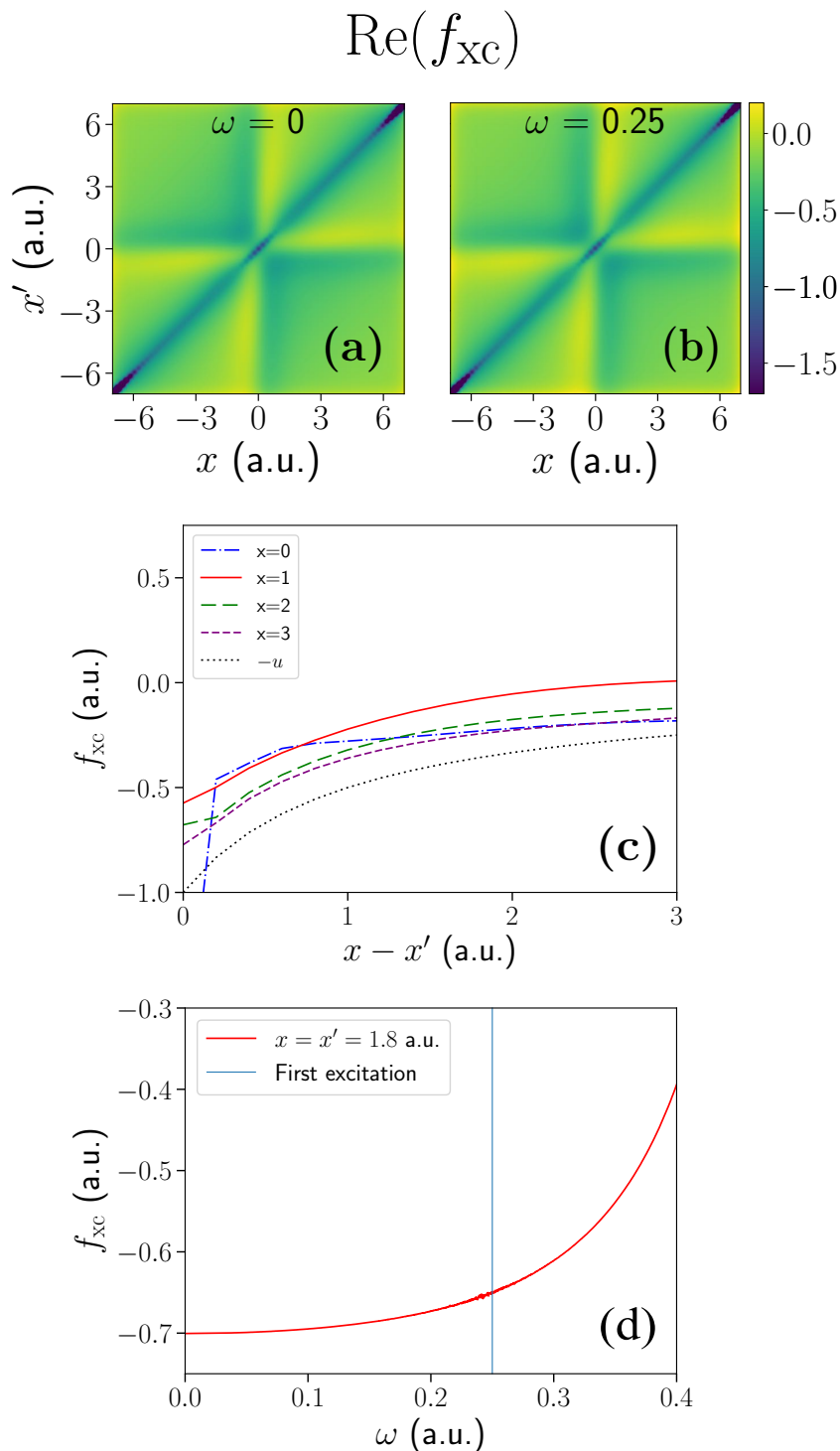
Fig. 6.2. The real part of the exact f_{xc} of the harmonic well system: (a) In the adiabatic limit ($\omega = 0$), and (b) at the first excitation ($\omega = 0.25$). (c) f_{xc} has a rather simple non-local dependence, which is similar to the negative of the Coulomb interaction u. Here we focus on f_{xc} at $\omega = 0.25$ and analyse its variation with $x - x'$. (The sharp change in the dotted-dashed blue curve ($x = 0$) close to $x - x' = 0$ arises due to the discretised spatial grid.) (d) We observe f_{xc} to have strikingly weak ω-dependence up to the first excitation (vertical line). We illustrate this by plotting its value (solid red) at a point along the main diagonal ($x = x'$) which corresponds to the peak in electron density in Fig. 6.1(a) ($x = 1.8$ a.u.).
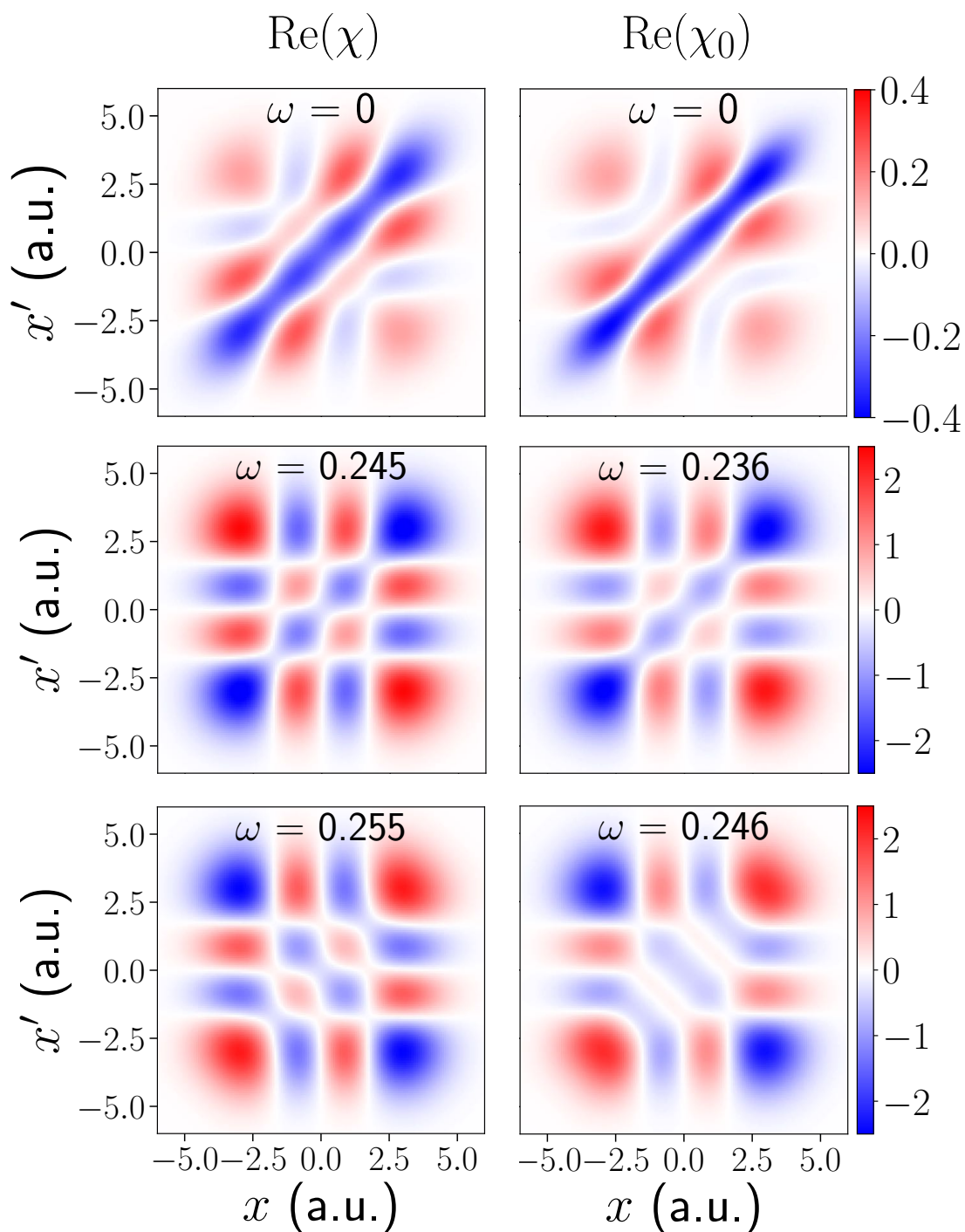
Fig. 6.3. The exact χ and χ_0 in the harmonic well system: Left: Re(χ) at $\omega = 0$ and on either side of the transition at 0.250. Right: Re(χ_0) at $\omega = 0$ and on either side of the transition at 0.241. Re(χ) and Re(χ_0) exhibit remarkably similar spatial structure.

6.3.2 Insight using a simple toy model

The above results can be demonstrated succinctly through a simple model, in which we take Eq. (2.35) and Eq. (2.38) (the Lehmann representation of χ and χ_0, respectively), and replace the spatially-dependent numerators (the oscillator strengths) with scalars. Specifically, we consider a system with a single excitation at $\omega = 1$, set the numerator equal to 1, and let $\eta = 0.05$ (inset of Fig. 6.4(a)). We do the same for the Kohn-Sham system, but choose the excitation to occur at $\omega = 0.9$. The density-response functions therefore become

$$\chi(x,x,\omega) = \frac{1}{\omega - 1 + 0.05i} - \frac{1}{\omega + 1 + 0.05i}, \tag{6.6a}$$

$$\chi_0(x,x,\omega) = \frac{1}{\omega - 0.9 + 0.05i} - \frac{1}{\omega + 0.9 + 0.05i}. \tag{6.6b}$$

By taking their inverses, we calculate $\mathrm{Re}(\chi_0^{-1} - \chi^{-1})$, which is the ω-dependent part of $\mathrm{Re}(f_{xc})$ in Eq. (6.2), and find this to be small in amplitude and have a fairly weak ω-dependence up to the first excitations [Fig. 6.4(b)]. The inclusion of higher excitations, and taking the limit $\eta \to 0$, change little at these low frequencies.

Including higher excitations in the model χ causes $\mathrm{Re}(\chi)$ to pass through zero between excitations. At these points $\mathrm{Re}(\chi^{-1})$ also passes through zero, and $\mathrm{Im}(\chi^{-1})$ peaks sharply [Fig. 6.4(a)]. As $\mathrm{Im}(f_{xc}) = \mathrm{Im}(\chi_0^{-1} - \chi^{-1})$, we find that the f_{xc} in our simple model only has an imaginary component when χ or χ_0 passes through zero between excitations, and hence is completely real up to the first excitations (as $\eta \to 0$). This supports our finding in the harmonic well system, in which $\mathrm{Im}(f_{xc})$ was very small up to the first excitations, and $\mathrm{Re}(f_{xc})$ was sufficient to reproduce the peak in the absorption spectrum. Additionally, f_{xc} in our simple model is well behaved up to the first excitation and around all additional excitations, with poles only appearing in between excitations (when the real part passes through zero and the imaginary part peaks). This agrees with the analysis of the exact f_{xc} for finite systems as reported in Ref. 172.

6.3.3 Higher excitations

System 3: two-electron atom. We now consider a system whose absorption spectrum includes higher excitations – two interacting electrons in a softened atomic-like potential [Fig. 6.5(a)]. As in the harmonic well system, the absorption spectrum of the
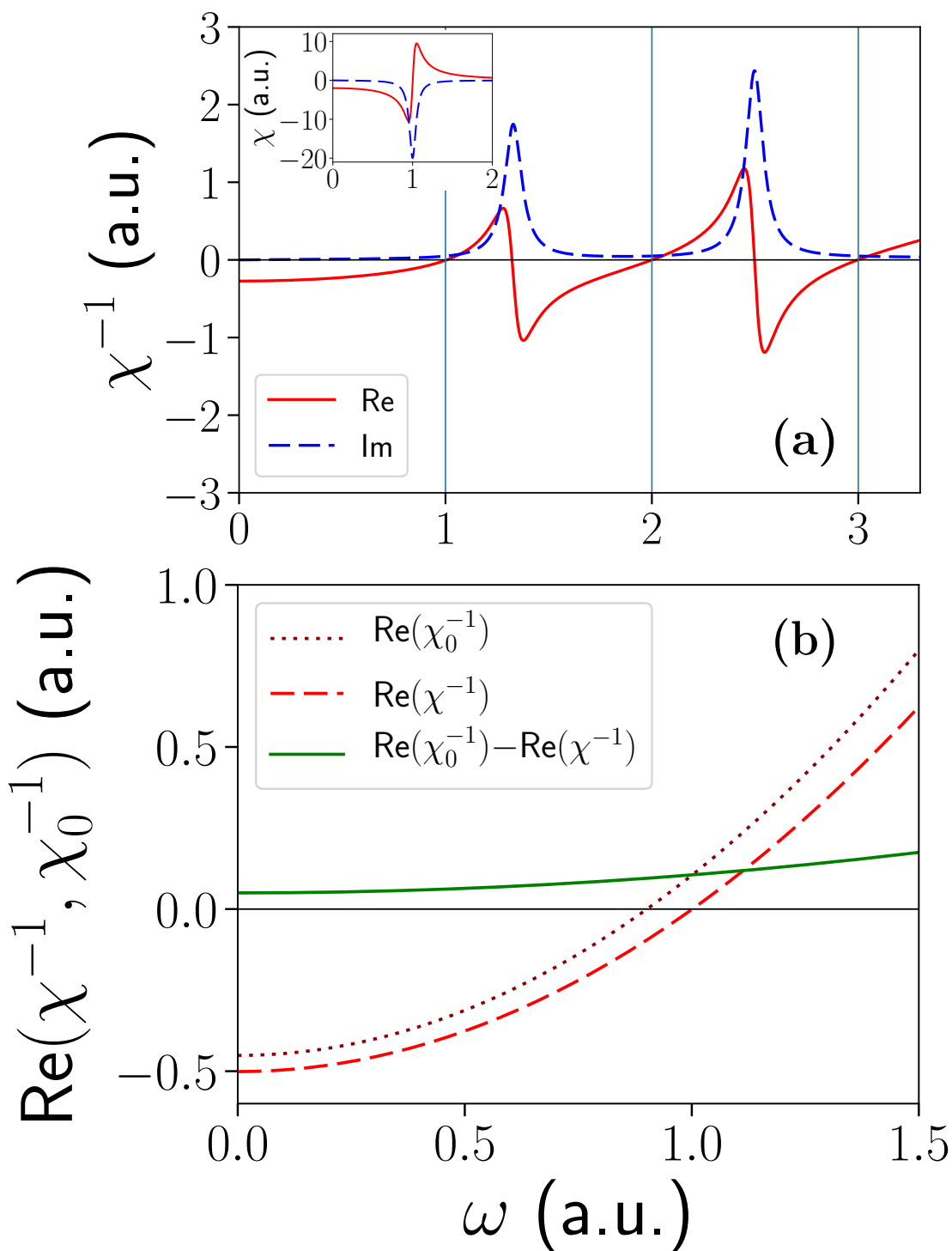
Fig. 6.4. System 2: a simple toy model. The inset shows χ for a simple toy model without spatial dependence and a single excitation at $\omega = 1$. (a) Two further excitations at $\omega = 2$ and 3 have been included, to show that $\text{Re}(\chi^{-1})$ passes through zero between excitations, which leads to a non-zero $\text{Im}(f_{\text{xc}})$, as does the corresponding feature in χ_0^{-1} (not shown). (b) The near cancellation (solid green) between $\text{Re}(\chi^{-1})$ (dashed red) and $\text{Re}(\chi_0^{-1})$ (dotted dark red), where χ_0 has an excitation at 0.9, causing f_{xc} to exhibit weak ω-dependence up to these first excitations.

exact Kohn-Sham system is slightly too low for the first excitation[8] [Fig. 6.5(b)]. Again, we find f_{xc} to be dominated by its real part and nearly ω-independent, while exhibiting relatively simple spatial structure, up to and including the first excitation (see Fig. 6.6(a) and Fig. 6.6(b)). The second excitation ($\omega = 0.0859$) does not appear in the absorption spectrum, but again we find the corresponding excitation in the KS system to be slightly too low ($\omega = 0.0825$), with χ and χ_0 exhibiting more complex but very similar behaviour to one another (see later), leading to little change in f_{xc} [Fig. 6.6(c)]. Moving to the third excitation[9], which does appear in the absorption spectrum but is much smaller in amplitude than the first, we once more observe the peak in the Kohn-Sham system to be slightly below but still very close to the exact[10] (inset of Fig. 6.5(b)). Again, the closeness between the two peaks arises from the similarity between χ and χ_0. In order to reproduce this excitation, higher spatial frequencies in f_{xc} are needed[11] [Fig. 6.6(d)]. As we progress to higher transitions, f_{xc} continues to acquire additional spatial structure and stronger ω-dependence [Fig. 6.6(e)].

Once more, we analyse the exact χ and χ_0 [Fig. 6.7]. As in the harmonic well system, $\mathrm{Re}(\chi)$ and $\mathrm{Re}(\chi_0)$ display strong but similar ω-dependence up to the first excitation (first row of Fig. 6.7), resulting in χ^{-1} and χ_0^{-1} largely cancelling, and hence leading to simplicity in f_{xc}. This behaviour of f_{xc} is maintained up to the second excitation, in which the density response functions acquire additional spatial structure, but continue to look alike (second row of Fig. 6.7). Interestingly, this continues to be the case near the third *KS excitation* (third row of Fig. 6.7), even though the corresponding excitation in the interacting system is at higher ω. Moving to the third excitation in the interacting system (fourth in the KS system), both χ and χ_0 have developed more elaborate structure (fourth row of Fig. 6.7), and also differ to a certain degree, giving rise to increased complexity in f_{xc}. If we move to higher frequencies, this progression persists.

---

[8]If we use the LDA orbitals and energies to construct χ_0, the error is a factor of 6-7 greater.

[9]The third excitation in the interacting system corresponds to the fourth excitation in the KS system. The third excitation in the KS system manifests at higher ω in the interacting system, but is suppressed in both absorption spectra.

[10]If we use the LDA orbitals and energies to construct χ_0, the peak is above that of the exact χ, and much too small in amplitude. The exact χ_0 corrects the peak height by a factor of 2-3, and reduces the discrepancy in position by $\approx 30\%$.

[11]As expected for higher energy excited states.
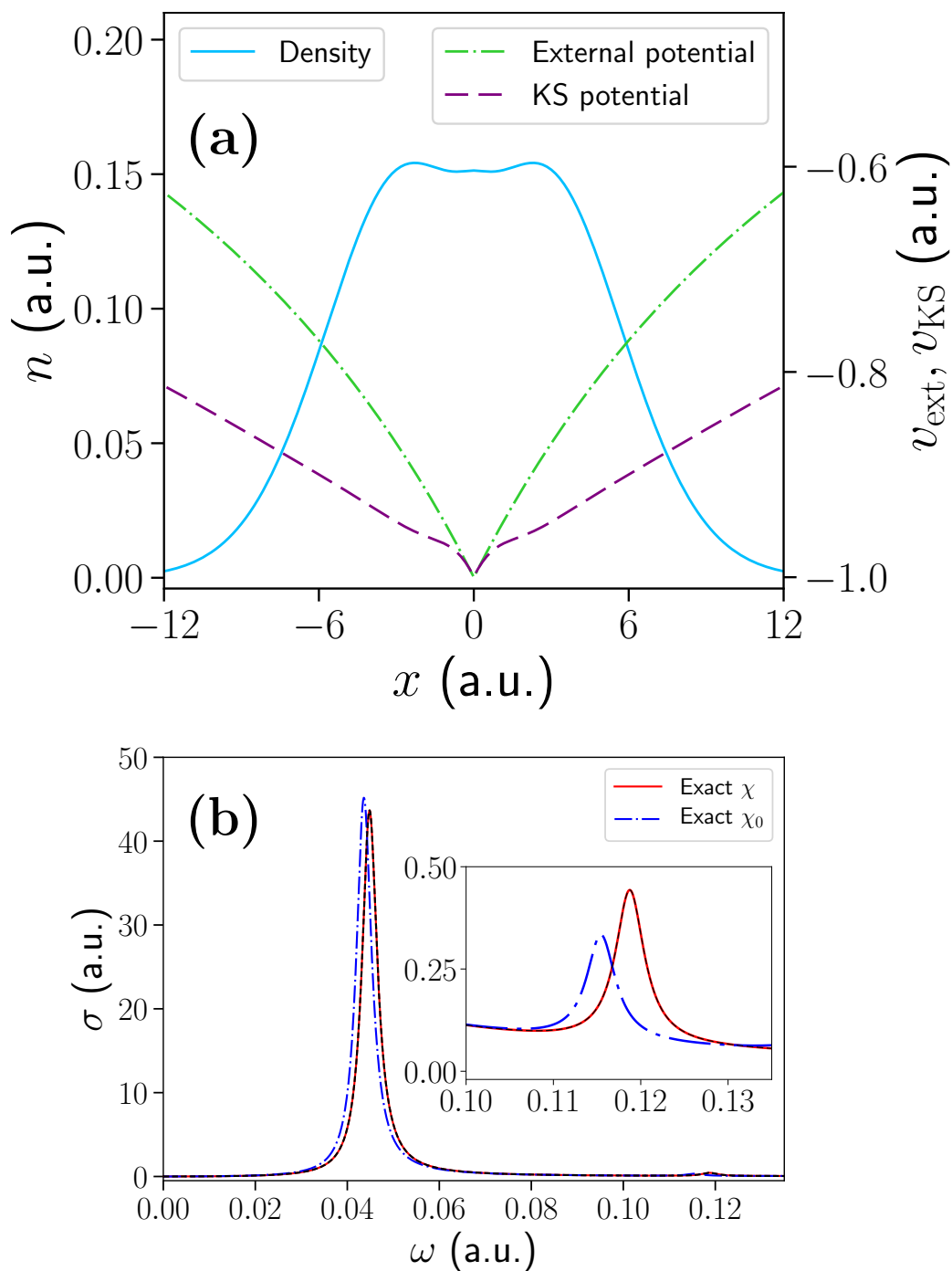
Fig. 6.5. System 3: two interacting electrons in an atomic-like potential. (a) The electron density (solid blue), along with the external (dotted-dashed green) and exact Kohn-Sham (dashed purple) potentials. (b) The absorption spectra of the exact (solid red) and Kohn-Sham (dotted-dashed blue) systems; the inset shows the third excitation (fourth in the KS system) in more detail, which is the next to appear after the first excitation. As in the harmonic well system, we check that the calculated f_{xc} is correct by solving the Dyson equation and comparing the resultant absorption spectrum (short-dashed black) with the exact.
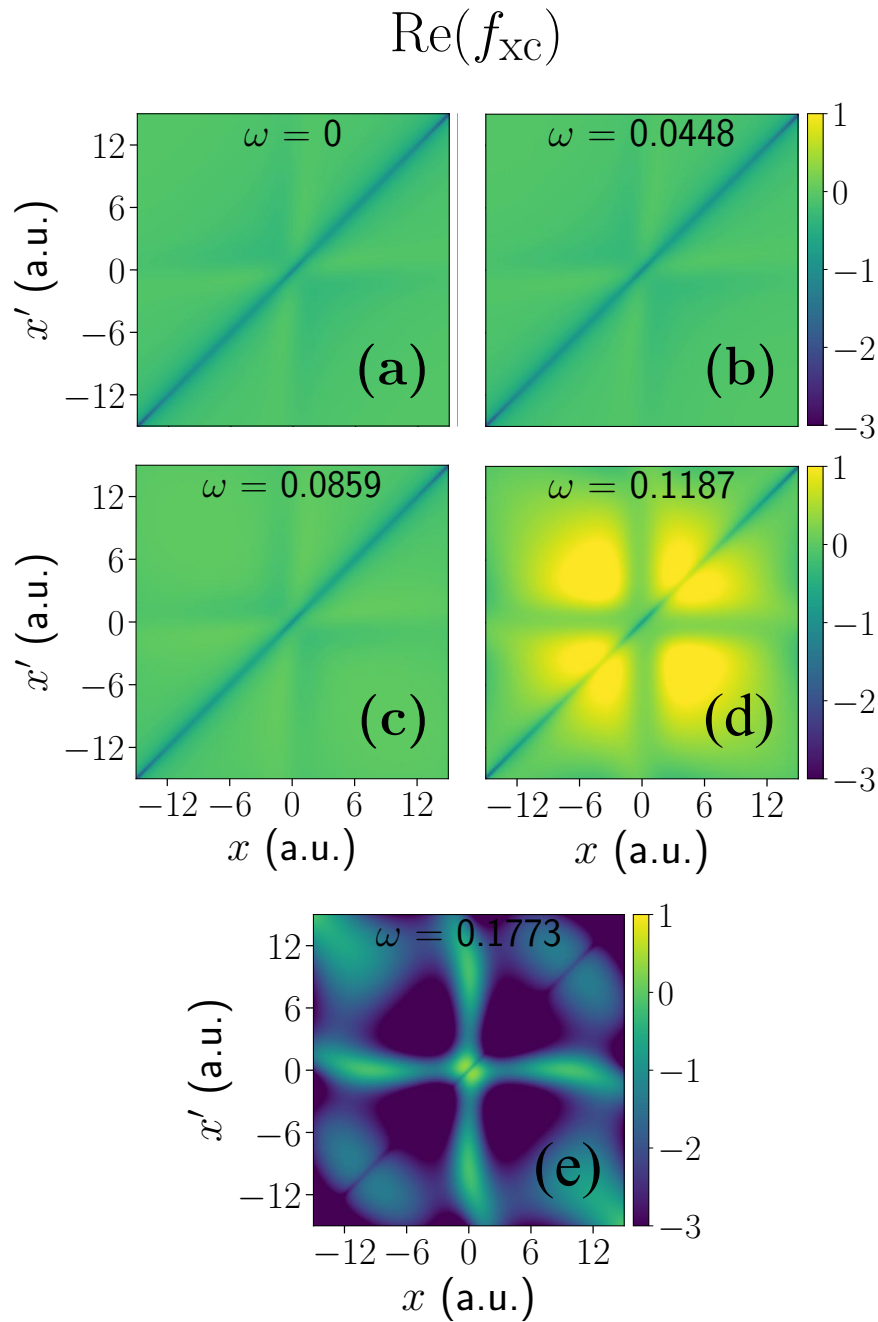
Fig. 6.6. The real part of the exact f_{xc} of the atomic-like system: (a) In the adiabatic limit ($\omega = 0$), (b) at the first excitation ($\omega = 0.0448$), (c) at the second excitation ($\omega = 0.0859$), (d) at the third excitation ($\omega = 0.1187$), and (e) at the sixth excitation ($\omega = 0.1773$). As in the harmonic well system, we find f_{xc} to be nearly ω-independent and exhibit a relatively simple spatial form up to the first excitation. This behaviour persists up to the second excitation, however, more complex spatial structure is needed to capture the third excitation. We find this additional spatial structure and stronger ω-dependence to increase as we progress to higher excitations, as seen at the sixth excitation in (e) (not shown in previous plot of $\sigma(\omega)$: Fig. 6.5(b)).
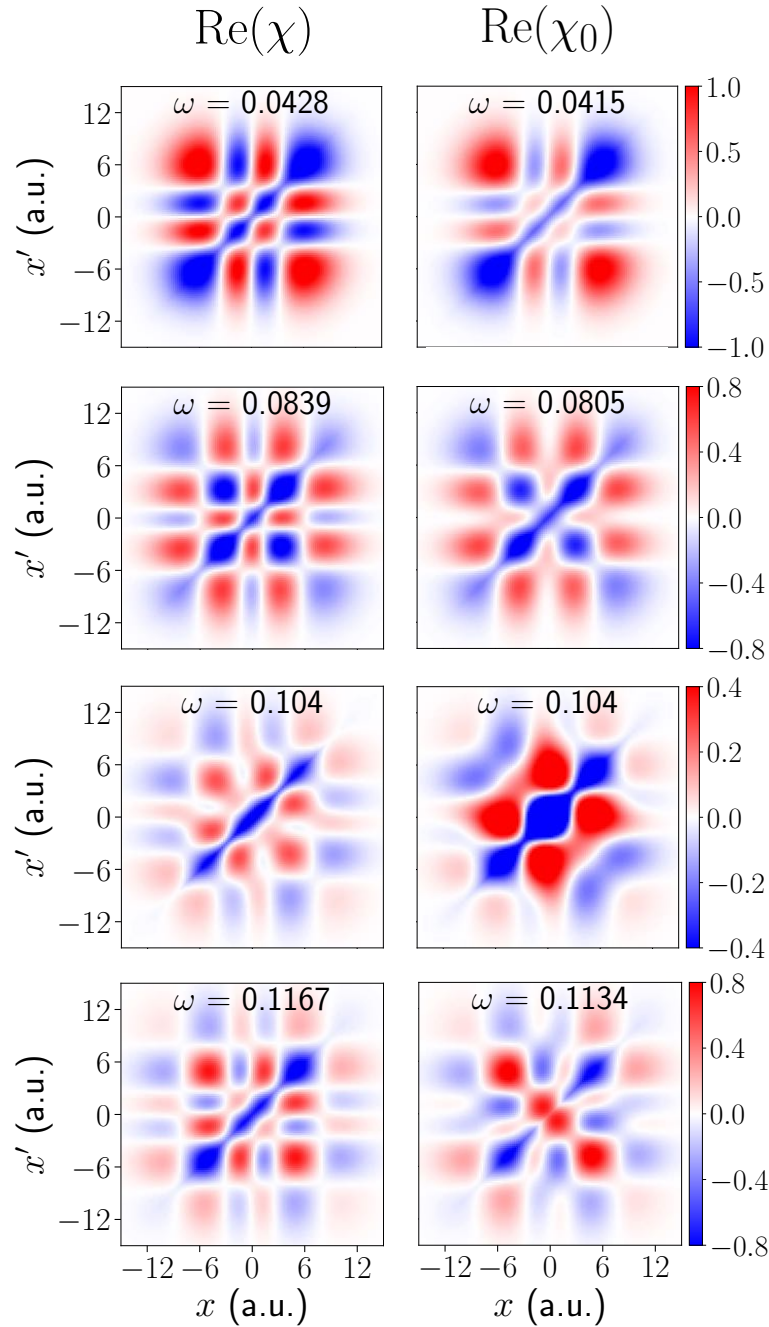
Fig. 6.7. The exact χ and χ_0 in the atomic-like system: Row one: $\text{Re}(\chi)$ and $\text{Re}(\chi_0)$ immediately prior to their first transitions at $\omega = 0.0448$ and 0.0435 (main panel of Fig. 6.5(b)), respectively. Row two: The same but for the second transitions at 0.0859 and 0.0825, respectively, which are suppressed in $\sigma(\omega)$. Row three: $\text{Re}(\chi)$ and $\text{Re}(\chi_0)$ immediately prior to the third KS excitation at 0.1060 (suppressed in $\sigma(\omega)$), which manifests at higher ω in the interacting system. Row four: $\text{Re}(\chi)$ and $\text{Re}(\chi_0)$ immediately prior to their next transitions at 0.1187 (third in the exact) and 0.1154 (fourth in the KS), respectively, which are the next peaks to appear in $\sigma(\omega)$ (inset of Fig. 6.5(b)). As seen in the harmonic well system, $\text{Re}(\chi)$ and $\text{Re}(\chi_0)$ exhibit remarkably similar spatial structure. This becomes less so as we progress to higher transitions, in which both response functions also acquire additional spatial structure.

6.3.4   Performance of approximate kernels

As set out in the introduction to this chapter, we are exploring the properties of exact kernels for model systems, in order to gain insight and to ascertain as to whether f_{xc} is amenable to approximation. To this end, we now investigate the performance of adiabatic kernels as well as local kernels, in the same spirit as most practical approximations.

We begin with the exact adiabatic approach, in which we take the static ($\omega = 0$) limit of the exact f_{xc}, and apply this at all frequencies: we mix $f_{xc}^A(x, x') = f_{xc}(x, x', \omega = 0)$ with the exact $\chi_0(x, x', \omega)$ to obtain some $\chi(x, x', \omega)$, via the Dyson equation. As the exact xc kernel is completely real in the static limit, so too is the exact adiabatic xc kernel. This will help us to determine the importance of not only the ω-dependence of f_{xc}, but also the imaginary component, as any kernel with memory must have an imaginary component (and any adiabatic kernel must be purely real), as a consequence of the known properties of the exact kernel (see Sec. 2.5.3.1).

We begin with the harmonic well system and find that the exact f_{xc}^A does a strikingly good job of describing the first excitation [Fig. 6.8(a)]; see the inset of the figure for a close-up view. It can be seen that the position of the KS peak and the slight discrepancy in its height is almost perfectly corrected by the exact adiabatic kernel. This reflects the remarkably weak ω-dependence of f_{xc}, as analysed in Fig. 6.2.

Moving on to the atomic-like system, we find a very similar result with the first excitation being well described by the exact f_{xc}^A [Fig. 6.8(b)], although the slight error is more noticeable in this system, as can be seen in the top inset of the figure. The bottom inset details the third excitation (the next to appear in $\sigma(\omega)$), which the exact adiabatic kernel is completely incapable of capturing. These results reflect the more complex spatial structure and ω-dependence that manifests in f_{xc} at higher frequencies, as shown in Fig. 6.6. It is clear that memory effects, described through the ω-dependence and imaginary part of the exact f_{xc}, become significant as we move beyond the first excitation (as suggested by our analysis of the simple toy model in Fig. 6.4), revealing the limitations of adiabatic kernels (even the exact adiabatic approach).

We now investigate the extent to which local kernel approximations for f_{xc} may be meaningful. As we have observed f_{xc} to largely cancel with u at low ω, we choose to focus on the Hartree-exchange-correlation kernel $f_{Hxc} = f_{xc} + u$. We find this cancellation results in it being much smaller in magnitude than f_{xc}, as shown in Fig. 6.9 for the atomic-like system. We seek to replicate the effect of the exact $f_{Hxc}(x, x', \omega)$ through a
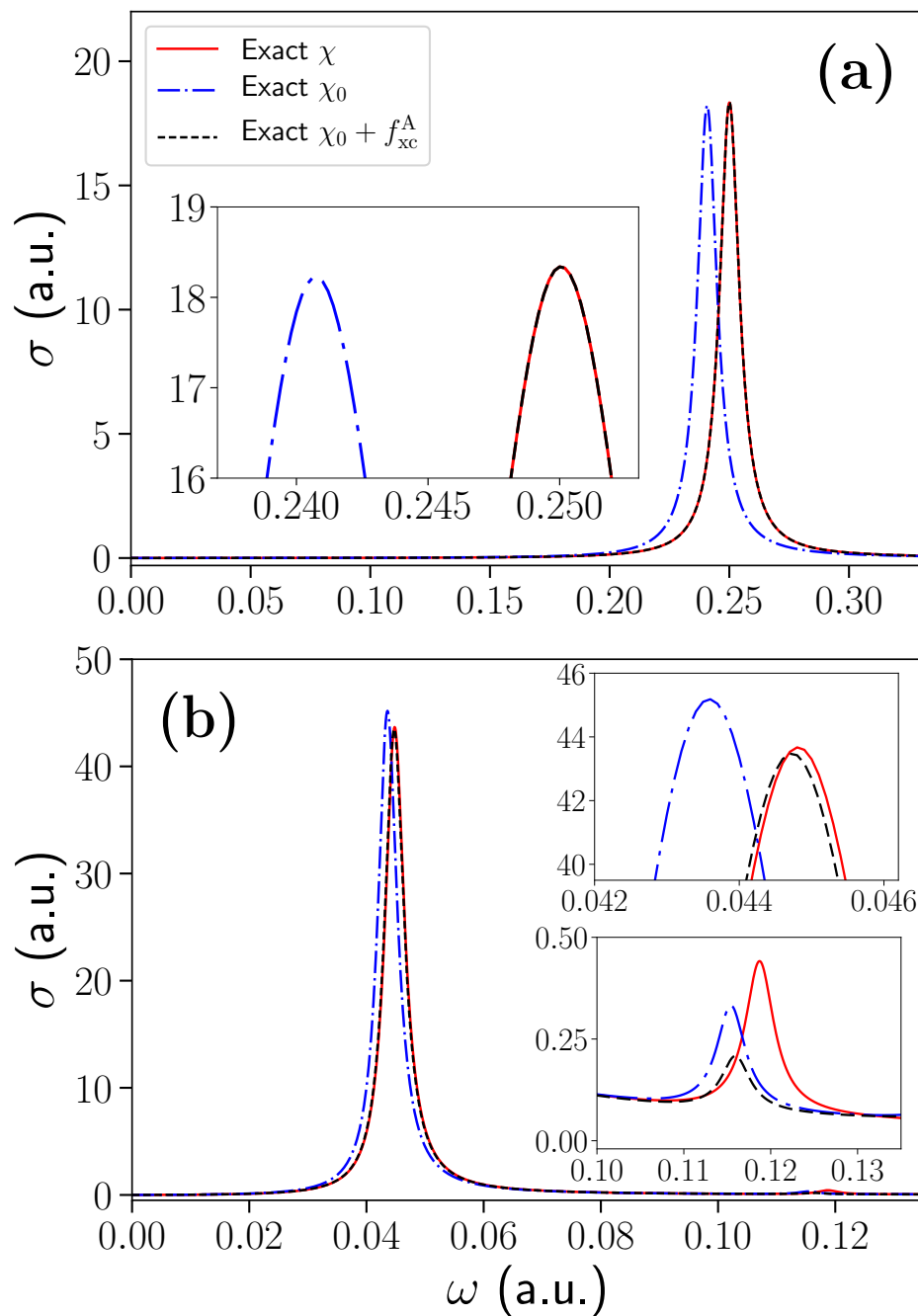
Fig. 6.8. Performance of the exact adiabatic xc kernel f_{xc}^A: (a) In the harmonic well system: the absorption spectra of the exact (solid red) and Kohn-Sham (dotted-dashed blue) systems, along with the exact adiabatic approximation (short-dashed black); the inset shows the peaks in more detail. (b) In the atomic-like system: the same; the top inset and bottom inset show the first and third excitations in more detail, respectively. In both systems f_{xc}^A does a strikingly good job of correcting χ_0 for the first excitation, particularly in the harmonic well system. It is completely inadequate for capturing the third excitation in the atomic-like system, which is not too surprising given the more complex spatial structure and ω-dependence that manifests in the exact f_{xc} at higher frequencies (see Fig. 6.6(d)).

simple local kernel $f_{\text{Hxc}}^{\text{l}}(x, \omega)$:

$$f_{\text{Hxc}}(x, x', \omega) \approx f_{\text{Hxc}}^{\text{l}}(x, \omega)\, \delta(x - x'), \tag{6.7a}$$

$$f_{\text{Hxc}}^{\text{l}}(x, \omega) = \int f_{\text{Hxc}}^{\text{l}}(x, \omega)\, \delta(x - x')\, dx' = \int f_{\text{Hxc}}(x, x', \omega)\, dx'. \tag{6.7b}$$

Here, we are trying to incorporate the non-local parts of f_{Hxc} through some envelope function, with which f_{Hxc} is integrated over x', for each fixed point x along the main diagonal. We assume a simple model for this envelope function – a constant. We find when mixed with the exact χ_0, this local kernel outperforms the RPA and ALDA kernels in regard to the peak position, but fails to correct the peak height and still performs worse than χ_0 alone, for the first excitation. Such a local kernel is completely inadequate to describe the third excitation.
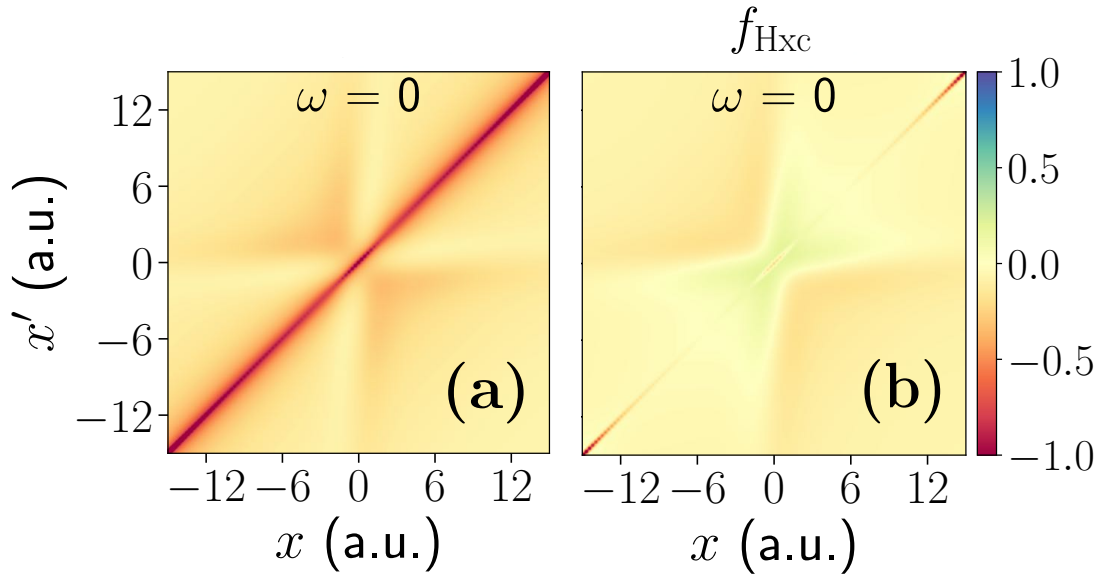
Fig. 6.9. The exact kernels of the atomic-like system at $\omega = 0$: (a) The exchange-correlation kernel f_{xc}, and (b) the Hartree-exchange-correlation kernel $f_{\text{Hxc}} = f_{\text{xc}} + u$. As we observed earlier, f_{xc} largely cancels with u at low ω, leading to f_{Hxc} being much smaller in magnitude.

6.4   Conclusions

In summary, we have calculated the exact $f_{\text{xc}}(x, x', \omega)$ for two prototype systems. At low ω, we find the imaginary component of f_{xc} to be small, with the real part alone sufficient to reproduce the first excitation. Up to and including the first excitation, $\text{Re}(f_{\text{xc}})$ exhibits strikingly weak ω-dependence, stemming from strong, but closely

similar ω-dependence between the interacting and non-interacting density-response functions – boding well for the applicability of adiabatic kernels. Additionally, $\mathrm{Re}(f_{xc})$ here has a rather simple spatial form, which is similar to the negative of the Coulomb interaction u, indicating that approximations to f_{Hxc} may be more appropriate than those for f_{xc} alone. For higher excitations, f_{xc} exhibits both additional spatial structure and stronger ω-dependence, indicating that more sophisticated approximations are needed. Throughout, the absorption spectrum of the exact Kohn-Sham system provides a very good starting point, signifying the crucial importance of an accurate approximation for the ground-state v_{xc}.

As discussed extensively in Sec. 2.6.2, most approximate TDDFT functionals utilise an adiabatic and (semi-) local approach. Our results so far suggest that these types of approximations are not adequate beyond low lying frequencies, thereby demanding improved functionals that account for non-adiabatic effects. While the exact f_{xc} is an enigmatic quantity, we have gained valuable insight into its nature through our analysis of prototype systems and a simple toy model. Further research should allow us to assimilate these insights into the development of more sophisticated approximate kernels, through e.g. current functionals.

CONCLUSIONS

7.1 Discussion of results

In this thesis, we set out to investigate the nature of the exact functionals of time-dependent density functional theory (TDDFT) through the study of prototype electronic systems. To begin our investigations we focused exclusively on ground-state DFT, whose solution forms the initial input into TDDFT calculations, and is therefore of crucial importance. The local density approximation (LDA) is the simplest, and one of the most widely used, approximate density functionals. Typically, LDAs are constructed from the homogeneous electron gas (HEG), and their successes and failures are well known. As an alternative approach, we constructed a set of LDAs from finite systems, and compared them against a suitable HEG-based LDA. We found these finite LDAs to give better densities and energies in exchange-dominated systems than did the HEG LDA. We demonstrated that an LDA constructed from systems of just one electron is possible, and remarkably is the one which most accurately describes the self-interaction correction (SIC) in our test systems — a notable failing of HEG-based LDAs. We ascribe this to the HEG being SIC-free in itself, whereas the xc energy of a one-electron system (from which the one-electron LDA was constructed) consists entirely of SIC. We inferred that this better description of the SIC would lead to a reduced error in the exchange energy. All LDAs performed poorly in systems with stronger correlation, highlighting the limitations of local density functionals.

Following on from this work on ground-state DFT we moved on to explicit time-dependence. Here, most approximate functionals utilise an adiabatic approach, thereby completely neglecting the memory-dependence of the true time-dependent xc functional, severely limiting the applicability of TDDFT to a variety of fields of increasing interest. Adiabatic approaches typically entail combining the time-dependent exter-

nal and Hartree potentials with a ground-state xc potential. In our work, we presented a new perspective on the concept of adiabaticity by applying it to the *complete* time-dependent Kohn-Sham (KS) potential. By rigorously splitting it into its adiabatic and non-adiabatic parts, we proposed a simple geometrical "fluidic" approximation to the latter. We found the fluidic approximation performed well when applied to a variety of test systems — recovering most of the density error attributable to the exact adiabatic approach — even in highly non-adiabatic situations where the dynamic xc effects become very significant. Further research is needed to better elucidate the advantages and disadvantages of this decomposition of the KS potential.

An important class of applications of TDDFT is the wide variety of spectroscopies, such as optical absorption spectra of molecules and solids. Here, the key quantity to approximate is the xc kernel f_{xc}, the functional derivative of the xc potential with respect to the density. Little is known about the nature of the exact f_{xc}, with most approximate functionals being (semi-) local and adiabatic – proving to be inadequate in many regards. With the aim to assist the development of improved approximate kernels, we have calculated the *exact* f_{xc} for a set of prototype systems. We find the imaginary component of the exact f_{xc} to be negligible at low frequencies ω, with the real part exhibiting strikingly weak ω-dependence and rather simple spatial structure, boding well for the applicability of simple, adiabatic kernels to describe the first excitation. Through analysis of the density response functions, and investigation using a simple toy model, we ascribe these results in part to the exact many-electron wavefunction being well approximated by the exact KS wavefunction. For higher excitations, f_{xc} exhibits both additional spatial structure and stronger ω-dependence, indicating that more sophisticated approximations are needed – motivating the development of improved non-adiabatic functionals. A key finding was that the absorption spectrum of the exact Kohn-Sham system provides a very good starting point to the absorption spectrum of the true interacting system, demonstrating the critical importance of using an accurate approximation to the ground-state xc potential.

7.2   Future work

The ground-state xc functional is crucial to the predictive power of TDDFT, even in non-adiabatic applications. This is evident, for example, from the results presented in Chapter 6, in which we conclude that the exact χ_0 (constructed from the exact ground-state xc potential v_{xc}) provides a good starting point to obtain the exact χ.

As discussed extensively throughout this thesis, local density functionals are widely used to approximate v_{xc}. The insight we gained in Chapter 4, from exploring alternative ways to construct these most simple of approximations, provides the rationale to extend this analysis. This may include generating local xc kernels from our set of LDAs and analysing how they, and the HEG-based one, perform in optical spectra calculations. Alternatively, we may progress to more sophisticated functionals, such as the semi-local generalised gradient approximation (GGA), and explore other ways of constructing these. The primary goal of this line of research is to understand whether approximate functionals can be tailored for use in ab initio calculations.

In Chapter 5, we saw that the fluidic approximation provides a very good description of the non-adiabatic part of the time-dependent KS potential, in the test systems studied. Further investigation is warranted to identify the limits of this approximation; we began to identify this, for example, when simulating a quantum tunnelling system. Nevertheless, the positive results obtained so far lead us to believe that this approach may prove to be a new procedure for performing TDDFT calculations[1], with the fluidic approximation providing a basis for more sophisticated approximate functionals. As detailed in the aforementioned chapter, the fluidic approximation assumes that a system remains close to its ground state in the local instantaneous rest frame, and neglects all non-adiabatic effects in this frame. Further research could perhaps focus on quantifying this remaining non-adiabatic contribution to the KS potential, with the aim of incorporating it into a more sophisticated functional.

Chapter 6 provided important insight into the nature of the exact f_{xc}, including the inadequacy of local and adiabatic kernels for anything but the lowest lying excitation. Our next stage of research should prioritise extending this analysis of the exact xc kernel and to understand how we can incorporate the results into developing improved approximate kernels for these first few excitations. While the performance of different local kernels (from our finite LDAs for instance) should be investigated, our results so far highlight the need to go beyond local, and perhaps semi-local approximations for f_{xc}, with the use of current functionals being a potential way forward. We could develop these current functionals through investigating the exact time propagation of prototype systems, e.g. utilising the "slab" systems presented in Chapter 4. Additionally, with the exact f_{xc} to hand, the tensor xc kernel of time-dependent current density

---

[1]As the application of the fluidic approximation in our test systems required knowledge of the exact density, we need to identify the most appropriate implementation in a practical calculation. This forms another line of research.

functional theory (TDCDFT) is readily available for analysis. If we deduce that the non-adiabatic xc effects captured by the fluidic approximation can be isolated, either exactly or approximately, this may prove to be another possible route to constructing current functionals, by e.g. mixing with an adiabatic kernel. Further research should also go beyond single excitations to explore more problematic situations for traditional approximate functionals, e.g. double excitations.

To summarise, we have presented and investigated the performance of a set of local density functionals as an exploration of the merits of developing approximate ground-state functionals from finite systems, in contrast to the usual extended system approach. We have suggested how this exploration may be furthered in future research. We have also introduced a new perspective on how to address the issue of non-adiabaticity in dynamic systems, and presented a simple geometrical approximation, upon which we hope more sophisticated approximations can be developed. Furthermore, we have begun to characterise the properties of the exact xc kernel of TDDFT, allowing us in part to examine the limitations of the typically applied adiabatic and (semi-) local approximations. In all our research we are always being guided by knowledge of the exact functional, including by analysing its properties in a variety of cases. The results and insight that we have obtained so far from the study of prototype systems are encouraging and set the scene for additional lines of research. A key question to answer is to what extent our results from one dimension translate over to three dimensions, which we began to explore in Ref. 121 and found the preliminary results to be positive. Further work is required to deduce what additional effects, if any, need to be incorporated as we transition to more realistic systems. Our aim is to develop improved approximate functionals for use in practical electronic structure calculations. To this end, after further development and testing in prototype systems, we hope to implement them in ab initio codes.

LINEAR RESPONSE THEORY

A.1 The density-response function in the Lehmann representation

A.1.1 The interacting density-response function[1]

The frequency representation of the interacting density-response function is given by

$$\chi(\vec{r}, \vec{r}', \omega) = \lim_{\eta \to 0^+} \sum_n \left[\frac{\langle \Psi_0 | \hat{n}(\vec{r}) | \Psi_n \rangle \langle \Psi_n | \hat{n}(\vec{r}') | \Psi_0 \rangle}{\omega - (E_n - E_0) + i\eta} - \frac{\langle \Psi_0 | \hat{n}(\vec{r}') | \Psi_n \rangle \langle \Psi_n | \hat{n}(\vec{r}) | \Psi_0 \rangle}{\omega + (E_n - E_0) + i\eta} \right],$$
(A.1.1)

where $|\Psi_0\rangle$, E_0, $|\Psi_n\rangle$ and E_n are the ground state and its energy, and the $n-$th excited state and its energy, respectively, $\hat{n}$ is the density operator in the Heisenberg picture, and ω is the frequency of the perturbation. χ has poles when $\omega \to (E_n - E_0)$, which describe the excitation energies of the system. Below we derive Eq. (A.1.1) from time-dependent perturbation theory.

A.1.1.1 Derivation from time-dependent perturbation theory

Eq. (2.4) defines the expectation value of an observable, with a corresponding Hermitian operator, for a system in state Ψ. Consider an observable α, with Hermitian operator $\hat{\alpha}$:

$$\alpha(t) = \langle \Psi(t) | \hat{\alpha} | \Psi(t) \rangle, \tag{A.1.2a}$$

$$\alpha_0 = \langle \Psi_0 | \hat{\alpha} | \Psi_0 \rangle, \tag{A.1.2b}$$

where α_0 is the expectation value of α when the system is initially in the ground state Ψ_0. At $t = 0$, a time-dependent perturbing field $F(t)$ is applied, such that the Hamil-

---

[1] The working below closely follows that presented in Refs 175 and 176.

tonian becomes

$$\hat{H}(t) = \hat{H}_0 + \hat{H}'(t), \tag{A.1.3a}$$

$$\hat{H}'(t) = F(t)\hat{\beta}, \tag{A.1.3b}$$

where $\hat{H}_0$ is the static (ground-state) Hamiltonian and $\hat{\beta}$ is some observable that $F(t)$ couples to. The response of $\hat{\alpha}$ to this perturbation is

$$
\begin{aligned}
\delta\alpha(t) &= \alpha(t) - \alpha_0 \\
&= \alpha_1(t) + \alpha_2(t) + \alpha_3(t) + ... \\
&\approx \alpha_1(t) \\
&= -i \int_0^t dt' \, F(t') \langle \Psi_0 | [\hat{\alpha}(t), \hat{\beta}(t')] | \Psi_0 \rangle.
\end{aligned}
\tag{A.1.4}
$$

Here, we have expanded $\delta\alpha(t)$ in powers of $F(t)$ and then only taken the first-order (linear response) term $\alpha_1(t)$, into consideration, i.e. neglecting higher-order terms, which is valid providing $F(t)$ is weak enough. The last line has been obtained through consideration of the time-evolution operator (see A.1.1.2).

We now define the response function as

$$\chi_{\alpha\beta}(t - t') = -i\theta(t - t')\langle \Psi_0 | [\hat{\alpha}(t - t'), \hat{\beta}] | \Psi_0 \rangle, \tag{A.1.5}$$

where $[\hat{\alpha}(t), \hat{\beta}(t')]$ has been replaced by $[\hat{\alpha}(t - t'), \hat{\beta}]$ as $\hat{H}_0$ is time-independent, and $\theta(t - t')$ is the step function that ensures causality. This means that the linear response can be written as

$$\delta\alpha(t) \approx \alpha_1(t) = \int_{-\infty}^{\infty} dt' \, \chi_{\alpha\beta}(t - t')F(t'), \tag{A.1.6}$$

where we have replaced the lower integration limit 0 by $-\infty$ as $F(t)$ is only non-zero for $t \geq 0$.

In applications of TDDFT we are interested in situations where the the perturbation is a scalar potential $\delta v_{\text{ext}}(\vec{r}, t)$. Here, δv_{ext} couples to the density operator $\hat{n}(\vec{r}) = \sum_i \delta(\vec{r} - \vec{r}_i)$, such that

$$\hat{H}'(t) = \int_{-\infty}^{\infty} d^3 r' \, \delta v_{\text{ext}}(\vec{r}', t)\hat{n}(\vec{r}'). \tag{A.1.7}$$

This means the response function in Eq. (A.1.5) becomes the density-response func-

tion:

$$\chi(\vec{r},\vec{r}',t-t') = -i\theta(t-t')\langle\Psi_0|[\hat{n}(\vec{r},t-t'),\hat{n}(\vec{r}')]|\Psi_0\rangle, \qquad (A.1.8)$$

and the linear response in Eq. (A.1.6) becomes the linear response in the density:

$$\delta n(\vec{r},t) \approx \int_{-\infty}^{\infty} dt' \int_{-\infty}^{\infty} d^3r' \, \chi(\vec{r},\vec{r}',t-t')\delta v_{\text{ext}}(\vec{r}',t'). \qquad (A.1.9)$$

Now, we Fourier transform Eq. (A.1.8) to obtain χ in frequency space:

$$\begin{aligned}
\chi(\vec{r},\vec{r}',\omega) &= -i\int_{-\infty}^{\infty} d\tau \, \theta(\tau)\langle\Psi_0|[\hat{n}(\vec{r},\tau),\hat{n}(\vec{r}')]|\Psi_0\rangle e^{i\omega\tau} \\
&= -i\sum_n \int_{-\infty}^{\infty} d\tau \, \Bigg[\theta(\tau)e^{i\omega\tau}\Big\{\langle\Psi_0|\hat{n}(\vec{r})|\Psi_n\rangle\langle\Psi_n|\hat{n}(\vec{r}')|\Psi_0\rangle e^{-i\omega_n\tau} \\
&\quad - \langle\Psi_0|\hat{n}(\vec{r}')|\Psi_n\rangle\langle\Psi_n|\hat{n}(\vec{r})|\Psi_0\rangle e^{i\omega_n\tau}\Big\}\Bigg],
\end{aligned} \qquad (A.1.10)$$

where $\tau = t - t'$, $\omega_n = E_n - E_0$, and we have used the interaction representation of operators [Eq. (A.1.18)] and the completeness relation $\sum_n |\Psi_n\rangle\langle\Psi_n| = 1$. Finally, it can be proved using contour integration that

$$\theta(\tau) = \lim_{\eta\to 0^+} \frac{i}{2\pi} \int_{-\infty}^{\infty} d\omega' \, \frac{e^{-i\omega'\tau}}{\omega' + i\eta}, \qquad (A.1.11)$$

and so

$$\chi(\vec{r},\vec{r}',\omega) = \lim_{\eta\to 0^+} \sum_n \left[\frac{\langle\Psi_0|\hat{n}(\vec{r})|\Psi_n\rangle\langle\Psi_n|\hat{n}(\vec{r}')|\Psi_0\rangle}{\omega - (E_n - E_0) + i\eta} - \frac{\langle\Psi_0|\hat{n}(\vec{r}')|\Psi_n\rangle\langle\Psi_n|\hat{n}(\vec{r})|\Psi_0\rangle}{\omega + (E_n - E_0) + i\eta}\right].$$
$$(A.1.12)$$

A.1.1.2 The time-evolution operator

The solution to the time-dependent Schrödinger equation [Eq. (2.5)] can be written as

$$\Psi(\{\vec{r}_i\},t) = \hat{U}(t)\Psi_0(\{\vec{r}_i\}), \qquad (A.1.13)$$

where $\hat{U}(t)$ is the time-evolution operator acting on the initial (ground-state) wavefunction Ψ_0. For a general time-dependent Hamiltonian $H(t)$, $\hat{U}(t)$ can be written as

$$\hat{U}(t) = \hat{\mathcal{T}}\exp\left[-i\int_0^t dt' \, \hat{H}(t')\right], \qquad (A.1.14)$$

where $\hat{\mathcal{T}}$ is the time-ordering operator.

We now consider the specific Hamiltonian in Eq. (A.1.3a), where a time-dependent

perturbation is applied at $t = 0$. For convenience, we define

$$\hat{U}(t) = e^{-i\hat{H}_0 t}\hat{U}_1(t). \tag{A.1.15}$$

It can be proven from the TDSE that

$$i\frac{\partial}{\partial t}\hat{U}_1(t) = e^{i\hat{H}_0 t}\hat{H}'(t)e^{-i\hat{H}_0 t}\hat{U}_1(t), \tag{A.1.16}$$

with initial condition $\hat{U}_1(t\!=\!0) = 1$, so that $\hat{U}(t\!=\!0) = \hat{U}_1(t\!=\!0)$ and $\Psi(\{\vec{r}_i\}, t\!=\!0) = \Psi_0(\{\vec{r}_i\})$. Substituting this initial condition into the RHS of the above equation and integrating over time leads to the following (first-order) approximation:

$$\hat{U}_1(t) \approx 1 - i\int_0^t dt'\, e^{i\hat{H}_0 t'}\hat{H}'(t')e^{-i\hat{H}_0 t'}. \tag{A.1.17}$$

The time-dependent perturbation takes the form $\hat{H}'(t) = F(t)\hat{\beta}$ [Eq. (A.1.3b)], and the observable $\hat{\beta}$ can be written as

$$\hat{\beta}(\tilde{t}) = e^{i\hat{H}_0 \tilde{t}}\hat{\beta}e^{-i\hat{H}_0 \tilde{t}}. \tag{A.1.18}$$

Finally, this leads to the first-order approximation to the full time-evolution operator:

$$\hat{U}(t) \approx e^{-i\hat{H}_0 t}\left(1 - i\int_0^t dt'\, F(t')\hat{\beta}(t')\right). \tag{A.1.19}$$

A.1.2 Non-interacting systems

The frequency representation of the non-interacting density-response function is given by

$$\chi_0(\vec{r}, \vec{r}', \omega) = \lim_{\eta \to 0^+}\sum_{i,j}(f_i - f_j)\frac{\phi_i^*(\vec{r})\phi_j(\vec{r})\phi_j^*(\vec{r}')\phi_i(\vec{r}')}{\omega - (\varepsilon_j - \varepsilon_i) + i\eta}, \tag{A.1.20}$$

where the ϕ_i, ε_i are the exact solutions to the Kohn-Sham equations of ground-state DFT, and f_i is the Fermi occupation (0 or 1) of ϕ_i. In a manner analogous to χ, which has poles at the excitation energies of the interacting system, χ_0 has poles at the excitation energies of the Kohn-Sham system, $\varepsilon_j - \varepsilon_i$. Below, by considering the expression for χ [Eq. (A.1.1)], we derive Eq. (A.1.20) for a system of two non-interacting electrons. This is generalisable to a system of N electrons.

The ground-state wavefunction of a system of two non-interacting electrons is a single Slater determinant of the lowest (occupied) single-particle orbitals:

$$\Psi_0(\vec{r}_1, \vec{r}_2) = \frac{1}{\sqrt{2}} \begin{vmatrix} \phi_1(\vec{r}_1) & \phi_2(\vec{r}_1) \\ \phi_1(\vec{r}_2) & \phi_2(\vec{r}_2) \end{vmatrix} = \frac{1}{\sqrt{2}} \left[\phi_1(\vec{r}_1)\phi_2(\vec{r}_2) - \phi_2(\vec{r}_1)\phi_1(\vec{r}_2) \right]. \qquad \text{(A.1.21)}$$

If either electron (or both) is promoted to a higher-energy orbital, this represents an excited state:

$$\Psi_n(\vec{r}_1, \vec{r}_2) = \frac{1}{\sqrt{2}} \begin{vmatrix} \phi_\mu(\vec{r}_1) & \phi_\nu(\vec{r}_1) \\ \phi_\mu(\vec{r}_2) & \phi_\nu(\vec{r}_2) \end{vmatrix} = \frac{1}{\sqrt{2}} \left[\phi_\mu(\vec{r}_1)\phi_\nu(\vec{r}_2) - \phi_\nu(\vec{r}_1)\phi_\mu(\vec{r}_2) \right]. \qquad \text{(A.1.22)}$$

Substituting the above expressions, along with the density operator $\hat{n}(\vec{r}) = \sum_i \delta(\vec{r} - \vec{r}_i)$, into the amplitudes in Eq. (A.1.1):

$$\langle \Psi_0 | \hat{n}(\vec{r}) | \Psi_n \rangle = \frac{1}{2} \int d^3 r_1 \int d^3 r_2 \left[\phi_1^*(\vec{r}_1)\phi_2^*(\vec{r}_2) - \phi_2^*(\vec{r}_1)\phi_1^*(\vec{r}_2) \right] \left[\delta(\vec{r} - \vec{r}_1) + \delta(\vec{r} - \vec{r}_2) \right] \times$$
$$\left[\phi_\mu(\vec{r}_1)\phi_\nu(\vec{r}_2) - \phi_\nu(\vec{r}_1)\phi_\mu(\vec{r}_2) \right]$$

$$= \frac{1}{2} \int d^3 r_1 \int d^3 r_2 \left[\delta(\vec{r} - \vec{r}_1) + \delta(\vec{r} - \vec{r}_2) \right] \left[\phi_1^*(\vec{r}_1)\phi_2^*(\vec{r}_2)\phi_\mu(\vec{r}_1)\phi_\nu(\vec{r}_2) - \right.$$
$$\phi_1^*(\vec{r}_1)\phi_2^*(\vec{r}_2)\phi_\nu(\vec{r}_1)\phi_\mu(\vec{r}_2) - \phi_2^*(\vec{r}_1)\phi_1^*(\vec{r}_2)\phi_\mu(\vec{r}_1)\phi_\nu(\vec{r}_2) +$$
$$\left. \phi_2^*(\vec{r}_1)\phi_1^*(\vec{r}_2)\phi_\nu(\vec{r}_1)\phi_\mu(\vec{r}_2) \right]$$

$$= \frac{1}{2} \int d^3 r_1 \left[\phi_1^*(\vec{r}_1)\phi_2^*(\vec{r})\phi_\mu(\vec{r}_1)\phi_\nu(\vec{r}) - \phi_1^*(\vec{r}_1)\phi_2^*(\vec{r})\phi_\nu(\vec{r}_1)\phi_\mu(\vec{r}) - \right.$$
$$\left. \phi_2^*(\vec{r}_1)\phi_1^*(\vec{r})\phi_\mu(\vec{r}_1)\phi_\nu(\vec{r}) + \phi_2^*(\vec{r}_1)\phi_1^*(\vec{r})\phi_\nu(\vec{r}_1)\phi_\mu(\vec{r}) \right]$$
$$+ \frac{1}{2} \int d^3 r_2 \left[\phi_1^*(\vec{r})\phi_2^*(\vec{r}_2)\phi_\mu(\vec{r})\phi_\nu(\vec{r}_2) - \phi_1^*(\vec{r})\phi_2^*(\vec{r}_2)\phi_\nu(\vec{r})\phi_\mu(\vec{r}_2) - \right.$$
$$\left. \phi_2^*(\vec{r})\phi_1^*(\vec{r}_2)\phi_\mu(\vec{r})\phi_\nu(\vec{r}_2) + \phi_2^*(\vec{r})\phi_1^*(\vec{r}_2)\phi_\nu(\vec{r})\phi_\mu(\vec{r}_2) \right]$$

$$= \frac{1}{2} \left[\phi_2^*(\vec{r})\phi_\nu(\vec{r})\delta_{1\mu} - \phi_2^*(\vec{r})\phi_\mu(\vec{r})\delta_{1\nu} - \phi_1^*(\vec{r})\phi_\nu(\vec{r})\delta_{2\mu} + \phi_1^*(\vec{r})\phi_\mu(\vec{r})\delta_{2\nu} \right]$$
$$+ \frac{1}{2} \left[\phi_1^*(\vec{r})\phi_\mu(\vec{r})\delta_{2\nu} - \phi_1^*(\vec{r})\phi_\nu(\vec{r})\delta_{2\mu} - \phi_2^*(\vec{r})\phi_\mu(\vec{r})\delta_{1\nu} + \phi_2^*(\vec{r})\phi_\nu(\vec{r})\delta_{1\mu} \right]$$

$$= \phi_2^*(\vec{r})\phi_\nu(\vec{r})\delta_{1\mu} + \phi_1^*(\vec{r})\phi_\mu(\vec{r})\delta_{2\nu},$$

$$\text{(A.1.23)}$$

where the last line has used $\delta_{1\nu} = \delta_{2\mu} = 0$ as both electrons cannot occupy the same single-particle state.

Similarly:

$$\langle \Psi_n | \hat{n}(\vec{r}') | \Psi_0 \rangle = \phi_2(\vec{r}')\phi_\nu^*(\vec{r}')\delta_{1\mu} + \phi_1(\vec{r}')\phi_\mu^*(\vec{r}')\delta_{2\nu}, \tag{A.1.24}$$

$$\langle \Psi_0 | \hat{n}(\vec{r}') | \Psi_n \rangle = \phi_2^*(\vec{r}')\phi_\nu(\vec{r}')\delta_{1\mu} + \phi_1^*(\vec{r}')\phi_\mu(\vec{r}')\delta_{2\nu}, \tag{A.1.25}$$

$$\langle \Psi_n | \hat{n}(\vec{r}) | \Psi_0 \rangle = \phi_2(\vec{r})\phi_\nu^*(\vec{r})\delta_{1\mu} + \phi_1(\vec{r})\phi_\mu^*(\vec{r})\delta_{2\nu}. \tag{A.1.26}$$

Substituting these amplitudes into the expression for χ to obtain χ_0:

$$\chi_0(\vec{r}, \vec{r}', \omega) = \lim_{\eta \to 0^+} \sum_n \left[\frac{\langle \Psi_0 | \hat{n}(\vec{r}) | \Psi_n \rangle \langle \Psi_n | \hat{n}(\vec{r}') | \Psi_0 \rangle}{\omega - (E_n - E_0) + i\eta} - \frac{\langle \Psi_0 | \hat{n}(\vec{r}') | \Psi_n \rangle \langle \Psi_n | \hat{n}(\vec{r}) | \Psi_0 \rangle}{\omega + (E_n - E_0) + i\eta} \right]$$

$$= \lim_{\eta \to 0^+} \sum_{\mu,\nu \in \text{unocc}} \left[\frac{\phi_2^*(\vec{r})\phi_\nu(\vec{r})\phi_2(\vec{r}')\phi_\nu^*(\vec{r}')\delta_{1\mu} + \phi_1^*(\vec{r})\phi_\mu(\vec{r})\phi_1(\vec{r}')\phi_\mu^*(\vec{r}')\delta_{2\nu}}{\omega - (E_{\mu\nu} - E_0) + i\eta} - \right.$$

$$\left. \frac{\phi_2^*(\vec{r}')\phi_\nu(\vec{r}')\phi_2(\vec{r})\phi_\nu^*(\vec{r})\delta_{1\mu} + \phi_1^*(\vec{r}')\phi_\mu(\vec{r}')\phi_1(\vec{r})\phi_\mu^*(\vec{r})\delta_{2\nu}}{\omega + (E_{\mu\nu} - E_0) + i\eta} \right], \tag{A.1.27}$$

where we have ignored the $\delta_{1\mu}\delta_{2\nu}$ cross-terms as these must be zero, and used $E_{\mu\nu}$ to denote the energy of an excited state. It is clear from the above equation that all double excitations ($\delta_{1\mu} = \delta_{2\nu} = 0$) are absent from χ_0 and only the single-particle excitations are captured. Simplifying:

$$\chi_0(\vec{r}, \vec{r}', \omega) = \lim_{\eta \to 0^+} \sum_{i \in \text{occ}} \sum_{j \in \text{unocc}} \left[\frac{\phi_i^*(\vec{r})\phi_j(\vec{r})\phi_j^*(\vec{r}')\phi_i(\vec{r}')}{\omega - (\varepsilon_j - \varepsilon_i) + i\eta} - \frac{\phi_i^*(\vec{r}')\phi_j(\vec{r}')\phi_j^*(\vec{r})\phi_i(\vec{r})}{\omega + (\varepsilon_j - \varepsilon_i) + i\eta} \right], \tag{A.1.28}$$

where we have noted that for each excitation ($i \to j$), the excitation energy will be equal to the difference between the KS eigenvalues. We can rewrite the above expression to obtain Eq. (A.1.20):

$$\chi_0(\vec{r}, \vec{r}', \omega) = \lim_{\eta \to 0^+} \sum_{i,j} (f_i - f_j) \frac{\phi_i^*(\vec{r})\phi_j(\vec{r})\phi_j^*(\vec{r}')\phi_i(\vec{r}')}{\omega - (\varepsilon_j - \varepsilon_i) + i\eta}. \tag{A.1.29}$$

This expression is equivalent [177] to that derived by Adler [178] and Wiser [179] for a periodic system in reciprocal space.

A.2 Optical absorption spectrum from the density-response function

A quantity of interest in spectroscopy is the photoabsorption cross-section $\sigma(\omega)$, otherwise known as the absorption spectrum, which provides a measure of how much of the incident radiation is absorbed by the system, and can be calculated from the imaginary part of the density-response function:

$$\sigma(\omega) = -\frac{4\pi\omega}{c} \int dx \int dx' \, \mathrm{Im}\big[\chi(x, x', \omega)\big] \, x \, x', \qquad (A.2.30)$$

where c is the speed of light and we have restricted ourselves to 1D.

Below we derive Eq. (A.2.30) from first principles.

A.2.1 Derivation from semi-classical physics

Consider a uniform electric field oscillating with time t at frequency ω:

$$E(t) = \mathcal{E} \cos(\omega t), \qquad (A.2.31)$$

where $\mathcal{E}$ is polarised along the x-axis. This represents the long-wavelength limit of a linearly polarised electromagnetic wave, where the magnetic field component is weak enough to be neglected. Some of this energy will be absorbed by the system and is quantified by $\sigma(\omega)$. This absorption cross-section can be imagined as a "disc" that absorbs all energy incident upon it. When multiplied by the intensity of the light I, it gives the total power absorbed by the system ($P = I\sigma$).

We begin with electromagnetic theory, specifically the Poynting vector, which describes the directional energy flux (rate of energy transport per unit area) of an electromagnetic field. For a monochromatic linearly polarised electromagnetic wave in empty space, such as the one in Eq. (A.2.31), the Poynting vector points in the direction of propagation and is given by

$$\vec{S} = \frac{1}{\mu_0}\vec{E} \times \vec{B}, \qquad (A.2.32a)$$

$$S = \frac{1}{\mu_0}EB, \qquad (A.2.32b)$$

where S is the magnitude of the Poynting vector and reduces to this simple form due to the electric field $\vec{E}$ and magnetic field $\vec{B}$ being perpendicular to one another.

For a plane wave, Maxwell's equations enforce the relationship between the strength of $\vec{E}$ and $\vec{B}$, $c = E/B$, where c is the speed of light in empty space. This allows the Poynting vector in Eq. (A.2.32b) to be written in terms of the electric field:

$$S = \frac{1}{\mu_0}\frac{1}{c}E^2 = \varepsilon_0 c E^2, \tag{A.2.33}$$

where the relationship $c = 1/\sqrt{\mu_0 \varepsilon_0}$ has been used. Substituting the magnitude of the electric field in Eq. (A.2.31) into Eq. (A.2.33):

$$S = \varepsilon_0 c \mathcal{E}^2 \cos^2(\omega t). \tag{A.2.34}$$

It can be seen from this equation that the Poynting vector fluctuates over one complete cycle. To get the *cycled-averaged* intensity of the incident wave, we need to average Eq. (A.2.34) over all cycles:

$$I = \langle S \rangle = \varepsilon_0 c \mathcal{E}^2 \langle \cos^2(\omega t) \rangle = \frac{1}{2}\varepsilon_0 c \mathcal{E}^2, \tag{A.2.35}$$

where we have used the well known expectation value $\langle \cos^2(\omega t) \rangle = \frac{1}{2}$.

Now that we have determined an expression for the intensity of the incident light, we need to determine an expression for the power that is absorbed by the system. To do so, it is helpful to recast the incident EM wave in complex exponential form:

$$E(t) = \mathcal{E}e^{-i\omega t}, \tag{A.2.36}$$

where the real part of this represents the true physical wave. After enough time has elapsed, such that the system has reached a steady-state, the time-dependent electron density is described by the sum of the ground-state density and a small induced (complex) density response δn, oscillating with frequency ω:

$$n(x,t) = n_{\text{gs}}(x) + \delta n(x)e^{-i\omega t}. \tag{A.2.37}$$

As a result, the time-dependent electron current density also oscillates with frequency ω:

$$j(x,t) = j_0(x)e^{-i\omega t}, \tag{A.2.38}$$

where again the real parts in both equations represent the true physical quantities.

We consider the (real) force on an infinitesimal element dq at position x:

$$dF = E \, dq = \mathcal{E} \cos(\omega t) \times (-e) \times n(x,t) \, dx, \tag{A.2.39}$$

where $-e$ is the electronic charge. By multiplying by the group velocity $u = j/n$ and integrating over space we find the total power absorbed by the system:

$$
\begin{aligned}
P &= \int dF \, u \\
&= -e \, \mathcal{E} \cos(\omega t) \int \text{Re}\big[j(x,t)\big] \, dx \\
&= -e \, \mathcal{E} \cos(\omega t) \int \text{Re}\big[j_0(x) e^{-i\omega t}\big] \, dx \\
&= -\frac{1}{2} e\mathcal{E} \int j_1(x) \, dx, \tag{A.2.40}
\end{aligned}
$$

where we have taken the real component of j, like we did with F, as we are multiplying two oscillating quantities together. The last line has rewritten the complex exponential through Euler's formula, denoted the real part of j_0 as j_1, and used the expectation values $\langle \cos^2(\omega t) \rangle = \frac{1}{2}$ and $\langle \cos(\omega t)\sin(\omega t) \rangle = 0$ to obtain the cycled-average power absorbed. Evaluating the integral using integration by parts:

$$
\begin{aligned}
\int_{-\infty}^{\infty} j_1(x) \, dx &= \int_{-\infty}^{\infty} j_1(x) \times 1 \, dx \\
&= \Big[j_1(x) x \Big]_{-\infty}^{\infty} - \int_{-\infty}^{\infty} \frac{dj_1}{dx} x \, dx \\
&= 0 - \int_{-\infty}^{\infty} -\omega \, \text{Im}\big[\delta n(x)\big] x \, dx \\
&= \omega \int_{-\infty}^{\infty} \text{Im}\big[\delta n(x)\big] x \, dx, \tag{A.2.41}
\end{aligned}
$$

where the third line has substituted Eq. (A.2.37) and Eq. (A.2.38) into the continuity equation ($\partial n/\partial t + \partial j/\partial x = 0$) to rewrite the integrand in terms of δn. This allows us to rewrite P in Eq. (A.2.40) in terms of the induced change in the density:

$$P = -\frac{1}{2} e \, \mathcal{E}\omega \int \text{Im}\big[\delta n(x)\big] x \, dx. \tag{A.2.42}$$

Now, linear response theory tells us that a weak external perturbation $\delta v_{\text{ext}}(x,\omega)$ will induce a density response that is linearly related to the density-response function:

$$\delta n(x,\omega) = \int \chi(x,x',\omega) \, \delta v_{\text{ext}}(x',\omega) \, dx'. \tag{A.2.43}$$

For a uniform electric field polarised along the x-axis, $\delta v_{\text{ext}}(x, \omega) = e\, \mathcal{E} x$. Substituting this into Eq. (A.2.43) to obtain $\delta n(x, \omega)$:

$$\begin{aligned}
\delta n(x, \omega) &= \int \chi(x, x', \omega)\, \delta v_{\text{ext}}(x', \omega)\, dx' \\
&= e\, \mathcal{E} \int \chi(x, x', \omega)\, x'\, dx'.
\end{aligned} \tag{A.2.44}$$

Finally, substituting this expression into Eq. (A.2.42) leads to an expression for the power absorbed by the system in terms of the density-response function:

$$P = -\frac{1}{2} e^2 \mathcal{E}^2 \omega \int dx \int dx'\ \text{Im}\left[\chi(x, x', \omega)\right] x\, x'. \tag{A.2.45}$$

We obtain the absorption cross-section σ through the ratio of the net power absorbed P to the intensity I [Eq. (A.2.35)]:

$$\begin{aligned}
\sigma(\omega) &= \left[-\frac{1}{2} e^2 \mathcal{E}^2 \omega \int dx \int dx'\ \text{Im}\left[\chi(x, x', \omega)\right] x\, x' \right] \times \left[\frac{2}{\varepsilon_0 c \mathcal{E}^2} \right] \\
&= -\frac{e^2 \omega}{\varepsilon_0 c} \int dx \int dx'\ \text{Im}\left[\chi(x, x', \omega)\right] x\, x'.
\end{aligned} \tag{A.2.46}$$

Finally, switching to Hartree atomic units ($m_e = e = \hbar = 1/4\pi\varepsilon_0 = 1$):

$$\sigma(\omega) = -\frac{4\pi\omega}{c} \int dx \int dx'\ \text{Im}\left[\chi(x, x', \omega)\right] x\, x'. \tag{A.2.47}$$

A.2.2   Derivation from time-dependent perturbation theory

Now that we have derived Eq. (A.2.30) through a semi-classical approach we wish to do so through a full quantum description. First, it is necessary to obtain the RHS of Eq. (A.2.30) (ignoring the prefactor) explicitly in terms of the many-electron eigenstates $\{\Psi_m\}$, as we shall determine an expression for $\sigma(\omega)$ in terms of $\{\Psi_m\}$, and then equate the two sides. By making use of the following identity:

$$\lim_{b \to 0^+} \frac{1}{a + ib} = \mathcal{P}\left(\frac{1}{a}\right) - i\pi\delta(a), \tag{A.2.48}$$

for two real numbers a and b, we obtain the imaginary part of χ [Eq. (A.1.1)]:

$$\begin{aligned}
\text{Im}\left[\chi(x, x', \omega)\right] = \pi \sum_n \Big[&- \langle \Psi_0 | \hat{n}(x) | \Psi_n \rangle \langle \Psi_n | \hat{n}(x') | \Psi_0 \rangle\, \delta(\omega - (E_n - E_0)) \\
&+ \langle \Psi_0 | \hat{n}(x') | \Psi_n \rangle \langle \Psi_n | \hat{n}(x) | \Psi_0 \rangle\, \delta(\omega + (E_n - E_0)) \Big],
\end{aligned} \tag{A.2.49}$$

and then:

$$
\int dx \int dx' \, \mathrm{Im}\big[\chi(x,x',\omega)\big] \, x \, x' = \pi \int dx \int dx' \, \Big[x \, x' \sum_n - \langle \Psi_0 | \hat{n}(x) | \Psi_n \rangle \langle \Psi_n | \hat{n}(x') | \Psi_0 \rangle
$$
$$
\times \, \delta(\omega - (E_n - E_0)) + \langle \Psi_0 | \hat{n}(x') | \Psi_n \rangle \langle \Psi_n | \hat{n}(x) | \Psi_0 \rangle
$$
$$
\times \, \delta(\omega + (E_n - E_0)) \Big].
$$

$$(A.2.50)$$

A.2.2.1   Fermi's golden rule

Now, we consider situations where a time-dependent perturbation is applied at $t = 0$, such that the Hamiltonian of the system becomes

$$
\hat{H}(t) = \hat{H}_0 + \hat{H}'(t), \tag{A.2.51}
$$

where $\hat{H}_0$ is the static (ground-state) Hamiltonian.

The time-dependent wavefunction can be expressed in terms of the many-electron eigenstates of the unperturbed system as they form a complete set:

$$
\Psi(t) = \sum_m c_m \Psi_m e^{-iE_m t}, \tag{A.2.52}
$$

where $\{c_m\}$ are the expansion coefficients and E_m is the energy eigenvalue associated with Ψ_m. By substituting these equations into the TDSE [Eq. (2.5)] we obtain

$$
\hat{H}\Psi = \sum_m c_m \hat{H}_0 \Psi_m e^{-iE_m t} + \sum_m c_m \hat{H}' \Psi_m e^{-iE_m t}, \tag{A.2.53a}
$$
$$
i\frac{\partial \Psi}{\partial t} = i \sum_m \Big[\dot{c}_m(t) \Psi_m e^{-iE_m t} - iE_m c_m(t) \Psi_m e^{-iE_m t} \Big]. \tag{A.2.53b}
$$

By equating both of these and after some manipulation:

$$
i \sum_m \dot{c}_m(t) e^{-iE_m t} \langle \Psi_n | \Psi_m \rangle = \sum_m c_m(t) e^{-iE_m t} \langle \Psi_n | \hat{H}' | \Psi_m \rangle. \tag{A.2.54}
$$

The eigenstates are orthonormal, $\langle \Psi_n | \Psi_m \rangle = \delta_{nm}$, and so

$$
i\dot{c}_n(t) e^{-iE_n t} = \sum_m c_m(t) e^{-iE_m t} H'_{nm}, \tag{A.2.55}
$$

where H'_{nm} is a matrix element. We find

$$\dot{c}_n(t) = \frac{1}{i}\sum_m c_m(t)e^{-i(E_m-E_n)t}H'_{nm}. \tag{A.2.56}$$

Now, if $\hat{H}'$ is much smaller than $\hat{H}_0$, then $\{c_m\}$ are slowly varying with t. As the system is initially in the ground state, $c_0 = 1$, with the rest equal to zero. Substituting these initial conditions into the RHS of the above equation leads to the first-order approximation:

$$\dot{c}_n(t) \approx \frac{1}{i}\sum_m \delta_{0m}e^{-i\omega_{mn}t}H'_{nm} = \frac{1}{i}e^{-i\omega_{0n}t}H'_{n0}, \tag{A.2.57}$$

where we have defined the transition energy $\omega_{mn} = E_m - E_n$. Therefore

$$c_n(t) \approx \frac{1}{i}\int_0^t dt'\, H'_{n0}(t')e^{-i\omega_{0n}t'}. \tag{A.2.58}$$

Now, we consider the system under the influence of the electric field in Eq. (A.2.31), such that

$$\hat{H}' = \sum_i \delta v(x_i)\cos(\omega t), \tag{A.2.59}$$

where $\delta v(x) = e\mathcal{E}x$. Substituting the above into Eq. (A.2.58), and using the identity $\cos(\omega t) = (e^{i\omega t} + e^{-i\omega t})/2$:

$$\begin{aligned}
c_n(t) &= \frac{1}{2i}\int_0^t dt'\, \delta v_{n0}\left[e^{-i(\omega_{0n}-\omega)t'} + e^{-i(\omega_{0n}+\omega)t'}\right]\\
&= \frac{\delta v_{n0}}{2}\left[\frac{e^{-i(\omega_{0n}-\omega)t}-1}{\omega_{0n}-\omega} + \frac{e^{-i(\omega_{0n}+\omega)t}-1}{\omega_{0n}+\omega}\right]\\
&= \frac{\delta v_{n0}}{2}\left[\frac{e^{i(\omega_{n0}-\omega)t}-1}{\omega-\omega_{n0}} - \frac{e^{i(\omega+\omega_{n0})t}-1}{\omega+\omega_{n0}}\right],
\end{aligned} \tag{A.2.60}$$

where δv_{n0} is a matrix element, defined below in Eq. (A.2.67). The first term in the square brackets is much larger than the second term when $\omega \approx \omega_{n0}$, i.e. at the transition energy, representing absorption. Considering only this term for now, and using $|e^{i\theta} - 1|^2 = 4\sin^2(\theta/2)$:

$$|c_n(t)|^2 \approx \frac{\delta v_{n0}t^2}{4}\text{sinc}^2\left[\frac{(\omega_{n0}-\omega)t}{2}\right]. \tag{A.2.61}$$

By using the identity

$$\delta(x) = \lim_{\varepsilon\to 0}\frac{1}{\varepsilon}\frac{\text{sinc}(\frac{x}{\varepsilon})}{\pi} \implies 2\pi\delta(x) = \lim_{t\to\infty} t\,\text{sinc}\left(\frac{xt}{2}\right), \tag{A.2.62}$$

we obtain the long-time limit:

$$
\begin{aligned}
|c_n(t)|^2 &\approx \frac{|\delta v_{n0}|^2 \pi t}{2} \delta(\omega_{n0} - \omega) \\
&= \frac{|\delta v_{n0}|^2 \pi t}{2} \delta(\omega - (E_n - E_0)).
\end{aligned} \tag{A.2.63}
$$

If we were to take the second term into consideration, an additional delta function $\delta(\omega + (E_n - E_0))$ would appear, representing stimulated emission. As the system begins in the ground state only absorption is possible, and so we can neglect this additional term. The above allows us to calculate the transition rate between the ground state and the $n-$th excited state:

$$
\Gamma_{0 \longrightarrow n} = \frac{|c_n(t)|^2}{t} = \frac{|\delta v_{n0}|^2 \pi}{2} \delta(\omega - (E_n - E_0)), \tag{A.2.64}
$$

which is constant in time and is known as Fermi's golden rule. The power (energy per unit time) absorbed will be equal to the transition rate multiplied by the transition energy. The total power absorbed by the system will be a sum over all states:

$$
\begin{aligned}
P &= \sum_n \omega_{n0} \Gamma_{0 \longrightarrow n} = \sum_n \left[\frac{\omega_{n0} |\delta v_{n0}|^2 \pi}{2} \delta(\omega - (E_n - E_0)) \right] \\
&= \omega \sum_n \left[\frac{|\delta v_{n0}|^2 \pi}{2} \delta(\omega - (E_n - E_0)) \right],
\end{aligned} \tag{A.2.65}
$$

where we have replaced ω_{n0} with ω as the delta function enforces this equality.

We can rewrite the spatial part of the perturbing Hamiltonian in terms of the density operator:

$$
\begin{aligned}
\sum_i \delta v(x_i) &= \int dx \sum_i \delta(x - x_i) \, \delta v(x) \\
&= e\mathcal{E} \int dx \, \hat{n}(x)x,
\end{aligned} \tag{A.2.66}
$$

which allows us to define the matrix element

$$
\begin{aligned}
\delta v_{n0} &= \langle \Psi_n | \left\{ \sum_i \delta v(x_i) \right\} | \Psi_0 \rangle \\
&= e\mathcal{E} \langle \Psi_n | \left\{ \int dx \, \hat{n}(x)x \right\} | \Psi_0 \rangle.
\end{aligned} \tag{A.2.67}
$$

We now take the square of the modulus of this matrix element:

$$
\begin{aligned}
|\delta v_{\mathrm{n}0}|^2 &= \delta v_{\mathrm{n}0}^* \, \delta v_{\mathrm{n}0} \\
&= e\mathcal{E} \langle \Psi_0 | \left\{ \int dx \, \hat{n}(x)x \right\} | \Psi_n \rangle \times e\mathcal{E} \langle \Psi_n | \left\{ \int dx' \, \hat{n}(x')x' \right\} | \Psi_0 \rangle \\
&= e^2\mathcal{E}^2 \langle \Psi_0 | \left\{ \int dx \, \hat{n}(x)x \right\} | \Psi_n \rangle \langle \Psi_n | \left\{ \int dx' \, \hat{n}(x')x' \right\} | \Psi_0 \rangle, \qquad \text{(A.2.68)}
\end{aligned}
$$

and substitute this into Eq. (A.2.65):

$$
\begin{aligned}
P &= \omega \sum_n \left[\frac{e^2\mathcal{E}^2 \pi}{2} \langle \Psi_0 | \left\{ \int dx \, \hat{n}(x)x \right\} | \Psi_n \rangle \langle \Psi_n | \left\{ \int dx' \, \hat{n}(x')x' \right\} | \Psi_0 \rangle \times \right. \\
&\qquad \left. \delta(\omega - (E_n - E_0)) \right] \\
&= \frac{e^2\mathcal{E}^2 \pi \omega}{2} \int dx \int dx' \left[x \, x' \sum_n \langle \Psi_0 | \hat{n}(x) | \Psi_n \rangle \langle \Psi_n | \hat{n}(x') | \Psi_0 \rangle \delta(\omega - (E_n - E_0)) \right].
\end{aligned}
$$
$$
\text{(A.2.69)}
$$

We divide this by the intensity of the perturbing field [Eq. (A.2.35)] and switch to Hartree atomic units:

$$
\frac{P}{I} = \frac{4\pi^2 \omega}{c} \int dx \int dx' \left[x \, x' \sum_n \langle \Psi_0 | \hat{n}(x') | \Psi_n \rangle \langle \Psi_n | \hat{n}(x) | \Psi_0 \rangle \delta(\omega - (E_n - E_0)) \right].
$$
$$
\text{(A.2.70)}
$$

Finally, through Eq. (A.2.50), we obtain $\sigma(\omega)$ in terms of the density-response function:

$$
\sigma(\omega) = -\frac{4\pi\omega}{c} \int dx \int dx' \, \text{Im}\big[\chi(x, x', \omega)\big] \, x \, x', \qquad \text{(A.2.71)}
$$

where we note that the expression for χ in the Lehmann representation, and hence Eq. (A.2.50), includes terms representing stimulated emission, which we were free to include in the above proof but neglected for simplicity.

ɪDEA

B.1 Imaginary time propagation

As discussed in Chapter 3, the old version of iDEA involved propagating a trial wavefunction through imaginary time to determine the exact ground state of the system. While the new version of iDEA uses an improved method, the results presented in Chapter 4 were generated using this old method, and so we discuss it below, along with the Crank-Nicolson scheme that was used to perform it.

We start from the time-dependent Schrödinger equation:

$$\hat{H}\Psi(\{x_i\},t) = i\frac{\partial}{\partial t}\Psi(\{x_i\},t). \tag{B.1.1}$$

If the Hamiltonian operator does not explicitly depend on time, the time-evolution operator [Eq. (A.1.14)] reduces to $\hat{U}(t) = -it\hat{H}$, and the solution to the TDSE is trivial:

$$\Psi(\{x_i\},t) = e^{-it\hat{H}}\Psi(\{x_i\},t=0). \tag{B.1.2}$$

We can expand the wavefunction at $t = 0$ in the basis of the many-electron eigenstates $\{\Psi_m\}$:

$$\Psi(x,t=0) = \sum_m c_m\Psi_m, \tag{B.1.3}$$

which are the set of solutions to the time-independent Schrödinger equation:

$$\hat{H}\Psi_m = E_m\Psi_m. \tag{B.1.4}$$

This allows us to recast the time-dependent wavefunction:

$$\Psi(x,t) = e^{-it\hat{H}}\sum_m c_m\Psi_m. \tag{B.1.5}$$

Achieving a Taylor expansion[1] of $\hat{U}(t)$:

$$e^x = \sum_{n=0}^{\infty} \frac{x^n}{n!} \implies e^{-it\hat{H}} = \sum_{n=0}^{\infty} \frac{(-it\hat{H})^n}{n!}. \tag{B.1.6}$$

Substituting this into the RHS of Eq. (B.1.5):

$$\begin{aligned} \Psi(x,t) &= e^{-it\hat{H}} \sum_m c_m \Psi_m \\ &= \sum_m c_m e^{-it\hat{H}} \Psi_m \\ &= \sum_m \sum_{n=0}^{\infty} c_m \frac{(-it\hat{H})^n}{n!} \Psi_m \\ &= \sum_m \sum_{n=0}^{\infty} c_m \frac{(-itE_m)^n}{n!} \Psi_m \\ &= \sum_m c_m e^{-itE_m} \Psi_m, \end{aligned} \tag{B.1.7}$$

i.e. the wavefunction is a weighted sum of eigenstates that are oscillatory in time. By making the substitution $\tau = it$:

$$\hat{U}(t) = e^{-it\hat{H}} \longrightarrow \hat{U}(\tau) = e^{-\tau\hat{H}}, \tag{B.1.8}$$

and so we obtain the wavefunction in imaginary time:

$$\Psi(x,\tau) = \sum_m c_m e^{-E_m \tau} \Psi_m. \tag{B.1.9}$$

I.e. the terms, which are oscillatory in real time, decay exponentially in imaginary time.

B.1.1   The Crank-Nicolson method

We begin by considering the time evolution of the wavefunction, given in Eq. (B.1.2):

$$\Psi(\{x_i\},t) = e^{-it\hat{H}} \Psi(\{x_i\}, t=0). \tag{B.1.10}$$

---

[1]Operators (e.g. $\hat{H}$) Taylor expand in the same way as variables (e.g. x).

At a time δt later:

$$
\begin{aligned}
\Psi(\{x_i\}, t + \delta t) &= e^{-i(t+\delta t)\hat{H}} \Psi(\{x_i\}, t = 0) \\
&= e^{-i\delta t \hat{H}} e^{-it\hat{H}} \Psi(\{x_i\}, t = 0) \\
&= e^{-i\delta t \hat{H}} \Psi(\{x_i\}, t).
\end{aligned}
\tag{B.1.11}
$$

Premultiplying both sides by $e^{i\frac{\delta t}{2}\hat{H}}$:

$$
e^{i\frac{\delta t}{2}\hat{H}} \Psi(\{x_i\}, t + \delta t) = e^{-i\frac{\delta t}{2}\hat{H}} \Psi(\{x_i\}, t).
\tag{B.1.12}
$$

Achieving Taylor expansions of both exponential terms and truncating to first order in δt:

$$
e^x = \sum_{n=0}^{\infty} \frac{x^n}{n!} \implies e^{\pm i\frac{\delta t}{2}\hat{H}} = \sum_{n=0}^{\infty} \frac{\left(\pm i\frac{\delta t}{2}\hat{H}\right)^n}{n!} = 1 \pm i\frac{\delta t}{2}\hat{H} + \mathcal{O}(\delta t^2).
\tag{B.1.13}
$$

Substituting into Eq. (B.1.12):

$$
\left(1 + i\frac{\delta t}{2}\hat{H}\right) \Psi(\{x_i\}, t + \delta t) = \left(1 - i\frac{\delta t}{2}\hat{H}\right) \Psi(\{x_i\}, t).
\tag{B.1.14}
$$

This constitutes a matrix equation:

$$
\left(I + i\frac{\delta t}{2}H\right) \Psi(\{x_i\}, t + \delta t) = \left(I - i\frac{\delta t}{2}H\right) \Psi(\{x_i\}, t),
\tag{B.1.15}
$$

where I is the identity matrix. This can also be cast into imaginary time by making the substitution $\tau = it$:

$$
\left(I + \frac{\delta \tau}{2}H\right) \Psi(\{x_i\}, \tau + \delta \tau) = \left(I - \frac{\delta \tau}{2}H\right) \Psi(\{x_i\}, \tau).
\tag{B.1.16}
$$

The above two equations are accurate to $\mathcal{O}(\delta t^2)$ and $\mathcal{O}(\delta \tau^2)$ respectively, as a result of the truncation made in Eq. (B.1.13).

B.2 Derivative stencils

As iDEA implements finite-difference methods on a real-space grid, the position variable x is discretised, functions become vectors and operators become matrices. Below we derive the matrix representation of the second-derivative operator, which is necessary to solve several differential equations, e.g. the many-electron Schrödinger

equation and KS equations.

Consider a function $f(x)$ expanded about two points, $x + \delta x$ and $x - \delta x$, through a Taylor series:

$$
\begin{aligned}
f(x \pm \delta x) &= \sum_{n=0}^{\infty} (\pm 1)^n \frac{f^{(n)}(x)}{n!} \delta x^n \\
&= f(x) \pm f'(x)\delta x + \frac{f''(x)\delta x^2}{2!} \pm \frac{f'''(x)\delta x^3}{3!} + \mathcal{O}(\delta x^4).
\end{aligned}
\qquad \text{(B.2.17)}
$$

Summing both terms gives

$$
\begin{aligned}
f(x + \delta x) + f(x - \delta x) &= \sum_{n=0}^{\infty} \left[1 + (-1)^n\right] \frac{f^{(n)}(x)}{n!} \delta x^n \\
&= 2f(x) + f''(x)\delta x^2 + \mathcal{O}(\delta x^4).
\end{aligned}
\qquad \text{(B.2.18)}
$$

Rearranging allows us to obtain an expression for the second derivative of f at the point x:

$$
f''(x) \approx \frac{f(x - \delta x) - 2f(x) + f(x + \delta x)}{\delta x^2},
\qquad \text{(B.2.19)}
$$

where we have truncated all terms $\mathcal{O}(\delta x^2)$. On a discretised grid with M points, the function $f(x)$ becomes a vector with M elements. As such, we obtain the second derivative of $f(x)$ as

$$
\frac{d^2 f}{dx^2} = \left(\frac{d^2}{dx^2}\right)
\begin{bmatrix} f_1 \\ f_2 \\ f_3 \\ \vdots \\ f_M \end{bmatrix}
\approx \frac{1}{\delta x^2}
\begin{pmatrix}
-2 & 1 & 0 & 0 & 0 \\
1 & -2 & 1 & 0 & 0 \\
0 & 1 & -2 & \ddots & 0 \\
0 & 0 & \ddots & \ddots & 1 \\
0 & 0 & 0 & 1 & -2
\end{pmatrix}
\begin{bmatrix} f_1 \\ f_2 \\ f_3 \\ \vdots \\ f_M \end{bmatrix}
\qquad \text{(B.2.20)}
$$

where the second-derivative matrix takes the form

$$
\frac{d^2}{dx^2} \approx \frac{1}{\delta x^2}
\begin{pmatrix}
-2 & 1 & 0 & 0 & 0 \\
1 & -2 & 1 & 0 & 0 \\
0 & 1 & -2 & \ddots & 0 \\
0 & 0 & \ddots & \ddots & 1 \\
0 & 0 & 0 & 1 & -2
\end{pmatrix}
\qquad \text{(B.2.21)}
$$

This is a tridiagonal matrix and is known as a three-point stencil. Higher-order approximations can be obtained (e.g. a five-point stencil with $\mathcal{O}(\delta x^4)$) by taking more

terms into account in Eq. (B.2.19). iDEA currently implements three-, five-, seven-, nine-, eleven- and thirteen-point stencils. For a fixed grid point number, the Hamiltonian matrix is less sparse for higher-order stencils, thereby leading to an increase in computation time. However, the higher-order stencils are much more accurate, and so less grid points can be used, thereby speeding up computation time. The user is free to specify the stencil to be used in a calculation, with these trade-offs being taken into account.

B.3 Density-response functions

The interacting density-response function

$$\chi(x, x', \omega) = \lim_{\eta \to 0^+} \sum_n \left[\frac{\langle \Psi_0 | \hat{n}(x) | \Psi_n \rangle \langle \Psi_n | \hat{n}(x') | \Psi_0 \rangle}{\omega - (E_n - E_0) + i\eta} - \frac{\langle \Psi_0 | \hat{n}(x') | \Psi_n \rangle \langle \Psi_n | \hat{n}(x) | \Psi_0 \rangle}{\omega + (E_n - E_0) + i\eta} \right],$$
(B.3.22)

is characterised by the amplitudes ($\langle \Psi_0 | \hat{n}(x) | \Psi_n \rangle$ etc.), which are determined from the many-electron eigenstates. We find expressions for these numerators for two-electron systems on a real-space grid. This is necessary for the results presented in Chapter 6.

B.3.1 Implementation for two-electron systems

We consider a two-electron system with ground state $\Psi_0(x_1, x_2)$ and $n-$th excited state $\Psi_n(x_1, x_2)$. We use these, along with the density operator $\hat{n}(x) = \sum_i \delta(x - x_i)$, to evaluate the first amplitude in Eq. (B.3.22):

$$\begin{aligned} \langle \Psi_0 | \hat{n}(x) | \Psi_n \rangle &= \int dx_1 \int dx_2 \, \Psi_0^*(x_1, x_2) \left[\delta(x - x_1) + \delta(x - x_2) \right] \Psi_n(x_1, x_2) \\ &= \int dx_2 \, \Psi_0^*(x, x_2) \Psi_n(x, x_2) + \int dx_1 \, \Psi_0^*(x_1, x) \Psi_n(x_1, x) \\ &= \int dx' \, \Psi_0^*(x, x') \Psi_n(x, x') + \int dx' \, \Psi_0^*(x', x) \Psi_n(x', x), \end{aligned}$$
(B.3.23)

where we have replaced the dummy variables x_1 and x_2 with x'. Finally, we can exploit the exchange-antisymmetry of $\Psi_0(x_1, x_2)$ and $\Psi_n(x_1, x_2)$ to combine the integrals and obtain

$$\langle \Psi_0 | \hat{n}(x) | \Psi_n \rangle = 2 \int dx' \, \Psi_0^*(x', x) \Psi_n(x', x).$$
(B.3.24)

Similarly:

$$\langle \Psi_n | \hat{n}(x') | \Psi_0 \rangle = 2 \int dx \, \Psi_n^*(x, x') \Psi_0(x, x'),$$

$$\langle \Psi_0 | \hat{n}(x') | \Psi_n \rangle = 2 \int dx \, \Psi_0^*(x, x') \Psi_n(x, x'),$$

$$\langle \Psi_n | \hat{n}(x) | \Psi_0 \rangle = 2 \int dx' \, \Psi_n^*(x', x) \Psi_0(x', x).$$

It should be noted that as our Hamiltonian matrix is real and symmetric the associated eigenvectors, i.e. solutions to the TISE, are real ($\Psi_0 = \Psi_0^*$, $\Psi_n = \Psi_n^* \; \forall \, n$), and therefore so are the amplitudes.

DETAILS OF CALCULATIONS

C.1 Chapter 4

C.1.1 Finite LDAs

The slab systems have electron densities of the form

$$n(x) = n_0 \exp\left[-10^{-11}(mx)^{12}\right], \tag{C.1.1}$$

where n_0 is the value of the plateau region and m is a scaling factor chosen so that the density integrates to the appropriate number of electrons (1, 2 or 3).

The xc energy density in the three finite LDAs is parameterised by

$$\varepsilon_{\text{xc}}(n) = (A + Bn + Cn^2 + Dn^3 + En^4 + Fn^5)n^G. \tag{C.1.2}$$

The parameterisation of the xc potential is obtained:

$$v_{\text{xc}}^{\text{LDA}}(n) = \varepsilon_{\text{xc}}(n(x)) + n(x)\frac{d\varepsilon_{\text{xc}}}{dn}\Big|_{n(x)}$$

$$= \Big[A(1+G) + B(2+G)n + C(3+G)n^2$$
$$+ D(4+G)n^3 + E(5+G)n^4$$
$$+ F(6+G)n^5\Big]n^G. \tag{C.1.3}$$

C.1.2 HEG LDAs

In the HEG LDA, the xc energy density is split into separate exchange and correlation parts. Consequently, the xc potential is also split into separate exchange and correlation parts.

The exchange energy density in the HEG LDA is parameterised as in Eq. (C.1.2), and so the exchange potential is of the same form as Eq. (C.1.3).

The correlation energy density in the HEG LDA is parameterised by

$$\varepsilon_c(r_s) = -\frac{A_{\mathrm{RPA}}r_s + Er_s^2}{1 + Br_s + Cr_s^2 + Dr_s^3}\frac{\ln\left(1 + \alpha r_s + \beta r_s^2\right)}{\alpha}, \tag{C.1.4}$$

where $2r_s = 1/n$. The correlation potential is given by

$$\begin{aligned}
v_c(r_s) = \varepsilon_c(r_s) \;-\; &\frac{r_s}{\alpha(1 + Br_s + Cr_s^2 + Dr_s^3)}\Bigg[-(A + 2Er_s)\ln\left(1 + \alpha r_s + \beta r_s^2\right) \\
&+ \frac{(Ar_s + Er_s^2)(B + 2Cr_s + 3Dr_s^2)\ln\left(1 + \alpha r_s + \beta r_s^2\right)}{1 + Br_s + Cr_s^2 + Dr_s^3} \\
&- \frac{(Ar_s + Er_s^2)(\alpha + 2\beta r_s)}{(1 + \alpha r_s + \beta r_s^2)}\Bigg].
\end{aligned} \tag{C.1.5}$$

C.1.3   System 1 (Two-electron harmonic well)

The external potential is

$$v_{\mathrm{ext}}(x) = \frac{1}{2}\omega^2 x^2, \tag{C.1.6}$$

where $\omega = \frac{2}{3}$ a.u. The system has a spatial length of 16 a.u. and is sampled with 1601 grid points for exact and Hartree-Fock calculations, leading to a grid spacing of $\delta x = 0.01$ a.u. The system is sampled with 3201 grid points for LDA calculations, leading to a grid spacing of $\delta x = 0.005$ a.u.

C.1.4   System 2 (Three-electron harmonic well)

The external potential is of the same form as Eq. (C.1.6) with $\omega = \frac{1}{2}$ a.u. The system has a spatial length of 16 a.u. and is sampled with 401 grid points for exact and Hartree-Fock calculations, leading to a grid spacing of $\delta x = 0.04$ a.u. The system is sampled with 4001 grid points for LDA calculations, leading to a grid spacing of $\delta x = 0.004$ a.u.

C.1.5   System 3 (Two-electron double well)

The external potential is

$$v_{\mathrm{ext}}(x) = \alpha x^{10} - \beta x^4, \tag{C.1.7}$$

where $\alpha = 5 \times 10^{-11}$ and $\beta = 1.3 \times 10^{-4}$. The system has a spatial length of 30 a.u. and is sampled with 2001 grid points for exact and Hartree-Fock calculations, leading to a grid spacing of $\delta x = 0.015$ a.u. The system is sampled with 4001 grid points for LDA calculations, leading to a grid spacing of $\delta x = 0.0075$ a.u.

C.1.6 System 4 (Two-electron atom)

The external potential is

$$v_{\text{ext}}(x) = -\frac{a}{|x| + a}, \tag{C.1.8}$$

where $a = 20$ a.u. The system has a spatial length of 60 a.u. and is sampled with 2001 grid points for exact and Hartree-Fock calculations, leading to a grid spacing of $\delta x = 0.03$ a.u. The system is sampled with 4001 grid points for LDA calculations, leading to a grid spacing of $\delta x = 0.015$ a.u.

C.1.7 System 5 (Three-electron atom)

The external potential is of the same form as Eq. (C.1.8) with $a = 50$ a.u. The system has a spatial length of 90 a.u. and is sampled with 401 grid points for exact and Hartree-Fock calculations, leading to a grid spacing of $\delta x = 0.225$ a.u. The system is sampled with 4001 grid points for LDA calculations, leading to a grid spacing of $\delta x = 0.0225$ a.u.

C.2 Chapter 5

C.2.1 System 1 (Two-electron Gaussian well)

The unperturbed and perturbed external potentials are

$$v_{\text{ext}}(x, t = 0) = -ae^{-bx^2}, \tag{C.2.9}$$

$$v_{\text{ext}}(x, t > 0) = -ae^{-bx^2} - \varepsilon x, \tag{C.2.10}$$

where $a = 0.75$ a.u., $b = 0.1$ a.u. and $\varepsilon = 0.02$ a.u. The system has a spatial length of 30 a.u. and is sampled with 151 grid points, leading to a grid spacing of $\delta x = 0.2$ a.u. Real time propagation is simulated for 8 a.u. and is sampled with 1601 time points, leading to a time step of $\delta t = 0.005$ a.u. To determine how well the fluidic approximation satisfies the zero-force theorem, we use $\delta x = 0.06$ a.u. and $\delta t = 4 \times 10^{-4}$ a.u.

C.2.2   System 2A (Two-electron atom)

The unperturbed and perturbed external potentials are

$$v_{\text{ext}}(x, t = 0) = -\frac{a}{|x| + a},$$
<div align="right">(C.2.11)</div>

$$v_{\text{ext}}(x, t > 0) = -\frac{a}{|x| + a} + \varepsilon \cos(bx),$$
<div align="right">(C.2.12)</div>

where $a = 20$ a.u., $\varepsilon = 0.02$ a.u. and $b = 0.75$. The system has a spatial length of 40 a.u. and is sampled with 151 grid points, leading to a grid spacing of $\delta x \approx 0.27$ a.u. Real time propagation is simulated for 5 a.u. and is sampled with 1001 time points, leading to a time step of $\delta t = 0.005$ a.u.

C.2.3   System 2B (Three-electron atom)

The potentials are of the same form as Eq. (C.2.11) and Eq. (C.2.12) with $a = 20$ a.u., $\varepsilon = 0.02$ a.u. and $b = 0.75$. The system has a spatial length of 50 a.u. and is sampled with 121 grid points, leading to a grid spacing of $\delta x \approx 0.42$ a.u. Real time propagation is simulated for 5 a.u. and is sampled with 1001 time points, leading to a time step of $\delta t = 0.005$ a.u.

C.2.4   System 2C (Strongly disrupted three-electron atom)

The potentials are of the same form as Eq. (C.2.11) and Eq. (C.2.12) with $a = 20$ a.u., $\varepsilon = 0.1$ a.u. and $b = 0.75$. The system has a spatial length of 50 a.u. and is sampled with 121 grid points, leading to a grid spacing of $\delta x \approx 0.42$ a.u. Real time propagation is simulated for 18 a.u. and is sampled with 9001 time points, leading to a time step of $\delta t = 0.002$ a.u.

C.2.5   System 3 (Two-electron tunnelling system)

The unperturbed and perturbed external potentials are

$$v_{\text{ext}}(x, t = 0) = \frac{a}{e^{4(-|x+4.5|+3.5)} + 1} - \frac{a}{e^{4(|x-4.5|-3.5)} + 1} - a,$$
<div align="right">(C.2.13)</div>

$$v_{\text{ext}}(x, t > 0) = \frac{a/2}{e^{4(-|x+4.5|+3.5)} + 1} - \frac{3a/2}{e^{4(|x-4.5|-3.5)} + 1} - \frac{a}{2},$$
<div align="right">(C.2.14)</div>

where $a = 0.3$ a.u. The system has a spatial length of 20 a.u. and is sampled with 301 grid points, leading to a grid spacing of $\delta x \approx 0.07$ a.u. Real time propagation is

simulated for 15 a.u. and is sampled with 3001 time points, leading to a time step of $\delta t = 0.005$ a.u.

C.3 Chapter 6

C.3.1 Sum rule

The exact f_{xc} satisfies the zero-force sum rule (see Sec. 2.5.3.1; Eq. (2.51)):

$$\int f_{xc}(x, x', \omega) \partial_{x'} n_0(x') \, dx' = \partial_x v_{xc}^0(x), \tag{C.3.15}$$

where n_0 is the ground-state density and v_{xc}^0 is the ground-state xc potential. As well as giving the correct absorption spectrum from the exact χ_0, we check that the f_{xc} for each model system satisfies this sum rule.

C.3.2 System 1 (Two-electron harmonic well)

The external potential is

$$v_{ext}(x) = \frac{1}{2} \omega_0^2 x^2, \tag{C.3.16}$$

where $\omega_0 = 0.25$ a.u. The system has a spatial length of 20 a.u. and is sampled with 101 grid points, leading to a grid spacing of $\delta x = 0.2$ a.u. We have replaced the positive infinitesimal η with 0.005 to broaden the absorption peaks for ease of viewing. We calculate all many-electron eigenstates and Kohn-Sham orbitals, to obtain converged results for χ and χ_0 respectively. We verify that the exact f_{xc} obtained is correct by checking that it satisfies Eq. (C.3.15) [Fig. C.1(a)].

C.3.3 System 3 (Two-electron atom)

The external potential is

$$v_{ext}(x) = -\frac{a}{|x| + a}, \tag{C.3.17}$$

where $a = 20$ a.u. The system has a spatial length of 50 a.u. and is sampled with 201 grid points, leading to a grid spacing of $\delta x = 0.25$ a.u. We have replaced the positive infinitesimal η with 0.002 to broaden the absorption peaks for ease of viewing. We calculate all many-electron eigenstates and Kohn-Sham orbitals, to obtain converged results for χ and χ_0 respectively. We verify that the exact f_{xc} obtained is correct by checking that it satisfies Eq. (C.3.15) [Fig. C.1(b)].
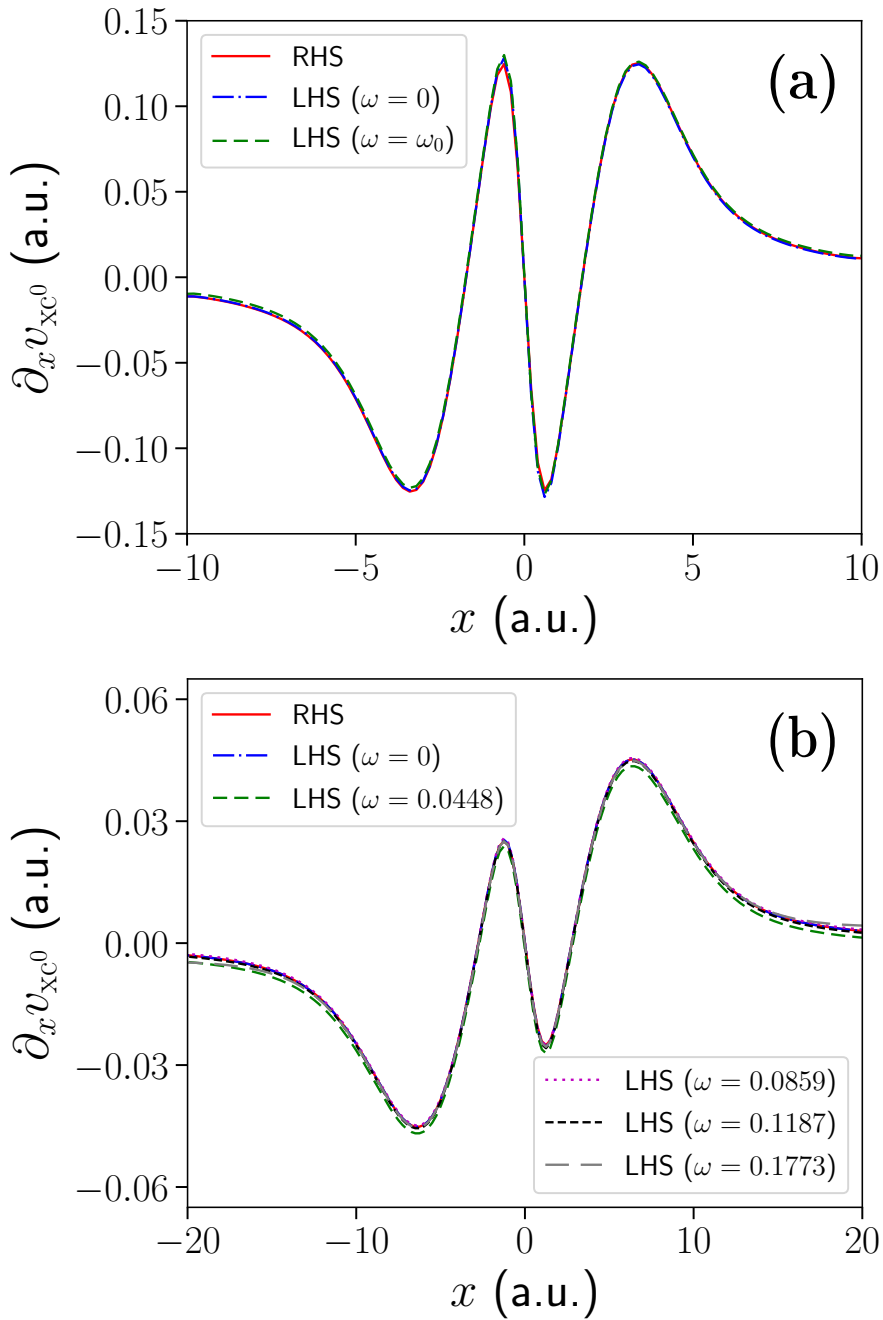
Fig. C.1. We confirm the exact f_{xc} obtained for each system satisfies the sum rule [Eq. (C.3.15)]. The RHS of the equation is obtained through direct differentiation of the exact ground-state xc potential (solid red in both plots): (a) For the harmonic well system, we evaluate the LHS of the equation at $\omega = 0$ (dotted-dashed blue) and at the first excitation $\omega = \omega_0$ (dashed green), both of which should be equal to the RHS if the sum rule is satisfied. (b) For the atom-like system, we evaluate the LHS of the equation at $\omega = 0$ (dotted-dashed blue), at the first excitation $\omega = 0.0448$ (dashed green), at the second excitation $\omega = 0.0859$ (dotted magenta), at the third excitation $\omega = 0.1187$ (short-dashed black), and at the sixth excitation $\omega = 0.1773$ (long-dashed grey), all of which should be equal to the RHS if the sum rule is satisfied. While there are discrepancies between the sets of curves in both plots, it is important to note that these discrepancies are much smaller in magnitude than f_{xc} is (Fig. 6.2 and Fig. 6.6 in Chapter 6). They can therefore be attributed to small numerical errors in f_{xc}.

FLUIDIC APPROXIMATION

D.1   Gauge transformation

We begin by considering the time-dependent Schrödinger equation (TDSE) for a system under the influence of a scalar potential v and vector potential A:

$$i\frac{\partial}{\partial t}\Psi(x,t) = \frac{1}{2}\left(-i\frac{\partial}{\partial x} + A(x,t)\right)^2 \Psi(x,t) + v(x,t)\Psi(x,t), \qquad \text{(D.1.1)}$$

where the first term in the brackets on the RHS is the momentum operator. Gauge theory tells us that we are free to make certain changes of gauge without affecting the physical characteristics of the system, meaning that the TDSE continues to be satisfied. Specifically:

$$\Psi(x,t) \longrightarrow e^{-i\theta(x,t)}\Psi(x,t), \qquad \text{(D.1.2a)}$$

$$A(x,t) \longrightarrow A(x,t) - \frac{\partial}{\partial x}\theta(x,t), \qquad \text{(D.1.2b)}$$

$$v(x,t) \longrightarrow v(x,t) + \frac{\partial}{\partial t}\theta(x,t), \qquad \text{(D.1.2c)}$$

which allows us to modify the scalar and vector potentials, without detriment to their associated fields. We utilise this in Sec. D.3, introducing the concept of a "local instantaneous rest frame".

D.2   Galilean transformation

Suppose we are in some frame S (the lab frame) with $A = 0$, such that Eq. (D.1.1) becomes

$$i\frac{\partial}{\partial t}\Psi(x,t) = -\frac{1}{2}\frac{\partial^2}{\partial x^2}\Psi(x,t) + v(x,t)\Psi(x,t). \qquad \text{(D.2.3)}$$

If we transform to some different (inertial) frame S', moving with velocity u relative to frame S, the TDSE remains invariant:

$$i\frac{\partial}{\partial t}\Psi'(x',t) = -\frac{1}{2}\frac{\partial^2}{\partial x'^2}\Psi'(x',t) + v'(x',t)\Psi'(x',t), \qquad (D.2.4)$$

where

$$x' = x - ut, \qquad (D.2.5a)$$

$$v'(x',t) = v(x,t) = v(x'+ut,t), \qquad (D.2.5b)$$

$$\Psi'(x',t) = e^{-i(ux'+ut^2/2)}\Psi(x,t), \qquad (D.2.5c)$$

and can be verified by direct substitution into Eq. (D.2.4). This Galilean invariance is a special case of generalised translational invariance [26], and the scalar potential rigidly follows the rigidly translated time-dependent density, $n'(x',t) = n(x'+ut,t)$.

D.3   Local instantaneous rest frame

Let us now consider a KS system that is at rest in frame S', such that the density moves rigidly with velocity u when viewed from frame S. In S' the KS potential (purely scalar) will be $v_s'(x',t) = v_s^{\mathrm{A}}[n'(x')]$, i.e. the adiabatic KS potential evaluated on $n'(x')$, which is static. Transforming to S through the above Galilean transformation maintains zero vector potential, and the scalar potential continues to be given by the adiabatic expression but moving along with velocity u [Eq. (D.2.5b)], i.e. following the density.

In S we now apply a gauge transformation, $A_s \to -u$. Through Eq. (D.1.2b) and Eq. (D.1.2c) we see that v_s remains unchanged ($\theta = ux$). So, if the KS system is in the ground state in frame S', then neither transforming to frame S through a Galilean transformation, nor making the gauge transformation in S, affects the validity of the adiabatic KS potential: $v_s = v_s^{\mathrm{A}}$.

But in general the system will not be at rest in frame S', and so the density in frame S will not be rigidly translating with a uniform and constant velocity u. Since $u(x,t)$ may be significantly x- and t-dependent, there is no universal rest frame S'. But, by imagining a vector potential $A_s(x,t) = -u(x,t)$ in S, we are achieving the effect of transforming to the *local instantaneous rest frame*[1], in which only a weak non-adiabatic

---

[1]Apart from a unimportant temporal phase factor in the KS orbitals, taking the same form as that in

correction to v_s^A is required. In particular, the effects of acceleration ($\dot{u} \neq 0$) and dispersion ($\partial_x u \neq 0$) have least effect in a frame where u itself is zero. Additionally, the rate of change of kinetic energy, which provides a measure of the scale of any non-adiabatic potential, is proportional to $u\dot{u}$ (as in classical mechanics), and so is smallest when u is zero. We now make the simple assumption that the non-adiabatic correction in the local instantaneous rest frame is zero, and approximate the KS potential as exactly adiabatic there. Recasting this vector potential as a scalar potential through Eq. (D.1.2b) and Eq. (D.1.2c) we obtain the non-adiabatic correction to the adiabatic potential:

$$\Delta v_s(x, t > 0) = -\int_{-\infty}^{x} \frac{\partial}{\partial t} u(x', t > 0)\, dx',\qquad \text{(D.3.6)}$$

which we term the *fluidic* approximation, as stated in Eq. (5.3) in Chapter 5.

D.4 The harmonic potential theorem

The harmonic potential theorem [27] (HPT), which is a special case of generalised translational invariance, shows that in a system of interacting electrons in a harmonic potential, subject to a uniform electric field at $t = 0$, the density rigidly moves in the manner of the underlying classical harmonic oscillator. Below, we state the HPT (see Ref. 27 for the original proof) and then show that the fluidic approximation adds exactly the non-adiabatic correction required (apart from an unimportant time-dependent constant) by the HPT[2].

The unperturbed and perturbed external potentials are

$$v_{\text{ext}}^0(x) = \frac{1}{2}\omega_0^2 x^2,\qquad \text{(D.4.7a)}$$

$$v_{\text{ext}}(x, t) = \frac{1}{2}\omega_0^2 x^2 + \mathcal{E}x\cos(\omega t),\qquad \text{(D.4.7b)}$$

where ω_0 is the angular frequency of the harmonic well and $\mathcal{E}$ is the amplitude of the the uniform electric field oscillating with angular frequency ω.

Ref. 27 showed that the time-dependent density is simply the ground-state density rigidly translated, $n(x, t) = n_0(x - X(t))$, where the translation vector $X(t)$ is

---

Eq. (D.1.2a) with $\theta(x, t) = u(x, t)x$.

[2]We have also confirmed this numerically for two interacting electrons in a harmonic potential where the perturbing field is static ($\omega = 0$).

described by the equation of motion of a (classical) driven harmonic oscillator:

$$\ddot{X} + \omega_0^2 X = -\mathcal{E}\cos(\omega t), \tag{D.4.8}$$

and is given by

$$X(t) = \frac{\mathcal{E}}{\omega_0^2 - \omega^2}(\cos(\omega_0 t) - \cos(\omega t)). \tag{D.4.9}$$

The exact ground-state and time-dependent KS potentials are given by

$$v_s^0(x) = \frac{1}{2}\omega_0^2 x^2 + v_{\mathrm{H}}^0(x) + v_{\mathrm{xc}}^0(x), \tag{D.4.10a}$$

$$v_s(x,t) = \frac{1}{2}\omega_0^2 x^2 + \mathcal{E}x\cos(\omega t) + v_{\mathrm{H}}^0(x - X(t)) + v_{\mathrm{xc}}^0(x - X(t)), \tag{D.4.10b}$$

where the time-dependent Hartree and xc potentials are their ground-state counterparts translated[3]. We can also decompose $v_s(x,t)$ into its adiabatic part:

$$
\begin{aligned}
v_s^{\mathrm{A}}(x,t) &= v_s^0(x - X(t)) \\
&= \frac{1}{2}\omega_0^2(x - X(t))^2 + v_{\mathrm{H}}^0(x - X(t)) + v_{\mathrm{xc}}^0(x - X(t)),
\end{aligned} \tag{D.4.11}
$$

and non-adiabatic part:

$$
\begin{aligned}
\Delta v_s(x,t) &= v_s(x,t) - v_s^{\mathrm{A}}(x,t) \\
&= \mathcal{E}x\cos(\omega t) + \omega_0^2 x X(t) \underbrace{- \frac{1}{2}\omega_0^2 X(t)^2}_{c(t)} \\
&= \mathcal{E}x\cos(\omega t) + \omega_0^2 x \left[\frac{\mathcal{E}}{\omega_0^2 - \omega^2}(\cos(\omega_0 t) - \cos(\omega t)) \right] + c(t) \\
&= \mathcal{E}x\left[1 - \frac{\omega_0^2}{\omega_0^2 - \omega^2}\right]\cos(\omega t) + \frac{\mathcal{E}\omega_0^2 x}{\omega_0^2 - \omega^2}\cos(\omega_0 t) + c(t) \\
&= \frac{\mathcal{E}x}{\omega_0^2 - \omega^2}\left[\omega_0^2\cos(\omega_0 t) - \omega^2\cos(\omega t)\right] + c(t).
\end{aligned} \tag{D.4.12}
$$

At each instant, v_s^{A} is the DFT KS potential whose ground-state density is equal to the exact time-dependent density, with Δv_s constituting the remainder of v_s.

We now prove that the fluidic approximation is exact in the case of HPT systems. To start with, we consider the velocity field, which is the time derivative of the trans-

---

[3]As the time-dependent density is simply the ground-state density rigidly translated, the time-dependent v_{H} and v_{xc} are simply their ground-state counterparts rigidly translated, as a consequence of generalised translational invariance (see Refs [26] and [180]; Eq. (2.29)).

lation vector:

$$u = \dot{X} = \frac{\mathcal{E}}{\omega_0^2 - \omega^2} \left[\omega \sin(\omega t) - \omega_0 \sin(\omega_0 t) \right], \tag{D.4.13}$$

and take the time derivative one more time:

$$\dot{u} = \ddot{X} = \frac{\mathcal{E}}{\omega_0^2 - \omega^2} \left[\omega^2 \cos(\omega t) - \omega_0^2 \cos(\omega_0 t) \right]. \tag{D.4.14}$$

Substituting this into the fluidic approximation [Eq. (D.3.6)]:

$$\begin{aligned} \Delta v_s(x, t) &= - \int_{-\infty}^{x} \dot{u} \, dx' \\ &= -\ddot{X} x \\ &= \frac{\mathcal{E} x}{\omega_0^2 - \omega^2} \left[\omega_0^2 \cos(\omega_0 t) - \omega^2 \cos(\omega t) \right]. \end{aligned} \tag{D.4.15}$$

This is equal to the exact non-adiabatic potential, apart from the time-dependent constant $c(t)$, which is unimportant as it has no effect on the density, and the KS potential is only defined up to an additive constant. The HPT is therefore satisfied by the fluidic approximation[4].

---

[4]To be clear, we have proven that the fluidic approximation satisfies the HPT. To prove the HPT itself, one needs to consider generalised translational invariance of the system, as is done in Ref. 27.

ABBREVIATIONS

1D one dimension.

1e one-electron.

2e two-electron.

3e three-electron.

ALDA adiabatic local density approximation.

BSE Bethe-Salpeter equation.

DFT density functional theory.

DMC diffusion Monte Carlo.

EELS electron energy loss spectra.

EXX exact exchange.

GGA generalised gradient approximation.

GK Gross-Kohn.

HEG homogeneous electron gas.

HF Hartree-Fock.

HK Hohenberg-Kohn.

HOMO highest occupied molecular orbital.

HPT harmonic potential theorem.

Hxc Hartree-exchange-correlation.

iDEA interacting Dynamic Electrons Approach.

KS Kohn-Sham.

LDA local density approximation.

LHS left-hand side.

LRDMC lattice regularized diffusion Monte Carlo.

LUMO lowest unoccupied molecular orbital.

MAE mean absolute error.

OEP optimised effective potential.

QMC quantum Monte Carlo.

RHS right-hand side.

RMSE root-mean-square error.

RPA random phase approximation.

SCF self-consistent field.

SIC self-interaction correction.

SVD singular-value decomposition.

TDCDFT time-dependent current density functional theory.

TDDFT time-dependent density functional theory.

TDSE time-dependent Schrödinger equation.

TISE time-independent Schrödinger equation.

VK Vignale-Kohn.

xc exchange-correlation.

ZFT zero-force theorem.

BIBLIOGRAPHY

[1] P. Hohenberg and W. Kohn. Inhomogeneous electron gas. *Phys. Rev.*, 136:B864–B871, Nov 1964.

[2] W. Kohn and L. J. Sham. Self-consistent equations including exchange and correlation effects. *Phys. Rev.*, 140:A1133–A1138, Nov 1965.

[3] J. P. Perdew and Alex Zunger. Self-interaction correction to density-functional approximations for many-electron systems. *Phys. Rev. B*, 23:5048–5079, May 1981.

[4] John P. Perdew, Robert G. Parr, Mel Levy, and Jose L. Balduz. Density-functional theory for fractional particle number: Derivative discontinuities of the energy. *Phys. Rev. Lett.*, 49:1691–1694, Dec 1982.

[5] Mel Levy, John P. Perdew, and Viraht Sahni. Exact differential equation for the density and ionization energy of a many-particle system. *Phys. Rev. A*, 30:2745–2748, Nov 1984.

[6] C.-O. Almbladh and U. von Barth. Exact results for the charge and spin densities, exchange-correlation potentials, and density-functional eigenvalues. *Phys. Rev. B*, 31:3231–3244, Mar 1985.

[7] David J. Tozer and Nicholas C. Handy. Improving virtual Kohn–Sham orbitals and eigenvalues: Application to excitation energies and static polarizabilities. *The Journal of Chemical Physics*, 109(23):10180–10189, 1998.

[8] Andreas Dreuw, Jennifer L. Weisman, and Martin Head-Gordon. Long-range charge-transfer excited states in time-dependent density functional theory require non-local exchange. *The Journal of Chemical Physics*, 119(6):2943–2946, 2003.

[9] Martín A. Mosquera and Adam Wasserman. Derivative discontinuities in density functional theory. *Molecular Physics*, 112(23):2997–3013, 2014.

[10] Erich Runge and E. K. U. Gross. Density-functional theory for time-dependent systems. *Phys. Rev. Lett.*, 52:997–1000, Mar 1984.

[11] Robert van Leeuwen. Mapping from densities to potentials in time-dependent density-functional theory. *Phys. Rev. Lett.*, 82:3863–3866, May 1999.

[12] Neepa T Maitra. Charge transfer in time-dependent density functional theory. *Journal of Physics: Condensed Matter*, 29(42):423001, Sep 2017.

[13] P. Elliott, J. I. Fuks, A. Rubio, and N. T. Maitra. Universal Dynamical Steps in the Exact Time-Dependent Exchange-Correlation Potential. *Phys. Rev. Lett.*, 109:266404, Dec 2012.

[14] Johanna I. Fuks. Time-dependent density functional theory for charge-transfer dynamics: review of the causes of failure and success*. *The European Physical Journal B*, 89(11):236, Nov 2016.

[15] Johanna I. Fuks, Kai Luo, Ernesto D. Sandoval, and Neepa T. Maitra. Time-resolved spectroscopy in time-dependent density functional theory: An exact condition. *Phys. Rev. Lett.*, 114:183002, May 2015.

[16] Yasumitsu Suzuki, Lionel Lacombe, Kazuyuki Watanabe, and Neepa T. Maitra. Exact time-dependent exchange-correlation potential in electron scattering processes. *Phys. Rev. Lett.*, 119:263401, Dec 2017.

[17] M. J. P. Hodgson, J. D. Ramsden, J. B. J. Chapman, P. Lillystone, and R. W. Godby. Exact time-dependent density-functional potentials for strongly correlated tunneling electrons. *Phys. Rev. B*, 88:241102, Dec 2013.

[18] M. Born and R. Oppenheimer. Zur Quantentheorie der Molekeln. *Annalen der Physik*, 389(20):457–484, 1927.

[19] Mel Levy. Universal variational functionals of electron densities, first-order density matrices, and natural spin-orbitals and solution of the v-representability problem. *Proceedings of the National Academy of Sciences*, 76(12):6062–6065, 1979.

[20] D. M. Ceperley and B. J. Alder. Ground State of the Electron Gas by a Stochastic Method. *Phys. Rev. Lett.*, 45:566–569, Aug 1980.

[21] O. Gunnarsson and B. I. Lundqvist. Exchange and correlation in atoms, molecules, and solids by the spin-density-functional formalism. *Phys. Rev. B*, 13:4274–4298, May 1976.

[22] D. R. Hartree. The wave mechanics of an atom with a non-Coulomb central field. part ii. some results and discussion. *Mathematical Proceedings of the Cambridge Philosophical Society*, 24(1):111–132, 1928.

[23] J. C. Slater. Note on Hartree's method. *Phys. Rev.*, 35:210–211, Jan 1930.

[24] V. Fock. Näherungsmethode zur Lösung des quantenmechanischen Mehrkörperproblems. *Zeitschrift für Physik A Hadrons and Nuclei*, 61(1):126–148, January 1930.

[25] Douglas Rayner Hartree and W. Hartree. Self-consistent field, with exchange, for beryllium. *Proceedings of the Royal Society of London. Series A - Mathematical and Physical Sciences*, 150(869):9–33, 1935.

[26] G. Vignale. Center of mass and relative motion in time dependent density functional theory. *Phys. Rev. Lett.*, 74:3233–3236, Apr 1995.

[27] John F. Dobson. Harmonic-Potential Theorem: Implications for Approximate Many-Body Theories. *Phys. Rev. Lett.*, 73:2244–2247, Oct 1994.

[28] Neepa T. Maitra, Kieron Burke, and Chris Woodward. Memory in time-dependent density functional theory. *Phys. Rev. Lett.*, 89:023002, Jun 2002.

[29] M. Born and V. Fock. Beweis des Adiabatensatzes. *Zeitschrift für Physik*, 51(3-4):165–180, March 1928.

[30] M. Thiele, E. K. U. Gross, and S. Kümmel. Adiabatic approximation in nonperturbative time-dependent density-functional theory. *Phys. Rev. Lett.*, 100:153004, Apr 2008.

[31] Neepa T. Maitra. Perspective: Fundamental aspects of time-dependent density functional theory. *The Journal of Chemical Physics*, 144(22):220901, 2016.

[32] D. Pines. *Elementary excitations in solids: lectures on phonons, electrons, and plasmons*. Lecture notes and supplements in physics. W. A. Benjamin, 1964.

[33] M.P. Marder. *Condensed Matter Physics*. Wiley, 2010.

[34] M. Petersilka, U. J. Gossmann, and E. K. U. Gross. Excitation energies from time-dependent density-functional theory. *Phys. Rev. Lett.*, 76:1212–1215, Feb 1996.

[35] H. Ehrenreich and M. H. Cohen. Self-consistent Field Approach to the Many-Electron Problem. *Phys. Rev.*, 115:786–790, Aug 1959.

[36] John P. Perdew and Karla Schmidt. Jacob's ladder of density functional approximations for the exchange-correlation energy. *AIP Conference Proceedings*, 577(1):1–20, 2001.

[37] C. Ullrich. *Time-Dependent Density-Functional Theory: Concepts and Applications*, page 31. Oxford Graduate Texts. OUP Oxford, 2012.

[38] Randolph Q. Hood, M. Y. Chou, A. J. Williamson, G. Rajagopal, R. J. Needs, and W. M. C. Foulkes. Quantum Monte Carlo investigation of exchange and correlation in silicon. *Phys. Rev. Lett.*, 78:3350–3353, Apr 1997.

[39] Randolph Q. Hood, M. Y. Chou, A. J. Williamson, G. Rajagopal, and R. J. Needs. Exchange and correlation in silicon. *Phys. Rev. B*, 57:8972–8982, Apr 1998.

[40] R.G. Parr and W. Yang. *Density-Functional Theory of Atoms and Molecules*. International Series of Monographs on Chemistry. Oxford University Press, USA, 1994.

[41] R.M. Dreizler and E.K.U. Gross. *Density Functional Theory: An Approach to the Quantum Many-Body Problem*. Springer Berlin Heidelberg, 2012.

[42] R. O. Jones and O. Gunnarsson. Density-functional formalism: Sources of error in local-density approximations. *Phys. Rev. Lett.*, 55:107–110, Jul 1985.

[43] S. H. Vosko, L. Wilk, and M. Nusair. Accurate spin-dependent electron liquid correlation energies for local spin density calculations: a critical analysis. *Canadian Journal of Physics*, 58(8):1200–1211, 1980.

[44] Kieron Burke, John P. Perdew, and Y. Wang. Derivation of a generalized gradient approximation: The PW91 density functional. In J.F. Dobson, G. Vignale, and M.P. Das, editors, *Electronic Density Functional Theory: Recent Progress and New Directions*, pages 81–112. Springer US, NY, 2013.

[45] C. J. Umrigar and Xavier Gonze. Accurate exchange-correlation potentials and total-energy components for the helium isoelectronic series. *Phys. Rev. A*, 50:3827–3837, Nov 1994.

[46] John P. Perdew, J. A. Chevary, S. H. Vosko, Koblar A. Jackson, Mark R. Pederson, D. J. Singh, and Carlos Fiolhais. Atoms, molecules, solids, and surfaces: Applications of the generalized gradient approximation for exchange and correlation. *Phys. Rev. B*, 46:6671–6687, Sep 1992.

[47] Wei-Xue Li, Catherine Stampfl, and Matthias Scheffler. Oxygen adsorption on Ag(111): A density-functional theory investigation. *Phys. Rev. B*, 65:075407, Jan 2002.

[48] M. Petersilka, E. K. U. Gross, and Kieron Burke. Excitation energies from time-dependent density functional theory using exact and approximate potentials. *International Journal of Quantum Chemistry*, 80(4-5):534–554, 2000.

[49] Mark E. Casida, Christine Jamorski, Kim C. Casida, and Dennis R. Salahub. Molecular excitation energies to high-lying bound states from time-dependent density-functional response theory: Characterization and correction of the time-dependent local density approximation ionization threshold. *The Journal of Chemical Physics*, 108(11):4439–4449, 1998.

[50] Mark E. Casida and Dennis R. Salahub. Asymptotic correction approach to improving approximate exchange–correlation potentials: Time-dependent density-functional theory calculations of molecular excitation spectra. *The Journal of Chemical Physics*, 113(20):8918–8935, 2000.

[51] David J. Tozer and Nicholas C. Handy. On the determination of excitation energies using density functional theory. *Phys. Chem. Chem. Phys.*, 2:2117–2121, 2000.

[52] Adam Wasserman, Neepa T. Maitra, and Kieron Burke. Accurate Rydberg excitations from the local density approximation. *Phys. Rev. Lett.*, 91:263001, Dec 2003.

[53] Christine Jamorski, Mark E. Casida, and Dennis R. Salahub. Dynamic polarizabilities and excitation spectra from a molecular implementation of time-

dependent density-functional response theory: N2 as a case study. *The Journal of Chemical Physics*, 104(13):5134–5147, 1996.

[54] G.D. Mahan and K.R. Subbaswamy. *Local Density Theory of Polarizability*. Physics of Solids and Liquids. Springer US, 1990.

[55] R. van Leeuwen and E. J. Baerends. Exchange-correlation potential with correct asymptotic behavior. *Phys. Rev. A*, 49:2421–2431, Apr 1994.

[56] Andreas Görling. New KS method for molecules based on an exchange charge density generating the exact local KS exchange potential. *Phys. Rev. Lett.*, 83:5459–5462, Dec 1999.

[57] Fabio Della Sala and Andreas Görling. Excitation energies of molecules by time-dependent density functional theory based on effective exact exchange Kohn–Sham potentials. *International Journal of Quantum Chemistry*, 91(2):131–138, 2003.

[58] Kenneth B. Wiberg, R.Eric Stratmann, and Michael J. Frisch. A time-dependent density functional theory study of the electronically excited states of formaldehyde, acetaldehyde and acetone. *Chemical Physics Letters*, 297(1):60 – 64, 1998.

[59] David J. Tozer, Roger D. Amos, Nicholas C. Handy, Björn O. Roos, and Luis Serrano-Andrés. Does density functional theory contribute to the understanding of excited states of unsaturated organic compounds? *Molecular Physics*, 97(7):859–868, 1999.

[60] T Yanai, DP Tew, and NC Handy. A new hybrid exchange-correlation functional using the Coulomb-attenuating method (CAM-B3LYi). *Chemical Physics Letters*, 393(1-3):51–57, 7 2004.

[61] Yan Zhao and Donald G. Truhlar. Density functional for spectroscopy: No long-range self-interaction error, good performance for Rydberg and charge-transfer states, and better performance on average than B3LYP for ground states. *The Journal of Physical Chemistry A*, 110(49):13126–13130, 2006.

[62] Michael J. G. Peach, Aron J. Cohen, and David J. Tozer. Influence of Coulomb-attenuation on exchange–correlation functional quality. *Phys. Chem. Chem. Phys.*, 8:4543–4549, 2006.

[63] Michael J. G. Peach, Peter Benfield, Trygve Helgaker, and David J. Tozer. Excitation energies in density functional theory: An evaluation and a diagnostic test. *The Journal of Chemical Physics*, 128(4):044118, 2008.

[64] Sigalit Berkovic Ben-Shlomo and Uzi Kaldor. N2 excitations below 15 ev by the multireference coupled-cluster method. *The Journal of Chemical Physics*, 92(6):3680–3682, 1990.

[65] Egon S. Nielsen, Poul Jørgensen, and Jens Oddershede. Transition moments and dynamic polarizabilities in a second order polarization propagator approach. *The Journal of Chemical Physics*, 73(12):6238–6246, 1980.

[66] Neepa T. Maitra, Fan Zhang, Robert J. Cave, and Kieron Burke. Double excitations within time-dependent density functional theory linear response. *The Journal of Chemical Physics*, 120(13):5932–5937, 2004.

[67] Robert J. Cave, Fan Zhang, Neepa T. Maitra, and Kieron Burke. A dressed TDDFT treatment of the 21Ag states of butadiene and hexatriene. *Chemical Physics Letters*, 389(1):39 – 42, 2004.

[68] Mark E. Casida. Propagator corrections to adiabatic time-dependent density-functional theory linear response theory. *The Journal of Chemical Physics*, 122(5):054111, 2005.

[69] Oleg V. Gritsenko and Evert Jan Baerends. Double excitation effect in non-adiabatic time-dependent density functional theory with an analytic construction of the exchange–correlation kernel in the common energy denominator approximation. *Phys. Chem. Chem. Phys.*, 11:4640–4646, 2009.

[70] P. Romaniello, D. Sangalli, J. A. Berger, F. Sottile, L. G. Molinari, L. Reining, and G. Onida. Double excitations in finite systems. *The Journal of Chemical Physics*, 130(4):044108, 2009.

[71] Peter Elliott, Sharma Goldson, Chris Canahui, and Neepa T. Maitra. Perspectives on double-excitations in TDDFT. *Chemical Physics*, 391(1):110 – 119, 2011. Open problems and new solutions in time dependent density functional theory.

[72] David J. Tozer. Relationship between long-range charge-transfer excitation energy error and integer discontinuity in kohn–sham theory. *The Journal of Chemical Physics*, 119(24):12697–12699, 2003.

[73] A. Seidl, A. Görling, P. Vogl, J. A. Majewski, and M. Levy. Generalized Kohn-Sham schemes and the band-gap problem. *Phys. Rev. B*, 53:3764–3774, Feb 1996.

[74] Thierry Leininger, Hermann Stoll, Hans-Joachim Werner, and Andreas Savin. Combining long-range configuration interaction with short-range density functionals. *Chemical Physics Letters*, 275(3):151 – 160, 1997.

[75] Tamar Stein, Leeor Kronik, and Roi Baer. Reliable prediction of charge transfer excitations in molecular complexes using time-dependent density functional theory. *Journal of the American Chemical Society*, 131(8):2818–2820, Apr 2009.

[76] Roi Baer, Ester Livshits, and Ulrike Salzner. Tuned range-separated hybrids in density functional theory. *Annual Review of Physical Chemistry*, 61(1):85–109, 2010. PMID: 20055678.

[77] Elisa Rebolini, Andreas Savin, and Julien Toulouse. Electronic excitations from a linear-response range-separated hybrid scheme. *Molecular Physics*, 111(9-11):1219–1234, 2013.

[78] T Koopmans. Über die Zuordnung von Wellenfunktionen und Eigenwerten zu den Einzelnen Elektronen Eines Atoms. *Physica*, 1(1):104 – 113, 1934.

[79] Andreas Heßelmann, Andrey Ipatov, and Andreas Görling. Charge-transfer excitation energies with a time-dependent density-functional method suitable for orbital-dependent exchange-correlation kernels. *Phys. Rev. A*, 80:012507, Jul 2009.

[80] Maria Hellgren and E. K. U. Gross. Discontinuities of the exchange-correlation kernel and charge-transfer excitations in time-dependent density-functional theory. *Phys. Rev. A*, 85:022514, Feb 2012.

[81] Neepa T. Maitra. Undoing static correlation: Long-range charge transfer in time-dependent density-functional theory. *The Journal of Chemical Physics*, 122(23):234104, 2005.

[82] Neepa T. Maitra and David G. Tempel. Long-range excitations in time-dependent density functional theory. *The Journal of Chemical Physics*, 125(18):184111, 2006.

[83] Giovanni Onida, Lucia Reining, and Angel Rubio. Electronic excitations: density-functional versus many-body Green's-function approaches. *Rev. Mod. Phys.*, 74:601–659, Jun 2002.

[84] Silvana Botti, Francesco Sottile, Nathalie Vast, Valerio Olevano, Lucia Reining, Hans-Christian Weissker, Angel Rubio, Giovanni Onida, Rodolfo Del Sole, and R. W. Godby. Long-range contribution to the exchange-correlation kernel of time-dependent density functional theory. *Phys. Rev. B*, 69:155112, Apr 2004.

[85] I. V. Tokatly and O. Pankratov. Many-body diagrammatic expansion in a kohn-sham basis: Implications for time-dependent density functional theory of excited states. *Phys. Rev. Lett.*, 86:2078–2081, Mar 2001.

[86] Lucia Reining, Valerio Olevano, Angel Rubio, and Giovanni Onida. Excitonic effects in solids described by time-dependent density-functional theory. *Phys. Rev. Lett.*, 88:066404, Jan 2002.

[87] Gabriele Giuliani and Giovanni Vignale. *Quantum Theory of the Electron Liquid*. Cambridge University Press, 2005.

[88] Young-Moo Byun, Jiuyu Sun, and Carsten A Ullrich. Time-dependent density-functional theory for periodic solids: assessment of excitonic exchange-correlation kernels. *Electronic Structure*, 2020.

[89] Yong-Hoon Kim and Andreas Görling. Excitonic optical spectrum of semiconductors obtained by time-dependent density-functional theory with the exact-exchange kernel. *Phys. Rev. Lett.*, 89:096402, Aug 2002.

[90] Silvana Botti, Armel Fourreau, François Nguyen, Yves-Olivier Renault, Francesco Sottile, and Lucia Reining. Energy dependence of the exchange-correlation kernel of time-dependent density functional theory: A simple model for solids. *Phys. Rev. B*, 72:125203, Sep 2005.

[91] V. U. Nazarov and G. Vignale. Optics of semiconductors from meta-generalized-gradient-approximation-based time-dependent density-functional theory. *Phys. Rev. Lett.*, 107:216402, Nov 2011.

[92] Leonardo Bernasconi, Stanko Tomić, Mauro Ferrero, Michel Rérat, Roberto Orlando, Roberto Dovesi, and Nicholas M. Harrison. First-principles optical re-

sponse of semiconductors and oxide materials. *Phys. Rev. B*, 83:195325, May 2011.

[93] Zhixin Qian and Giovanni Vignale. Dynamical exchange-correlation potentials for an electron liquid. *Phys. Rev. B*, 65:235121, Jun 2002.

[94] Paolo E. Trevisanutto, Aleksandrs Terentjevs, Lucian A. Constantin, Valerio Olevano, and Fabio Della Sala. Optical spectra of solids obtained by time-dependent density functional theory with the jellium-with-gap-model exchange-correlation kernel. *Phys. Rev. B*, 87:205143, May 2013.

[95] Martin Panholzer, Matteo Gatti, and Lucia Reining. Nonlocal and nonadiabatic effects in the charge-density response of solids: A time-dependent density-functional approach. *Phys. Rev. Lett.*, 120:166402, Apr 2018.

[96] Thomas Olsen, Christopher Patrick, Jefferson Bates, Adrienn Ruzsinszky, and Kristian Thygesen. Beyond the RPA and GW methods with adiabatic xc-kernels for accurate ground state and quasiparticle energies. *npj Computational Materials*, 5, 12 2019.

[97] Gianni Adragna, Rodolfo Del Sole, and Andrea Marini. Ab initio calculation of the exchange-correlation kernel in extended systems. *Phys. Rev. B*, 68:165108, Oct 2003.

[98] Francesco Sottile, Valerio Olevano, and Lucia Reining. Parameter-free calculation of response functions in time-dependent density-functional theory. *Phys. Rev. Lett.*, 91:056402, Jul 2003.

[99] Andrea Marini, Rodolfo Del Sole, and Angel Rubio. Bound excitons in time-dependent density-functional theory: Optical and energy-loss spectra. *Phys. Rev. Lett.*, 91:256402, Dec 2003.

[100] Carsten Ullrich and Zeng-hui Yang. Excitons in time-dependent density-functional theory. *Topics in current chemistry*, 368, 03 2015.

[101] F. Perez and B. E. Granger. Ipython: A system for interactive scientific computing. *Computing in Science Engineering*, 9(3):21–29, 2007.

[102] S. Behnel, R. Bradshaw, C. Citro, L. Dalcin, D. S. Seljebotn, and K. Smith. Cython: The Best of Both Worlds. *Computing in Science Engineering*, 13(2):31–39, 2011.

[103] M. J. P. Hodgson. *Electrons in model nanostructures*. PhD thesis, University of York, 2016.

[104] Richard B. Lehoucq, Danny C. Sorensen, and Chao Yang. Arpack users' guide - solution of large-scale eigenvalue problems with implicitly restarted arnoldi methods. In *Software, environments, tools*, 1998.

[105] Pauli Virtanen, Ralf Gommers, Travis E. Oliphant, Matt Haberland, Tyler Reddy, David Cournapeau, Evgeni Burovski, Pearu Peterson, Warren Weckesser, Jonathan Bright, Stéfan J. van der Walt, Matthew Brett, Joshua Wilson, K. Jarrod Millman, Nikolay Mayorov, Andrew R. J. Nelson, Eric Jones, Robert Kern, Eric Larson, CJ Carey, İlhan Polat, Yu Feng, Eric W. Moore, Jake Vand erPlas, Denis Laxalde, Josef Perktold, Robert Cimrman, Ian Henriksen, E. A. Quintero, Charles R Harris, Anne M. Archibald, Antônio H. Ribeiro, Fabian Pedregosa, Paul van Mulbregt, and SciPy 1. 0 Contributors. SciPy 1.0: Fundamental Algorithms for Scientific Computing in Python. *Nature Methods*, 17:261–272, 2020.

[106] M. T. Entwistle and R. W. Godby. Exact exchange-correlation kernels for optical spectra of model systems. *Phys. Rev. B*, 99:161102, Apr 2019.

[107] J. J. Moré, B. S. Garbow, and K. E. Hillstrom. User guide for MINPACK-1. Report ANL-80-74, pub-ANL, pub-ANL:adr, 1980.

[108] Nick Woods. On the Nature of Self-Consistency in Density Functional Theory. *arXiv e-prints*, page arXiv:1803.01763, March 2018.

[109] M. C. Payne, M. P. Teter, D. C. Allan, T. A. Arias, and J. D. Joannopoulos. Iterative minimization techniques for ab initio total-energy calculations: molecular dynamics and conjugate gradients. *Rev. Mod. Phys.*, 64:1045–1097, Oct 1992.

[110] G. Kresse and J. Furthmüller. Efficiency of ab-initio total energy calculations for metals and semiconductors using a plane-wave basis set. *Computational Materials Science*, 6(1):15 – 50, 1996.

[111] R. O. Jones and O. Gunnarsson. The density functional formalism, its applications and prospects. *Rev. Mod. Phys.*, 61:689–746, Jul 1989.

[112] Warren E. Pickett. Pseudopotential methods in condensed matter applications. *Computer Physics Reports*, 9:115 – 197, Apr 1989.

[113] X. Gonze, Ph. Ghosez, and R. W. Godby. Density-functional theory of polar insulators. *Phys. Rev. Lett.*, 78:294–297, Jan 1997.

[114] Manfred Lein, E. K. U. Gross, and John P. Perdew. Electron correlation energies from scaled exchange-correlation kernels: Importance of spatial versus temporal nonlocality. *Phys. Rev. B*, 61:13431–13437, May 2000.

[115] OV Gritsenko, SJA Van Gisbergen, A Görling, EJ Baerends, et al. Excitation energies of dissociating H-2: A problematic case for the adiabatic approximation of time-dependent density functional theory. *J. Chem. Phys*, 113(19):8478–8489, 2000.

[116] Neepa T. Maitra, Kieron Burke, and Chris Woodward. Memory in time-dependent density functional theory. *Phys. Rev. Lett.*, 89:023002, Jun 2002.

[117] Kieron Burke, Jan Werschnik, and EKU Gross. Time-dependent density functional theory: Past, present, and future. *J. Chem. Phys*, 123(6):062206, 2005.

[118] Daniele Varsano, Andrea Marini, and Angel Rubio. Optical saturation driven by exciton confinement in molecular chains: A time-dependent density-functional theory approach. *Phys. Rev. Lett.*, 101:133002, Sep 2008.

[119] Martín A. Mosquera and Adam Wasserman. Integer discontinuity of density functional theory. *Phys. Rev. A*, 89:052506, May 2014.

[120] Paula Mori-Sanchez and Aron J. Cohen. The derivative discontinuity of the exchange-correlation functional. *Phys. Chem. Chem. Phys.*, 16:14378–14387, 2014.

[121] M. T. Entwistle, M. J. P. Hodgson, J. Wetherell, B. Longstaff, J. D. Ramsden, and R. W. Godby. Local density approximations from finite systems. *Phys. Rev. B*, 94:205134, Nov 2016.

[122] Michele Casula, Claudia Filippi, and Sandro Sorella. Diffusion Monte Carlo Method with Lattice Regularization. *Phys. Rev. Lett.*, 95:100201, Sep 2005.

[123] Michele Casula, Sandro Sorella, and Gaetano Senatore. Ground state properties of the one-dimensional Coulomb gas using the lattice regularized diffusion Monte Carlo method. *Phys. Rev. B*, 74:245427, Dec 2006.

[124] Luke Shulenburger, Michele Casula, Gaetano Senatore, and Richard M Martin. Spin resolved energy parametrization of a quasi-one-dimensional electron gas. *Journal of Physics A: Mathematical and Theoretical*, 42(21):214021, 2009.

[125] Min-Cheol Kim, Eunji Sim, and Kieron Burke. Understanding and reducing errors in density functional calculations. *Phys. Rev. Lett.*, 111:073003, Aug 2013.

[126] Gao Xianlong. $2k_F$-friedel to $4k_F$-wigner oscillations in one-dimensional fermi gases under confinement. *Phys. Rev. A*, 86:023616, Aug 2012.

[127] G. E. Astrakharchik and M. D. Girardeau. Exact ground-state properties of a one-dimensional coulomb gas. *Phys. Rev. B*, 83:153303, Apr 2011.

[128] John P. Perdew and Yue Wang. Accurate and simple analytic representation of the electron-gas correlation energy. *Phys. Rev. B*, 45:13244–13249, Jun 1992.

[129] John P. Perdew. Accurate density functional for the energy: Real-space cutoff of the gradient expansion for the exchange hole. *Phys. Rev. Lett.*, 55:1665–1668, Oct 1985.

[130] John P. Perdew, Kieron Burke, and Matthias Ernzerhof. Generalized gradient approximation made simple. *Phys. Rev. Lett.*, 77:3865–3868, Oct 1996.

[131] John P. Perdew, Matthias Ernzerhof, and Kieron Burke. Rationale for mixing exact exchange with density functional approximations. *The Journal of Chemical Physics*, 105(22):9982–9985, 1996.

[132] Emil Proynov, S. Sirois, and Dennis Salahub. Extension of the LAP functional to include parallel spin correlation. *International Journal of Quantum Chemistry*, 64:427 – 446, Jan 1997.

[133] Troy Van Voorhis and Gustavo E. Scuseria. A novel form for the exchange-correlation energy functional. *The Journal of Chemical Physics*, 109(2):400–410, 1998.

[134] John P. Perdew, Stefan Kurth, Aleš Zupan, and Peter Blaha. Accurate density functional with correct formal properties: A step beyond the generalized gradient approximation. *Phys. Rev. Lett.*, 82:2544–2547, Mar 1999.

[135] Jianwei Sun, Adrienn Ruzsinszky, and John P. Perdew. Strongly constrained and appropriately normed semilocal density functional. *Phys. Rev. Lett.*, 115:036402, Jul 2015.

[136] Giovanni Vignale. Sum rule for the linear density response of a driven electronic system. *Physics Letters A*, 209(3):206 – 210, 1995.

[137] G. Vignale and Walter Kohn. Current-dependent exchange-correlation potential for dynamical linear response theory. *Phys. Rev. Lett.*, 77:2037–2040, Sep 1996.

[138] Paul Hessler, Neepa T. Maitra, and Kieron Burke. Correlation in time-dependent density-functional theory. *The Journal of Chemical Physics*, 117(1):72–81, 2002.

[139] Johannes Neugebauer, Evert Jan Baerends, and Marcel Nooijen. Vibronic coupling and double excitations in linear response time-dependent density functional calculations: Dipole-allowed states of N2. *The Journal of Chemical Physics*, 121(13):6155–6166, 2004.

[140] C. A. Ullrich and I. V. Tokatly. Nonadiabatic electron dynamics in time-dependent density-functional theory. *Phys. Rev. B*, 73:235102, Jun 2006.

[141] K. J. H. Giesbertz, E. J. Baerends, and O. V. Gritsenko. Charge transfer, double and bond-breaking excitations with time-dependent density matrix functional theory. *Phys. Rev. Lett.*, 101:033004, Jul 2008.

[142] Johanna I. Fuks, Angel Rubio, and Neepa T. Maitra. Charge transfer in time-dependent density-functional theory via spin-symmetry breaking. *Phys. Rev. A*, 83:042501, Apr 2011.

[143] N. Singh, P. Elliott, T. Nautiyal, J. K. Dewhurst, and S. Sharma. Adiabatic generalized gradient approximation kernel in time-dependent density functional theory. *Phys. Rev. B*, 99:035151, Jan 2019.

[144] E. K. U. Gross and Walter Kohn. Local density-functional theory of frequency-dependent linear response. *Phys. Rev. Lett.*, 55:2850–2852, Dec 1985.

[145] G. Vignale, C. A. Ullrich, and S. Conti. Time-dependent density functional theory beyond the adiabatic local density approximation. *Phys. Rev. Lett.*, 79:4878–4881, Dec 1997.

[146] J.F. Dobson, G. Vignale, and M.P. Das. *Electronic Density Functional Theory: Recent Progress and New Directions*. Springer US, 2013.

[147] C. A. Ullrich and G. Vignale. Linewidths of collective excitations of the inhomogeneous electron gas: Application to two-dimensional quantum strips. *Phys. Rev. B*, 58:7141–7150, Sep 1998.

[148] C. A. Ullrich and G. Vignale. Theory of the linewidth of intersubband plasmons in quantum wells. *Phys. Rev. Lett.*, 87:037402, Jul 2001.

[149] P. L. de Boeij, F. Kootstra, J. A. Berger, R. van Leeuwen, and J. G. Snijders. Current density functional theory for optical spectra: A polarization functional. *The Journal of Chemical Physics*, 115(5):1995–1999, 2001.

[150] M. van Faassen, P. L. de Boeij, R. van Leeuwen, J. A. Berger, and J. G. Snijders. Ultranonlocality in time-dependent current-density-functional theory: Application to conjugated polymers. *Phys. Rev. Lett.*, 88:186401, Apr 2002.

[151] C. A. Ullrich and G. Vignale. Time-dependent current-density-functional theory for the linear response of weakly disordered systems. *Phys. Rev. B*, 65:245102, May 2002.

[152] M. van Faassen, P. L. de Boeij, R. van Leeuwen, J. A. Berger, and J. G. Snijders. Application of time-dependent current-density-functional theory to non-local exchange-correlation effects in polymers. *The Journal of Chemical Physics*, 118(3):1044–1053, 2003.

[153] Na Sai, Michael Zwolak, Giovanni Vignale, and Massimiliano Di Ventra. Dynamical corrections to the DFT-LDA electron conductance in nanoscale systems. *Phys. Rev. Lett.*, 94:186810, May 2005.

[154] Roberto D'Agosta and Giovanni Vignale. Relaxation in Time-Dependent Current-Density-Functional Theory. *Phys. Rev. Lett.*, 96:016405, Jan 2006.

[155] I. D'Amico and C. A. Ullrich. Dissipation through spin Coulomb drag in electronic spin transport and optical excitations. *Phys. Rev. B*, 74:121303, Sep 2006.

[156] J. Berger, Pina Romaniello, Robert van Leeuwen, and P.L. Boeij. Performance of the Vignale-Kohn functional in the linear response of metals. *Phys. Rev. B*, 74:245117, Dec 2006.

[157] V. U. Nazarov, J. M. Pitarke, Y. Takada, G. Vignale, and Y.-C. Chang. Including nonlocality in the exchange-correlation kernel from time-dependent current density functional theory: Application to the stopping power of electron liquids. *Phys. Rev. B*, 76:205103, Nov 2007.

[158] M. van Faassen and P. L. de Boeij. Excitation energies for a benchmark set of molecules obtained within time-dependent current-density functional theory using the Vignale-Kohn functional. *The Journal of Chemical Physics*, 120(18):8353–8363, 2004.

[159] C. A. Ullrich and Kieron Burke. Excitation energies from time-dependent density-functional theory beyond the adiabatic approximation. *The Journal of Chemical Physics*, 121(1):28–35, 2004.

[160] M. van Faassen and P. L. de Boeij. Excitation energies of π-conjugated oligomers within time-dependent current-density-functional theory. *The Journal of Chemical Physics*, 121(21):10707–10714, 2004.

[161] J. A. Berger, P. L. de Boeij, and R. van Leeuwen. Analysis of the viscoelastic coefficients in the Vignale-Kohn functional: The cases of one- and three-dimensional polyacetylene. *Phys. Rev. B*, 71:155104, Apr 2005.

[162] J. A. Berger, P. L. de Boeij, and R. van Leeuwen. Analysis of the Vignale-Kohn current functional in the calculation of the optical spectra of semiconductors. *Phys. Rev. B*, 75:035116, Jan 2007.

[163] I. V. Tokatly. Quantum many-body dynamics in a Lagrangian frame: I. equations of motion and conservation laws. *Phys. Rev. B*, 71:165104, Apr 2005.

[164] I. V. Tokatly. Quantum many-body dynamics in a Lagrangian frame: Ii. geometric formulation of time-dependent density functional theory. *Phys. Rev. B*, 71:165105, Apr 2005.

[165] I.V. Tokatly. Time-dependent deformation approximation. In M. A. L. Marques, C. A. Ullrich, F. Nogueira, A. Rubio, K. Burke, and E.K.U. Gross, editors, *Time-Dependent Density Functional Theory*, chapter 8, pages 123–136. Springer-Verlag, Berlin Heidelberg, 2006.

[166] C. Ullrich. *Time-Dependent Density-Functional Theory: Concepts and Applications*, pages 465–476. Oxford Graduate Texts. OUP Oxford, 2012.

[167] M. J. P. Hodgson, J. D. Ramsden, T. R. Durrant, and R. W. Godby. Role of electron localization in density functionals. *Phys. Rev. B*, 90:241107, Dec 2014.

[168] M. Thiele and S. Kümmel. Reconstructing the adiabatic exchange-correlation kernel of time-dependent density-functional theory. *Phys. Rev. A*, 80:012514, Jul 2009.

[169] F. Aryasetiawan and O. Gunnarsson. Exchange-correlation kernel in time-dependent density functional theory. *Phys. Rev. B*, 66:165119, Oct 2002.

[170] Diego J. Carrascal, Jaime Ferrer, Neepa Maitra, and Kieron Burke. Linear response time-dependent density functional theory of the Hubbard dimer. *The European Physical Journal B*, 91(7):142, Jul 2018.

[171] M. Thiele and S. Kümmel. Frequency dependence of the exact exchange-correlation kernel of time-dependent density-functional theory. *Phys. Rev. Lett.*, 112:083001, Feb 2014.

[172] Robert van Leeuwen. Key concepts in time-dependent density-functional theory. *International Journal of Modern Physics B*, 15(14):1969–2023, 2001.

[173] A. Ben-Israel and T.N.E. Greville. *Generalized Inverses: Theory and Applications*. CMS Books in Mathematics. Springer New York, 2006.

[174] M. T. Entwistle, M. Casula, and R. W. Godby. Comparison of local density functionals based on electron gas and finite systems. *Phys. Rev. B*, 97:235143, Jun 2018.

[175] C. Ullrich. *Time-Dependent Density-Functional Theory: Concepts and Applications*, pages 46–47. Oxford Graduate Texts. OUP Oxford, 2012.

[176] C. Ullrich. *Time-Dependent Density-Functional Theory: Concepts and Applications*, pages 124–127. Oxford Graduate Texts. OUP Oxford, 2012.

[177] F. Mohammed, R. Warmbier, and A. Quandt. Numerical techniques. In A. Agrawal, T. Benson, R.M. De La Rue, and G.A. Wurtz, editors, *Recent Trends in Computational Photonics*, Springer Series in Optical Sciences, chapter 12, pages 341–368. Springer International Publishing, Cham, Switzerland, 2017.

[178] Stephen L. Adler. Quantum theory of the dielectric constant in real solids. *Phys. Rev.*, 126:413–420, Apr 1962.

[179] Nathan Wiser. Dielectric constant with local field effects included. *Phys. Rev.*, 129:62–69, Jan 1963.

[180] C. Ullrich. *Time-Dependent Density-Functional Theory: Concepts and Applications*, pages 98–103. Oxford Graduate Texts. OUP Oxford, 2012.